Economical e-Methanol Production: Dynamic Modelling and Optimal Scheduling of Power-to-Methanol Plant

Matej Vinko Primorac, Marin Veršić

TEPE4-1010, 2025-06

4th Semester Master Thesis

STUDENT REPORT

AALBORG UNIVERSITY

Title:
Economical e-Methanol Production: Dynamic Modelling and Optimal Scheduling of Power-to-Methanol Plant

Theme:
Design and Optimisation of Thermal Systems for Sustainable Fuel Production

Project Period:
2025

Project Group:
TEPE4-1010

Participants:
Matej Vinko Primorac
Marin Veršić

Supervisors:
Xiaoti Cui

Number of Pages: 103

Date of Completion:
May 28th - 2025

Abstract:

Power-to-methanol (PtMeOH) systems offer promising solutions for converting surplus renewable electricity into valuable energy carriers for hard-to-abate sectors. This work presents an integrated 50 MW PtMeOH production system with an annual demand of 25,000 tonnes of e-MeOH, addressing critical challenges such as high production costs and limited operational flexibility. Comprehensive steady-state and dynamic models were developed for all major components. A PEM electrolyser model was created in Simulink, capturing non-linear efficiency-load relationships varying from 76% at low loads to 67%. The methanol synthesis and distillation system was modelled using Aspen Tech, maintaining product specifications above 99.7% MeOH purity. System flexibility evaluation demonstrated that flexible operation (40–100% capacity) reduces e-MeOH production costs by 50 €/tonne compared to fixed-load operation. The system achieved 86% annual runtime with strategic partial load operation, minimising harmful start-stop cycles. Cost-effective optimisation determined optimal hourly schedules based on real electricity price data, achieving e-MeOH production cost of 1196.4 €/tonne. Economic analysis confirmed electrolyser costs dominate both CAPEX (90%) and OPEX (83%).

Summary

The increasing penetration of renewable energy sources creates challenges due to electricity supply fluctuations and dynamic pricing. Power-to-X (PtX) technologies, particularly power-to-methanol (PtMeOH) systems, offer promising solutions by converting surplus renewable electricity into valuable energy carriers for hard-to-abate sectors such as maritime transport and heavy industry.

This master thesis presents a techno-economic analysis of an integrated 50 MW PtMeOH production system with a demand of 25,000 tonnes of e-MeOH annually. The research successfully addresses critical challenges identified in e-MeOH production such as: high production costs compared to fossil alternatives, limited operational flexibility of existing systems, and insufficient understanding of dynamic coupling between major subsystems.

Modelling and system development was done through detailed steady-state and dynamic models for all major components. A PEM electrolyser (PEMEL) model was developed in Simulink incorporating six modules (membrane, anode, cathode, voltage, efficiency, and thermal), capturing the non-linear efficiency-load relationship that varies from 76% at low loads to 67%. The methanol synthesis and distillation (MSD) system was modelled using Aspen Plus and Aspen Plus Dynamics, demonstrating stable dynamic performance while maintaining product specifications above 99.7% MeOH purity.

System flexibility evaluation revealed operational advantages of variable load capability over fixed operation. The dynamic coupling between PEMEL and MSD systems was successfully obtained, demonstrating that flexible operation (40–100% capacity) reduces e-MeOH production costs by 50 €/tonne compared to fixed-load operation. The system achieved 86% annual runtime with strategic use of partial loads during moderate electricity price periods, effectively minimising harmful start-stop cycles while maintaining economic efficiency.

Cost-effective optimisation was implemented through a mixed-integer linear programming (MILP) framework in MATLAB, determining optimal hourly operational schedules based on real electricity price data. Results demonstrate that e-MeOH can be produced at 1196.4 €/tonne under optimal flexible operation, positioning it within the competitive range of current renewable MeOH technologies. Economic analysis confirmed that electrolyser costs dominate both CAPEX (90%) and OPEX (83%), identifying this component as the primary target for cost reduction. Sensitivity analysis revealed critical dependencies on CO_2 pricing and electrolyser efficiency improvements as key factors for future competitiveness.

The developed modelling framework and optimisation methodology offer practical tools for commercial PtMeOH development, contributing to the broader implementation of Power-to-X technologies in sustainable energy systems.

Preface

The following master thesis has been written by 4th semester M.Sc. students Matej Vinko Primorac and Marin Veršić, at the Department of Energy of Aalborg University, as the final project for the Master of Science in Energy Engineering program. The project has been supervised by Associate Professor Xiaoti Cui.

This thesis is carried out in collaboration with another student from the Department of Materials and Production at Aalborg University, Filip Džigurski. While his work centres on forecasting electricity cost models, this thesis focuses on system modelling, evaluation of operational flexibility, and optimisation of dynamic, cost-effective e-methanol production. The two projects are developed separately but are integrated in a joint case study towards the end.

The authors would like to express their gratitude to Associate Professor Xiaoti Cui for his guidance, valuable feedback, and support throughout the project.

Reading Guide

The citations have been done using the APA method, where citations will be shown as Author(s) (year). The citations follow their references in the bibliography located at the end of the thesis. Chapters, sections, figures, tables and equations are labeled and these will also be referenced when mentioned in the text. The numbering of these labels is in chronological order and chapter-wise. Throughout the report, some symbols and abbreviations may have different subscripts, however, these differences can be found in the Nomenclature.

<div style="text-align:center">

Matej Vinko Primorac
mprimo23@student.aau.dk

Marin Versic
mversi23@student.aau.dk

</div>

Signature: _____   Signature: _____

Nomenclature

Chemical Symbol	Description
CH_3OH	Methanol
CH_4	Methane
CO	Carbon monoxide
CO_2	Carbon dioxide
e^-	Electrons
H^+	Hydrogen ions
H_2	Hydrogen
H_2O	Water
IrO_2	Iridium dioxide
$MeOH$	Methanol
N_2	Nitrogen
NH_3	Ammonia
O_2	Oxygen
O^{2-}	Oxygen ions
OH^-	Hydroxide ions
$\cdot OH$	Hydroxyl radical
Pt	Platinum

Symbol	Description	SI Unit
A	Total area of MEA (Membrane Electrode Assembly)	$[cm^2]$
A_{ex}	Heat transfer Area of HEX	$[m^2]$
a	Gas dependent coefficient	$[-]$
b	Gas dependent coefficient	$[-]$
C	Concentration or cost constant	$[mol/m^3]$ or $[€]$
C_B	Base cost	$[€]$
C_c	Capital cost of equipment	$[€]$
C_{chill}	Chilled water price	$[€/GJ]$
C_{H+}	Concentration of hydrogen ions	$[mol/m^3]$
C_{stack}	Lumped heat capacity of PEM stack	$[J/K]$
C_{steam}	Low-pressure steam price	$[€/GJ]$
C_{tot}	Total lumped heat	$[J/K]$
$C_{water in system}$	Heat capacity of water in the PEMEL system	$[J/K]$
C^{CO_2}	CO_2 credit price	$[€/tonne]$
C^{cold}	Cold start cost	$[€]$
C^{heat}	Excess heat value	$[€/MW]$
C^{hot}	Hot start cost	$[€]$
c	Cost per hour	$[€/h]$
D	Diameter or duration parameter	$[m]$ or $[h]$
D_{A-B}	Binary diffusion coefficient	$[m^2/s]$
D_{H+}	Diffusitivity of hydrogen ions	$[m^2/s]$
D_w	Membrane water diffusion coefficient	$[m^2/s]$
D^{cold}	Cold start duration	$[h]$
D^{hot}	Hot start duration	$[h]$
$D^{MSD-cooling}$	MSD cooling duration	$[h]$
$D^{MSD-heating}$	MSD heating duration	$[h]$
$D^{MSD-ramp}$	MSD ramp duration	$[h]$
D^{SB}	Stand-by duration	$[h]$
D^{tank}	Tank filling duration	$[h]$
d_M	Crystallite diameter	$[m]$

Symbol	Description	SI Unit
e	Error of PI controller	[various]
E	Energy consumption	[MWh]
E_a	Activation energy	[J/mol]
E^{con}	Electrolyser power consumption including losses	[MW]
$E^{\text{con-SB}}$	Standby power consumption including losses	[MW]
E^{MSD}	MSD system power consumption	[MW]
$E^{\text{MSD-ramp}}$	MSD ramp-up/down power consumption	[MW]
$E^{\text{MSD-SB}}$	MSD standby power consumption	[MW]
F	Faraday constant	[C/mol]
f_M	Effect of material of construction for capital cost	[–]
f_P	Effect of operating pressure for capital cost	[–]
f_T	Effect of operating temperature for capital cost	[–]
H	Height	[m]
I	Current	[A]
i	Current density	[A/cm^2]
i_0	Exchange current density	[A/cm^2]
i_x	Current density of crossover	[A/cm^2]
K	Permeability	[m^2]
$K_{a,b,c}$	Adsorption constants	[various]
K_{darcy}	Membrane permeability to water (Darcy)	[cm^2]
K_{eq}	Equilibrium constant	[various]
K_i	Integral contribution	[–]
K_p	Gain	[–]
K_u	Ultimate gain	[–]
$k_{1,2}$	Rate constants	[various]
k_k	Permeability of species through membrane	[cm^2]
l	Load level index	[–]
l'	"FROM" Load level index	[–]
M	Cost exponent	[–]
M_m	Molar mass	[kg/mol]
M^{MEOH}	Methanol production	[kg]
M^{start}	MeOH production rate during start	[kg/min]
$M^{\text{MeOH}}_{\text{TARGET}}$	Target methanol production	[kg]
$M^{\text{MeOH}}_{\text{TOTAL}}$	Total methanol production	[kg]
m_M	Catalyst loading	[g/cm^2]
$\dot{m}$	Mass flow	[kg/s]
$\dot{n}$	Molar flow	[kmol/hr]
N	Number of cells	[–]
N_{module}	Number of modules	[–]
N_{stack}	Number of stacks	[–]
n_d	Electro-osmotic drag coefficient	[–]
P	Total pressure or Power	[Pa] or [W]
P_C	Critical pressure	[Pa]
P_u	Ultimate period	[–]
P^{el}_t	Electricity price at time t	[€/MWh]
p	Partial pressure	[Pa]
Q	Heat	[W]
Q_B	Base capacity	[–]
R	Gas constant	[J/(mol · K)]
R^2	Coefficient of determination	[–]
R_{th}	Thermal insulation factor	[J/(K/W)]
r	Reaction rate	[various]
r_c	Heat capacity ratio	[–]
s	Operating state index	[–]
T	Temperature or total time periods	[K] or [–]
T_C	Critical temperature	[K]
t	Time index	[–]

Symbol	Description	SI Unit
$t^{\text{min-run}}$	Minimum running time	[h]
$t^{\text{min-SB}}$	Minimum standby time	[h]
$t^{\text{min-SD}}$	Minimum shutdown time	[h]
t_{op}	Operation time	[h]
U	Heat-transfer coefficient	$[\text{kW}/(\text{K} \cdot \text{m}^2)]$
U	Overall heat transfer coefficient	$[\text{W}/(\text{m}^2\text{K})]$
V	Voltage	[V]
W	Electrical work/power	[W]
w	Binary decision variable for transition	[–]
x	Binary decision variable for running operation	[–]
Y_i	Real target output values	[–]
$\hat{Y}_i$	Predicted target output values	[–]
y	Binary decision variable for standby/shutdown	[–]
Z	Objective function value or compressibility factor	[€] or [–]
Z_{TOTAL}	Total cost function value	[€]
z	Binary decision variable for startup	[–]
$\dot{N}$	Molar flow rate	[mol/s]
$\dot{n}$	Molar flux	$[\text{mol}/(\text{s} \cdot \text{m}^2)]$

Greek Symbol	Description	SI Unit
α_{exp}	Experimental factor	[–]
α_t	Transfer coefficient	[–]
γ_M	Membrane roughness factor	[–]
$\delta_{el,an}$	Thickness of anode electrode	[m]
$\delta_{el,cat}$	Thickness of cathode electrode	[m]
δ_{mem}	Thickness of MEA	[m]
ΔG	Gibbs free energy change	[J/mol]
ΔH	Enthalpy change	[J/mol]
ϵ	Effectiveness factor	[–]
ε	Efficiency	[–]
ε_f	Porosity correction factor	[–]
ε_p	Percolation threshold factor	[–]
η_{motor}	Electric motor efficiency	[–]
η_{pump}	Pump efficiency	[–]
λ	Load level fraction	[–]
μ_{H2O}	Water viscosity	[Pa $\cdot$ s]
ρ_M	Catalyst density	[g/cm^3]
ρ_{molar}	Molar density	[mol/m^3]
σ	Conductivity	[S/m]
φ_I	Catalyst surface-ionomer fraction	[–]
Φ	Heat	[kJ]

Notation	Description
$\forall$	For all (universal quantifier)
$\in$	Element of (set membership)
$\leq$	Less than or equal to
ln	Natural logarithm
$\mathcal{L}$	Set of electrolyser load levels
$\mathcal{S}$	Set of operating states
$\mathcal{T}$	Set of time periods
min	Minimise (optimisation)
$\sum$	Summation
€	Euro (currency)
H/C ratio	Hydrogen/carbon ratio
L/D ratio	Length-to-diameter ratio
min	Minutes (time unit)
MW	Megawatt (power unit)
MWh	Megawatt-hour (energy unit)
0D	Zero-dimension
1D	One-dimension

Abbreviations

Abbreviation	Description
AC	Alternating current
AEL	Alkaline electrolyser
AI	Artificial intelligence
atm	Atmosphere (pressure unit)
ATV	Auto-tune
Bio-MeOH	Biogas-based methanol
CAPEX	Capital expenditures
CCUS	Carbon capture, utilisation and storage
CZA	$Cu-ZnO-Al_2O_3$
DAC	Direct air capture
DC	Direct current
DKK	Danish Krone (currency)
DSTWU	Underwood-Wine-Gilliland
EES	Engineering Equation Solver
E-MeOH	Electricity-based methanol
EPRI	Electric Power Research Institute
EU	European Union
F-MeOH	Fossil-based methanol
GHG	Green-house-gas
GHSV	Gas hourly space velocity
HEX	Heat exchanger
intlinprog	Integer linear programming solver (MATLAB)
JT	Joule-Thomson
KPI	Key performance indicators
LHV	Lower heating value
LNG	Liquified natural gas
LSTM	Long Short-Term Memory
MAE	Mean absolute error
MATLAB	Matrix Laboratory (software)
MD	Methanol distillation
MEA	Membrane electrode assembly
MILP	Mixed-integer linear programming
MS	Methanol synthesis
MSD	Methanol synthesis and distillation
NREL	National Renewable Energy Laboratory
NRTL	Non-random two-liquid
NTU	Number of transfer units
OPEX	Operating expenditures
PEM	Proton exchange membrane
PEMEL	PEM electrolyser
PtMeOH	Power-to-Methanol
PtX	Power-to-X
RadFrac	Rigorous Algorithm Distillation Fractionation
RWGS	Reversed water-gas-shift
SAF	Sustainable aviation fuels
SB	Standby
SD	Shutdown
SOEL	Solid-oxide electrolyser
TAC	Total annual cost
TRL	Technology Readiness Level

Subscripts & Superscripts

Subscript	Description
x_0	Reference
$x_{\Delta H}$	First law
x_{act}	Activation
x_{amb}	Ambient
x_{an}	Anode
x_{cat}	Cathode
x_{cell}	Cell
x_{ch}	Channel
x_{cond}	Condenser
x_{conc}	Concentration
$x_{cooling}$	Cooling
$x_{CR\text{-}METH}$	Crude Methanol
x_{eff}	Effective
x_{gen}	Generated
x_{H2}	Hydrogen
x_{H2O}	Water
x_{heater}	Heater
x_l	Load level index
x_{loss}	Loss
x_{max}	Maximum
x_{min}	Minimum
x_{O2}	Oxygen
x_{OC}	Open circuit
x_{ohm}	Ohmic
x_{pump}	Pump
x_{PUR}	Purge
x_{ratred}	Rated
x_{reac}	Reaction
x_{ref}	Reference
$x_{refrigerant}$	Refrigerant
x_{ren}	Reboiler
x_{rev}	Reversible
x_{sat}	Saturated
x_{std}	Standard
x_t	Time index
x_{TARGET}	Target value
x_{TCOMP}	Compressor
x_{tn}	Thermoneutral
x_{TOTAL}	Total value

Superscript	Description
x^0	Standard conditions
x^{cold}	Cold start
x^{conc}	Concentration (gradient)
x^{cons}	Consumed
x^{el}	Electrical/electricity
x^{elec}	Electrolyser
x^{eod}	Electro-osmotic drag
x^{gen}	Generated
x^{heat}	Heat-related
x^{hot}	Hot start
x^{in}	Inlet
x^{inj}	Injected
x^{mem}	Membrane
x^{MeOH}	Methanol
x^{MSD}	Methanol synthesis and distillation

Superscript (cont.)	Description
x^{out}	Outlet
x^{pg}	Pressure gradient
x^{SB}	Standby
$x^{\text{SB-trans}}$	Standby transition
x^{SD}	Shutdown
$x^{\text{SD-trans}}$	Shutdown transition
x^{start}	Start-up
x^{trans}	Transition

Contents

List of Figures

List of Tables

Chapter 1

Introduction

The transition to clean energy has accelerated in recent years, thanks to global efforts to satisfy rising energy demands and respond to climate changes. The cost of renewable energy technologies, particularly solar photovoltaics and wind turbines, has dramatically decreased in recent years. Specifically, the price of solar electricity has fallen by approximately 80% and wind energy by around 40% over the past decade [1]. This cost reduction plays a big role in decarbonising power supply chain. However, despite these advances, certain sectors remain challenging to decarbonise directly through electrification alone, including maritime shipping, aviation, heavy transportation, and various industrial processes [2]. These industries require energy-dense fuels and feedstocks that electricity alone cannot easily provide.

In this context, power-to-X (PtX) technologies have emerged to convert renewable electricity into energy carriers that can substitute for fossil fuels in these applications. Energy carriers like ammonia (NH_3) and methanol (MeOH) offer a way to store and transport renewable energy in chemical form. The general PtX concept encompasses converting surplus renewable electricity into fuels such as hydrogen (H_2), NH3, or MeOH that can be stored for long periods and shipped to where energy is needed. MeOH, in particular, has attracted attention as a versatile carrier: it can be produced through three main routes, conventionally from syngas (yielding fossil-based MeOH, or f-MeOH), with biomass (yielding bio-MeOH) or from green hydrogen and captured carbon dioxide (CO_2) (yielding e-MeOH), which aligns with PtX strategies. [1]

Notably, e-MeOH is liquid at ambient conditions and has a higher volumetric energy density than H_2 gas, enabling use of existing fuel infrastructure with minimal modifications. Its synthesis from renewable resources such as biogenic CO_2 and electrolytic H_2 contributes to CO_2 utilisation and supports a more sustainable carbon cycle. MeOH also holds potential as a clean fuel or as a feedstock for chemicals like formaldehyde and acetic acid, as well as in applications such as fuel cells and residential heating. Given these advantages, e-MeOH is a particularly promising PtX fuel pathway[1, 3, 4]

Integrating renewable energy into the electricity supply chain presents significant challenges, primarily due to the non-flexibility of power generation. To optimally address grid integration challenges, PtX plants, such as those producing e-MeOH, must operate dynamically. Unlike conventional plants, PtX facilities need flexible operational strategies that allow them to ramp production up or down based on real-time electricity supply conditions, thus actively compensating for renewable energy fluctuations [4].

Developing these dynamic, responsive PtX systems is complex, and current operational data is limited due to their novelty and high complexity. Because of this, there is still a significant knowledge gap regarding how to optimally design and manage these dynamic processes for economic efficiency [5, 6].

This project specifically targets this gap, focusing on developing fast, flexible, and economical operational solutions for e-MeOH production. The ultimate goal is to establish methods to produce low-cost e-MeOH efficiently, thereby bridging the critical gap between green electricity production and green fuel availability. The outcomes of this research aim

to significantly contribute to the broader adoption and integration of PtX solutions into future sustainable energy systems.

1.1 Report Structure

After briefly introducing the problem that will be the topic of interest in this report, the state-of-the-art section follows, presenting the up-to-date stage of development of PtX and e-MeOH production technology with an overview of available research and industrial cases. Following this, the system configuration and theoretical background are defined to establish the motivation and technical basis for the study. The methodology chapter then outlines the modelling approaches and tools used, including both steady-state and dynamic simulation environments. Subsequently, the case study is presented, where operational strategies are evaluated. Finally, the results of the study are then discussed in detail, leading to key insights and conclusions regarding system flexibility and economic performance under fluctuating electricity trends.

To maintain the integrity and clarity of each section, certain content may be intentionally repeated throughout the report, to ensure that all sections are fully comprehensive and can stand independently.

1.2 Literature Review

This chapter presents a literature review of the most relevant topics related to the project and contributes to an understanding of the current state-of-the-art in Power-to-MeOH (PtMeOH) technology development. It begins by summarising key findings from recent outlook reports, providing insights into the primary drivers behind the development of PtMeOH systems and their supporting technologies. The chapter then reviews scientific studies that examine real-life implementations of PtMeOH plants. Finally, relevant researches on different system units are also introduced.

1.2.1 Industry Outlooks and Predictions

DNV's *Hydrogen Forecast To 2050* [2] is a forecast reporting about the H_2 role in the energy transition in the following years. It says that H_2 derivates like NH_3, MeOH and e-kerosene will play a key role in decarbonising the heavy transport sector, because in that case, electricity, or pure H_2 cannot be used directly. Reason why H_2 cannot be used directly is because of its expensive storage and low volumetric energy density. Even though e-MeOH is not completely green solution, it is considered to be a low-carbon chemical, and can be produced with previously captured CO_2 from flue gases, direct air capture, etc. Forecast predicts that prices of CO_2 will rise in the following years, which can negatively affects the e-MeOH price on the market. On the other hand, it is assumed that taxes on fossil fuel will increase in line with the region's carbon-price regime, and supports on h_2 infrastructure and renewable energy plants will increase.

There are little to no open commodity markets for H_2, with the exception of markets for H_2 derivatives such as MeOH. The biggest potential for application of e-MeOH fuel is

found in maritime industry, where there are already ships being made that can use MeOH as a fuel ([7, 8]), even though e-MeOH is not widely spread yet.

International Renewable Energy Agency (IRENA) released the *Renewable Methanol Outlook* [1] in which the key finding is that MeOH produced from green H_2 and Co_2 has too high production cost and low production volume, but with funded researches and right policies, it can become cost-competitive before 2050. The current cost of e-MeOH is estimated to be in the range of 745-1490 €/tonne, and is estimated to drop to levels between 232-585 €/tonne. The outlook [1] gives a comprehensive research on the MeOH properties, historical prices, usage possibilities, and other alternative production options (e.g. from municipal solid waste). An overview of ongoing projects for e-MeOH facilities and demonstration plants is given, of which several are presented further down in the text. Later, capital expenditures (CAPEX) and operating expenditures (OPEX) overview, and comparative study with current and forecasting prices are presented.

S.S.Araya et al. (2022) [6] gave a comprehensive overview of the PtX technologies, different types of electrolysers, CO_2 and water (H_2O) sources for PtX, and MeOH as a fuel.

1.2.2 Case Studies of PtMeOH Plants

The base case for research in this report is Y.Zheng et al.(2022) [4] in which grid-connected PtMeOH system is introduced. The modelled plant consists of alkaline electrolyser (AEL), a MeOH synthesis (MS), and a MeOH distillation (MD) part. It is assumed that MeOH converters can go from zero to maximum load in few minutes, while AEL designed with three defined operating states (production, standby, and off state). Development of AEL model and its dynamic behaviour is detailed in Y. Zheng et al. (2022) [9] with a reported H_2 production capacity of 405 kg/h. MS plan incorporate two main chemical reactions in the model: hydrogenation of CO2 and reverse water-gas-shift (R-WGS) reaction. The model used for optimisation is made in one dimension (1D), and is validated with Aspen Plus model. The catalytic reactor operates at 483.15 K and 76 bars, with H/C ratio of 3:1, and recycle ratio of 4.115.

The optimisation model aims to minimise the operational cost while satisfying a fixed daily MeOH demand. The cost components considered include electricity costs, hot and cold start-up costs of the AEL, and CO_2 emissions. Reported cost of f-MeOH is in the range of 300-500 €/tonne, while the calculated cost of e-MeOH ranges from 584 to 1146 €/tonne, depending on CO_2 and electricity prices. Electricity, primarily consumed by the AEL, is identified as the dominant component of the OPEX.

Taslimi et al. (2024) [10] present a comprehensive techno-economic analysis of a large-scale commercial PtX plant in Kassø, Denmark. This facility focuses on MeOH production, with H_2 supplied by a 52.5 MW electrolyser plant developed by Siemens Energy. The project is owned, constructed, and operated by European Energy. The PtX system consists of three PEM electrolyser (PEMEL) units, each with a capacity of 17.5 MW. It also includes an air-cooling system for the electrolysers, a compressor line, a CO_2 storage system, a heat pump and two MS units. The maximum annual production capacity of the facility is 44,000 tonnes of MeOH. As part of their research, Taslimi et al. developed a dynamic electrol-

yser model, an MS plant model, and an optimisation model for plant load management. Their analysis explores optimal operating conditions, potential sector coupling between the power and heat sectors, and the economic feasibility of integrating such systems. The study evaluates how changes in electricity prices, CO_2 costs, and MeOH market prices impact system performance.

The results indicate that the electrolyser's operation and MeOH pricing are highly dependent on electricity spot prices. When considering the current market price of MeOH (470 €/tonne), the plant operates at an annual load of 20%. However, when a premium price is introduced to meet production requirements, the annual load increases to 66%. To ensure a minimum annual production of 32,000 tonnes of MeOH, a calculated total price of 1092 €/tonne is necessary. This adjustment corresponds to a premium price of 660 €/tonne. The plant released its first product on the March 2025 [11]. [10]

M. Fuglsang (2022) [12] presents a socioeconomic feasibility study of the "FjordPtX" project, which aims to build a PtX facility in the Aalborg municipality in Denmark. The plant is designed to produce 130,000 tons of MeOH annually. For the purposes of the research, a simulation model of the facility was developed using Microsoft Excel. Several system scenarios involving a PEMEL were evaluated, with focus on the difference between configurations with and without H_2 storage. In scenarios where H_2 storage is integrated, the electrolyser operates dynamically. The control strategy is as follows: when electricity prices fall below 30 €/MWh, the electrolyser operates at full capacity, supplying both the H_2 storage and the MeOH plant. When prices exceed 50 €/MWh, the electrolyser is shut down. For prices in between, it runs at half capacity, supplying only the MeOH plant. By following this operational strategy, the cost of producing e-MeOH is reduced from 1084 to 1108 €/tonne. Bunker oil is used as the reference fuel for cost comparison, with levelised costs adjusted based on energy density. The planned facility will include a 300 MW electrolysis plant, and among all components, the PtMeOH facility represents the most significant investment. Its annual OPEX are estimated at approximately 83 million euros, with around 50% attributed to electrolysis. Additionally, the plant's excess heat is intended for use in district heating systems, and it is assumed that benefits of selling produced oxygen (O_2) are no substantial for the ultimate cost, and therefore not included. The same goes for the expenses for H_2O, land, and transport.

The results of the study indicate that PtMeOH offers several socio-economic benefits, including improved electricity grid stability, job creation, and CO_2 emission reductions. The analysis also highlights the strong influence of electricity prices on the levelised cost of MeOH. Furthermore, the report underlines the importance of considering the technological immaturity of PtMeOH systems at this scale. The facility is scheduled to begin operation in 2028. [12]

S.Sollai et al. (2023) [13] presents a pre-feasibility study of a PtMeOH plant designed for production of 500 kg/h of e-MeOH (corresponding to about 4000 tonne/year) from green H_2 and captured CO_2. Firstly, they highlight that 90 Mt of MeOH is produced yearly, 65% from LNG (steam reforming), and 35% from coal (gasification), when e-MeOH is less than 0.2%. A process model is made in Aspen Plus software for optimising the process and for further economic analysis, including CO_2 capture and H_2 production units. As a case study, the plant is assumed to be on Sardinia island, Italy, with a purpose of giving a solution on how to assure the stability of the electric grid in the region. The electrolyser

used is PEMEL, instead of AEL, since it has advantages of "faster cold start-up, a higher flexibility and, consequently, a better coupling with dynamic and intermittent power generation systems", and "are able to operate at lower cell voltages, higher current densities, and higher temperatures and pressures leading to higher efficiencies". Estimated lifetime of PEMEL is 60,000 h. Power consumption of PEMEL is 50-80 kWh/kgH_2, with capacity around 6MW. H_2 storage system operates at 200 bars, and has a capacity to secure the operation of e-MeOH plant "for several hours". Operating pressure of their MS reactor is 65 bars, and temperatures are 483-563 K (inlet-outlet), second separator works at 1.2 bars and 295 K, and distillation column operates at 1.1 bar and 353 K. The composition of distillate is 96.4% MeOH and 3.6% CO_2. For the economic assessment, the annual inflation rate of 1.33% is assumed.

As a result, S.Sollai et al. (2023) [13] got that 20-year lifetime of a plant is assumed when calculating a levelised cost of e-MeOH of 960 €/tonne (about 175 €/MWh). The results shows that technology is still not competitive from the economic point of view, since current MeOH price is 450 €/tonne. Thanks to the future developments, and European policies, it is assumed that process is expected to become competitive in a mid-term future. The study also reveals that MeOH production cost is mainly affected by the electricity price and the electrolyser capital cost, as well as the capacity factor of the plant.

A more comprehensive overview of PtMeOH technology is provided by L. Marques et al. (2024) [14]. This study presents detailed examples of industrial-scale facilities, demonstration units, and ongoing projects funded by the EU (European Union) and those around the world. It also includes a techno-economic analysis of e-MeOH production processes, emphasising their potential to support carbon neutrality in hard-to-abate sectors, particularly the cement industry. The report compiles publicly available information on these plants, which will serve as references throughout this report.

1.2.3   Relevant Findings on System Components

R. Hancke (2022) [15] highlights that H_2 compression is a crucial part of the green H_2 supply chain. However, mechanical compressors are prone to failure and increase system complexity and cost. High-pressure H_2O electrolysis offers a potential solution by enabling internal electrochemical compression within the electrolyser, thus eliminating the need for external H_2 compressors. PEMEL operating at pressures compatible with end-use applications offer several benefits. They can remove the need for mechanical compressors, components that are bulky, costly, noisy, and require frequent maintenance. For this research, a semi-empirical model of the PEMEL, along with supporting units, was developed using the Engineering Equation Solver (EES) software. In Hancke's economic model, the stack replacement cost is assumed to be 35% of the initial PEMEL system cost.

The paper states that, in theory, electrochemical compression losses in a PEMEL can be estimated using the Nernst equation. For instance, increasing the pressure from 30 to 200 bar at 333 K adds about 55 mV to the cell voltage. Although mass transport polarisation slightly decreases with pressure, its impact on cell voltage at 2 A/cm^2 is minor—dropping from 12.3 mV at 30 bar to 10.5 mV at 200 bar. The results indicate that high-pressure PEMEL systems, operating up to 200 bar, can be economically viable. These pressure levels align well with the requirements of current and future industrial applications, such as

e-fuel production (30–120 bar).

D. Marlin et al. (2018) [16] argue that synthesising MeOH directly from CO_2 and H_2 offers several advantages over traditional methods based on syngas (a mixture of CO, CO_2, and H_2). Although the CO_2 to MeOH pathway is less reactive, requiring larger reactors, and results in higher H_2O and CO_2 content in the crude product, it brings notable benefits: greater selectivity, fewer byproducts, milder reaction conditions, and improved carbon utilisation. Using pure feed streams enables precise stoichiometric control without the need for costly reforming steps. Moreover, due to the reduced impurity levels, MeOH can be effectively purified using a single distillation column, eliminating the need for complex setups like multi-column systems or advanced techniques such as pressure swing distillation.

In the context of MS via CO_2 hydrogenation, the choice of reactor plays a crucial role in determining both the overall efficiency and economic feasibility of the process. According to Cui et al. (2020) [17], a comparative analysis of three reactor types—adiabatic, water-cooled, and gas-cooled—revealed that the adiabatic fixed-bed reactor offers the lowest capital cost among them. Adiabatic reactors are providing acceptable temperature profiles within the safe operating window for conventional Cu-based catalysts and allowing for straightforward scalability. Complementing this reactor design, the $Cu-ZnO-Al_2O_3$ (CZA) catalyst remains one of the most industrially viable and widely adopted systems for MeOH production via CO_2 hydrogenation. As noted by Mohammed et al. (2024) [18], CZA exhibits high catalytic activity, long operational lifetime, and strong resistance to deactivation by poisoning, making it a reliable choice for sustained industrial use.

B.Lee et al. (2020) [19] highlights how renewable MS using green H_2 and the CO_2 captured from various industrial processes as well as the atmosphere has received significant attention. In this context, the technical and economic feasibility analysis of renewable MS was conducted in this study. A model of a MeOH plant, using CO_2 hydrogenation, was developed using Aspen HYSYS. Several options to make e-MeOH economically feasible are proposed, assessing the effects of key performance indicators (KPI). Various parameters were varied in a specific range, like gas hourly space velocity (GHSV) (1000-10000 h^{-1}), temperature (483-543 K), pressure (50-100 bar), H/C ratio (1-12). Under the optimum conditions, an economic analysis was performed to estimate the unit MeOH production costs at different capacities.

The study by Mbatha et al. (2024) [20] presents a comprehensive dynamic evaluation of MS reactors: adiabatic, gas-cooled, and water-cooled, under flexible operating conditions including shutdown and standby transitions. The report identifies two key principles for standby operation: the use of H_2 or nitrogen N_2 to maintain system standby, each affecting the restart time differently. For the adiabatic reactor operating under N_2 standby, a fast ramp-down at 1000% per hour reduces CO_2 and H_2 feed to zero within 6 minutes, while it takes approximately 1.5 hours for the system to reach standby temperature. During ramp-up, the system again reaches full feed flow in 6 minutes, but requires 39 minutes to achieve the operating temperature. In this thesis, the focus was not placed on modelling MeOH reactor standby behaviour, so all relevant operational values for standby operation of MS were adopted from this report.

Chapter 2

Problem Analysis

This chapter provides the necessary background to understand the challenges and opportunities explored in this report. It begins with an overview of the current state of the energy sector and its climate goals. From there, it introduces the Power-to-X (PtX) concept, with a focus on its potential to integrate renewable energy into hard-to-abate sectors. The theoretical principles behind electrolysis are then discussed, as electrolysers play a central role in hydrogen (H_2) production. Key H_2 properties, along with methods for its storage, are examined, followed by an outline of carbon capture, utilisation and storage (CCUS) technologies. Finally, the chapter addresses the role of methanol (MeOH) as a versatile energy carrier and chemical feedstock, highlighting its properties and various production pathways. Together, these topics provide the context and technical foundation needed to understand the challenges addressed in this report.

2.1 Climate Goals

The first chapter gave the insight of the climate goals, and possible options on how they can be reached. Now, this information will be covered more comprehensive, in order to get a clearer understanding of the topic.

2.1.1 Energy Transition

As it was mentioned earlier, the transition to clean energy has accelerated in recent years, thanks to multiple global efforts. Many efforts regarding the production of renewable electricity have been made, and it can be seen on the figure 2.1 that there has been an increase in renewable electricity generation in last 15 years.
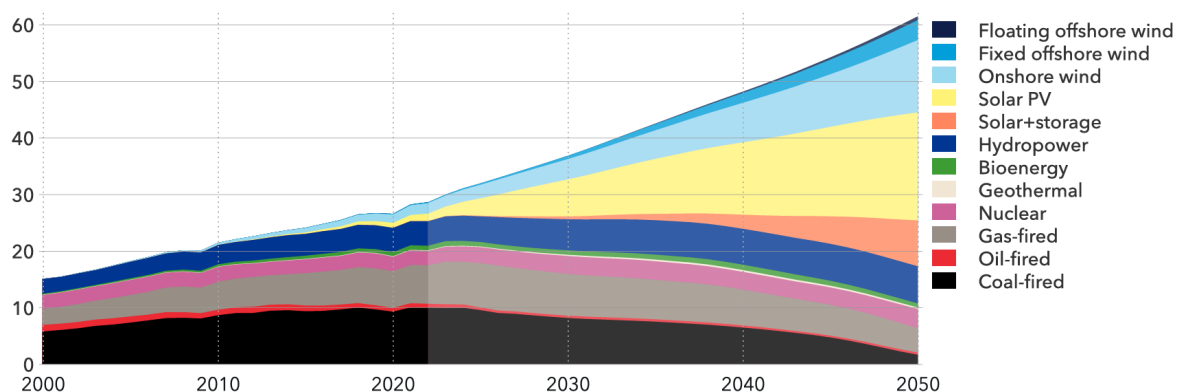
Figure 2.1: World grid-connected electricity generation by power station type [21]

Nevertheless, electricity demand is forecasted to doubled until 2050, from 30 to 61.6 petawatt-hours (PWh). The doubling of electricity demand is the result of several transformative changes across sectors. One of the primary drivers is the electrification of transport,

but also the electrification of the industrial sectors, such as heating, and increase in electricity consumption in households. In general, studies show that as economic activities in a certain region rise, so does the electricity consumption. Further, the prediction is that H_2 production demand will rise exponentially, and will require 1.9 PWh by 2050. The figure 2.1 illustrates how renewable electricity generation is expected to increase and meet the growing demand for energy in the future. [21]

2.1.2 Energy Storage Overview

Even though electricity consumption is increasing, there are periods in which there is a surplus electrical energy produced, since renewable electricity plants are not as flexible as conventional gas-, or coal-fired plants. To compensate for this drawback of the renewable sources, the development of energy storage solutions parallel to the transition in energy production is necessary. The figure 2.2 shows different storage solutions sorted by their potential capacity and discharge time. It is obvious that H_2 and its derivates has the biggest potential for large scale energy storage. [22]
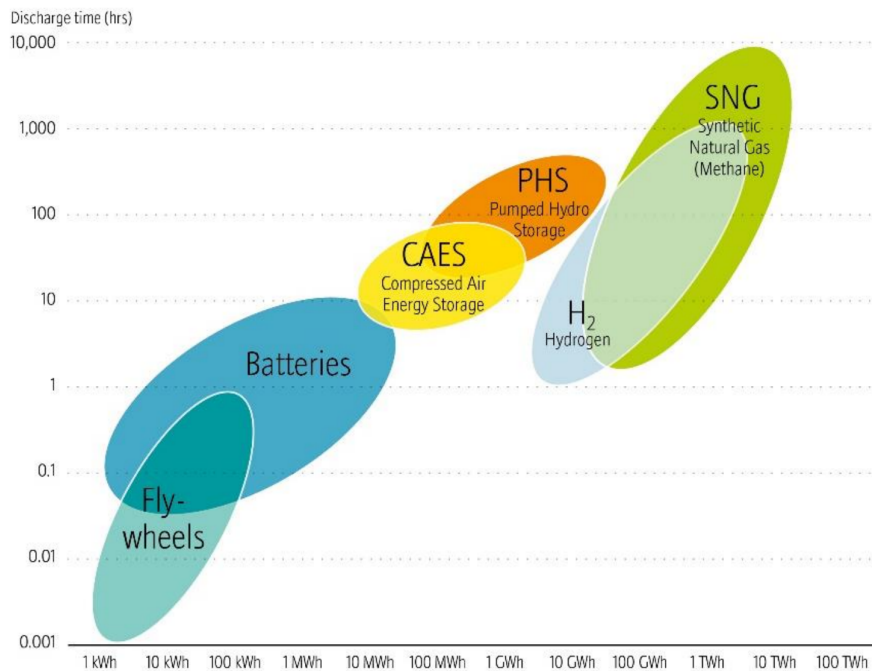
Figure 2.2: Overview storage capacity of different energy storage systems [23]

2.1.3 Dynamic Electricity Market

Increasing the share of renewable energy sources (particularly wind and solar) in electricity production leads to greater fluctuations in electricity prices. This is primarily due to their dependence on weather conditions and limited flexibility, which prevents them from adjusting output in response to real-time demand. As a result, electricity prices can vary significantly on an hourly basis (2.3.
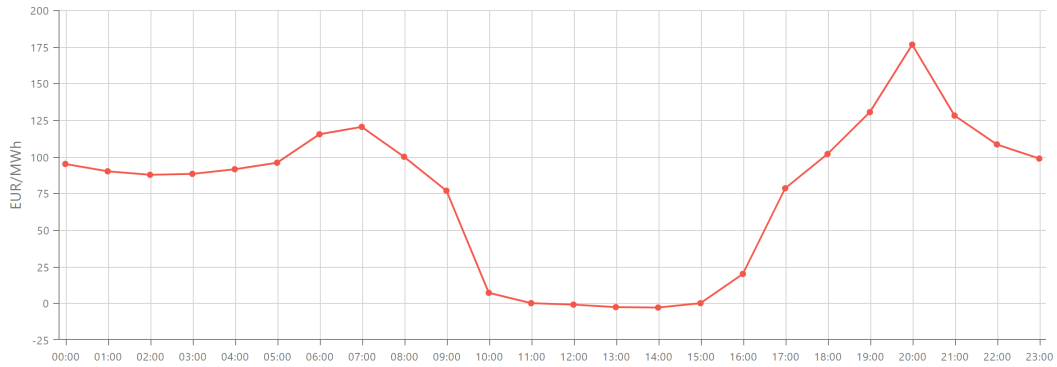
Figure 2.3: Example of a daily electricity price fluctuation in West-Denmark region [24]

While the variability of renewables poses challenges, literature suggests that increasing the share of diverse renewable sources can positively influence overall electricity costs. Additionally, renewables help address security concerns associated with traditional fossil fuels like natural gas and oil, which are subject to geopolitical and market instability. These benefits encourage governments and energy companies to actively pursue and expand renewable energy deployment. However, the rapid growth of renewables also introduces new complexities. One such issue is the surplus of electricity during periods of peak renewable generation, such as midday during sunny conditions, which can lead to negative electricity prices. Negative electricity prices occur when supply significantly exceeds demand, forcing power producers to pay consumers to take excess electricity. This situation can undermine the financial sustainability of power plants, particularly those with inflexible operations, as they incur costs to offload surplus electricity. It may also discourage investment in new generation capacity, creating long-term challenges for market stability and energy security. [22, 24–26]

PtX technologies offer promising solutions to several challenges mentioned so far. By converting surplus electricity into other forms of energy, PtX technologies can absorb excess supply, thereby helping to stabilise the electricity market and mitigate the occurrence of negative electricity prices. This improves market efficiency and strengthens the economic viability of renewable energy. In addition, PtX enables the indirect electrification of hard-to-abate sectors, further supporting deep decarbonisation across the energy system. This technologies are explained in more detail in the following section.

2.2 Power-to-X

2.2.1 General Concept

The goals to decarbonise all sectors, reduce green-house-gas (GHG) emissions and stabilise energy supply marker, together with changes in global policies, pushed the development of different solutions to face these problems. As already mentioned earlier, one such solution is coupling renewable electricity to other sectors through H_2 production, where both renewable H_2 and low-emission H_2 are expected to have a major role in the clean energy transition, especially in hard-to-abate industries. Hard-to-abate industries are the ones which are challenging to decarbonise directly, because they cannot be connected to the electrical grid, and require high independency and energy-dense fuels, which batteries alone cannot meet. This category includes long-distance maritime shipping, aviation,
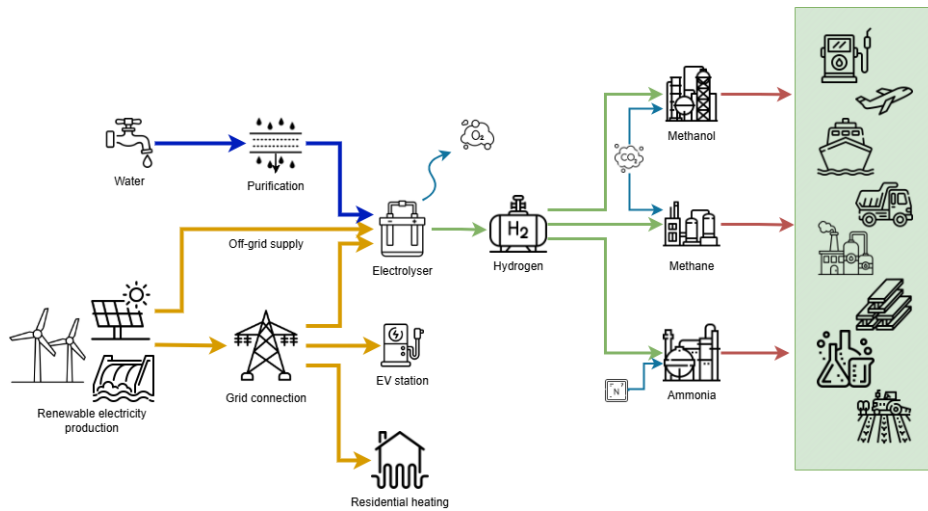
Figure 2.4: Illustration of Power-to-X concept

heavy-duty transportation, and heavy-industry processes like production of cement and steel. This indirect electrification of different sectors is known as sector coupling, also known as PtX. Figure 2.4 illustrates the concept of PtX. The power in PtX processes could theoretically be generated from any source. However, if it is not of renewable origin, the entire purpose of transitioning away from fossil fuels is defeated. The method of obtaining power for PtX processes is beyond the scope of this project and will therefore not be further discussed.

This power can be used in a district heating network or directly in transportation, where it is referred to as Power-to-Heat and Power-to-Mobility, respectively. However, the main focus here is on using electricity to produce H_2 via electrolysis. Electrolysis can be powered either by a grid-connected source, where it helps balance the electricity grid, or by an off-grid power supply, where its power demand has no impact on the grid. In the second case, PtX plants are typically built close to renewable power sources to minimise complexity and cost. Examples of this approach are the Kassø plant in southern Denmark, connected directly to the Kassø solar park, and the energy islands planned to be built in the North Sea by 2030.

Since water is the raw material for electrolysis, electrolysers require a constant h_2O supply, which is typically desalinated or otherwise treated before use. H_2 produced in this way is central to the green transition through PtX, as it can be further converted into ammonia (NH_3), MeoH, or methanol (MeOH), or be used directly. One of the main contributions of PtX to climate targets is the substitution of petroleum in both fuel applications and the chemical industry. Additionally, PtX enables the conversion of captured carbon dioxide (CO_2), from either ambient air or industrial flue gases, into valuable products. These include energy carriers (fuels), sustainable aviation fuels (SAF), fertilisers, olefins, dimethyl ether, and various other chemicals.

S. Araya et al. (2022) mention that the market for PtX products is expected to grow significantly in the coming years, with global MeOH and H_2 markets projected to increase steadily through 2030. As PtX capacity expands, efficient integration with existing energy systems becomes increasingly important. A large share of the energy used in electrolysis is released as waste heat, which can be recovered to improve overall system efficiency. A leading example is the PtX plant in Esbjerg, Denmark, where excess heat from H_2 produc-

tion will supply district heating to up to 15,000 households. Additionally, treated wastewater will be reused within the plant. Such integrated approaches enhance sustainability, reduce energy waste, and add economic value to PtX facilities [6, 27, 28].

2.2.2 Electrolysers

The "to" part of Power-to-X refers to the conversion of electrical energy into another form, most commonly achieved through H_2O electrolysis. Electrolysers, which use electricity to split H_2O into H_2 and oxygen (O_2), are central to PtX systems and act as a bridge between sectors. In H_2O electrolysis a voltage is applied to the cells and a DC current passes between two electrodes, anode and cathode, in contact with an ionic conducting medium. H_2O fuelled to the electrolyser is decomposed and split into H_2 and (O_2) in an endothermal chemical reaction. Even though h_2O electrolysis is an endothermal reaction, electrolyser actually releases heat during its operation, due to inefficiencies in the system. The overall reaction of this process is given below:

$$H_2O \rightarrow H_2 + \tfrac{1}{2}O_2 \qquad\qquad \Delta H = 285.8 \text{ kJ/mol} \qquad (2.1)$$

The commonly used electrolysis technologies are alkaline electrolyser (AEL), solid oxide electrolyser (SOEL) and proton exchange membrane electrolyser (PEMEL) 2.5.
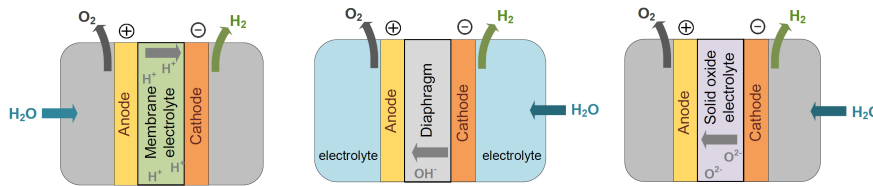
Figure 2.5: Conceptual schemes of different types of electrolysers [6]

AEL has the oldest and most established technology. They use a liquid alkaline solution (typically potassium hydroxide or sodium hydroxide) as the electrolyte, and operate at moderate temperatures of 343-363 K. In this system, H_2 gas hydroxide ions (OH^-) are produced. Ions move from the cathode to the anode through electrolyte and a separator (diaphragm) towards the anode. There, they are oxidised to form O_2 and water molecules. These systems are relatively simple, cost-effective, and suitable for large-scale applications. However, they are limited by slower dynamics and slower response to fluctuating loads, making them less ideal for integration with dynamic renewable energy systems.

PEM electrolysers use a solid polymer membrane, typically made from materials like Nafion® as the electrolyte. This membrane is designed to conduct hydrogen ions (H^+) while acting as a barrier to electrons and gases, ensuring high purity and safe separation of H_2 and O_2. Water is fed to the anode side, where it is split into O_2, protons (hydrogen ions), and electrons. The protons pass through the membrane to the cathode, while the electrons travel through an external circuit. At the cathode, protons and electrons recombine to form H_2 gas. This configuration enables a compact system with high efficiency, excellent gas separation, and fast response to changes in power input. The system is compact mainly because of polymer membrane is very thin, comparable to a kitchen plastic foil. PEM electrolysers operate at lower temperatures, typically between 323 and 353 K, and support high current densities and dynamic operation. Their main drawbacks are the high cost of materials, particularly the need for precious metal catalysts such as platinum

and iridium, and chemically robust membrane materials.

SOEL operate at much higher temperatures (873-1173 K) and use a solid ceramic electrolyte that conducts oxygen ions (O^{2-}). In this configuration, H_2O is introduced as steam, and the high temperature allows a portion of the required energy to be provided as heat, improving overall efficiency. Oxygen ions travel from the cathode to the anode, where O_2 is released. SOELs are promising for industrial applications, but they are still in the development phase due to materials challenges and durability issues at high temperatures. Their dynamics are usually slower than PEMEL and AEL, but are the highest in efficiency. In terms of technology readiness, AWE and PEM electrolysers are both considered commercially mature, typically classified as Technology Readiness Level (TRL) 8–9. In contrast, SOELs remain at TRL 6–7, reflecting their advanced efficiency potential but limited long-term demonstration. [6, 28, 29]

2.3 Hydrogen

This section provides an overview of H_2 physical and chemical properties, its environmental impact, and the role it plays in PtX systems, with a focus on its limitations and advantages in energy applications.

H_2 is the lightest molecule in nature, consisting of two hydrogen atoms, with a molecular weight of 2.016 g/mol. It is colorless, odorless, and non-toxic, and due to its small molecular size, H_2 has high diffusivity and permeability. Its molecules are non-polar, and its boiling point is 20.28 K at 1 atm.

2.3.1 Compressibility, Boil-off and Tank Filling

In its gaseous state, H_2 behaves similarly to an ideal gas within a limited temperature range and at low pressure. Outside this range, its behaviour deviates, which is quantified using the compressibility factor Z, a dimensionless value added to the ideal gas law (for an ideal gas, $Z = 1$). However, at high pressures, H_2's Z can differ significantly from 1, indicating non-ideal behaviour. As pressure increases, these deviations mean H_2 becomes harder to compress, requiring greater energy input.

H_2 low boiling point and small molecular size contribute to leakage and permeation through seals and container walls, making it challenging to store and handle. Even slight heat increase can cause evaporation and pressure build-up. A great example is NASA's Space Shuttle Program, where 45.4% of procured liquid H_2 was lost due to boil-off, despite sophisticated infrastructure. Although modern technology has improved storage conditions, boil-off losses can still reach up to 12% per day. These limitations reveal a major weakness of H_2 as an energy carrier. In PtX systems, this issue can be reduced by converting H_2 into more stable compounds, thereby minimising losses and improving overall system efficiency.

Another important physical characteristic of H_2 is the Joule-Thomson (JT) effect, which describes how a gas's temperature changes during adiabatic expansion at constant enthalpy. For most gases, expansion results in cooling, but H_2 behaves differently. Above its inversion temperature of approximately 200 K (at 1 atm), H_2 has a negative JT coefficient, meaning it warms up when pressure is reduced. This effect is observed during tank filling, where a temperature rise can occur. As this a H_2 safety issue and may cause multiple problems, additional cooling is typically required.

2.3.2 Energy Density

H_2 has a very low volumetric energy density in its gaseous state of approximately 0.01 MJ/L at 1 atm, despite having one of the highest gravimetric energy densities among all fuels (120–142 MJ/kg). When compressed to 700 bar, its volumetric energy density increases to about 5.6 MJ/L, and in liquid form, it reaches around 8.5 MJ/L. However, this remains low compared to conventional fuels: petrol provides about 32 MJ/L, diesel 35.8 MJ/L, MeOH 15.6 MJ/L, and NH_3 11.5 MJ/L. These differences make H_2 much less space-efficient for storage and transport, especially in mobile or long-range applications. This highlights the advantage of converting H_2 into denser synthetic fuels through PtX technologies to improve the overall energy storage efficiency of the final product.

2.3.3 Impact on the Environment

H_2 is non-toxic and produces no harmful byproducts when used, making it a clean energy carrier at the point of use. However, when released into the atmosphere, it can indirectly contribute to global warming and is considered an "indirect greenhouse gas." It reacts with hydroxyl radicals ($\cdot$OH), particles which are essential for breaking down potent GHGs like (e.g. CH_4) Therefore, lack of hydroxyl radicals in the air prolongs their atmospheric lifetime.

The environmental impact of H_2 depends largely on its production method and is associated CO_2 footprint. H_2 is commonly categorised into 4 types based on its origin. Grey H_2 is produced from natural gas via steam methane reforming, releasing significant amount of CO_2. Blue H_2 follows the same process but incorporates CCUS to reduce emissions. Black H_2 is derived from coal through pyrolysis, with emissions similar to coal combustion. In contrast, green H_2 is generated via electrolysis powered by renewable energy and results in no direct CO_2 emissions. While grey, blue, and black H_2 rely on fossil fuels, green H_2 is considered the most sustainable and the only truly green option suitable for PtX applications and long-term climate goals. Figure 2.6 illustrates the projected transition from fossil-based H_2 to low-emission alternatives until 2050.
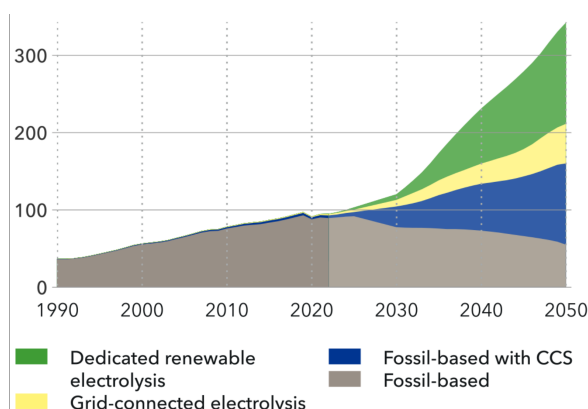
Figure 2.6: Projected global H_2 production by production type from 1990 to 2050 (Unit: Mt/year) [2]

2.3.4 Compression Challenges

H_2 is a clean and flexible energy carrier with a key role in grid stability and long-term storage through PtX systems. However, its use should be focused where it offers the

most value. In short-distance transport, such as city buses, battery electric solutions are already more efficient, as H_2 systems suffer from significant energy losses during production, compression, storage, and delivery. H_2 compression alone is technically complex and energy-intensive, often requiring multistage compressors and cooling to reach pressures up to 900 bar (350-700 bar for vehicles). In this project, H_2 is produced at high pressure and directly converted to MeOH, avoiding the need for extensive compression and storage. A small buffer tank is included only to manage dynamic mismatches between the electrolyser and MeOH synthesis (MS). As such, H_2 importance lies in decarbonising hard-to-electrify sectors like steel production and long-distance transport, where it enables indirect electrification that batteries alone cannot provide. [6, 29–32]

2.4 Carbon Capture, Utilisation and Storage

This section presents the role of CCUS in addressing the challenge of rising atmospheric CO_2 levels. It outlines the current trends in global CO_2 emissions, explains how CCUS works, identifies key CO_2 sources suitable for capture, and explores the suitability and costs of different CO_2 feedstocks for e-MeOH production.

2.4.1 Current State of CO_2 Emissions

One of the most urgent challenges in reaching global climate goals is the continuous increase in atmospheric CO_2 levels. Over the past few decades, CO_2 concentrations have steadily risen, as shown in Figure 2.7, which illustrates long-term measurements from the Mauna Loa Observatory in Hawaii. This site has been selected due to its remote location and high altitude, which allows it to provide reliable, baseline data on global atmospheric CO_2 concentrations, largely unaffected by local pollution sources.
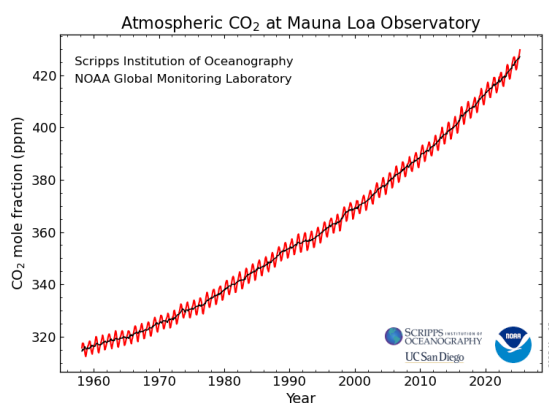
Figure 2.7: Mean CO_2 measured in atmosphere at Mauna Loa Observatory, Hawaii. [33]

Excess atmospheric CO_2 enhances the greenhouse effect, contributing to global warming and associated impacts such as extreme weather events, rising sea levels, and ecological disturbances. To limit global temperature rise to well below 2 °C above pre-industrial levels, as set by the Paris Agreement [34], a combination of emission reduction and carbon removal strategies is necessary. CCUS is among the most promising tools available to help achieve this goal.

2.4.2 CCUS and Its Importance in Emission Reduction Pathways

CCUS refers to the process of capturing CO_2 emissions from industrial sources or directly from the atmosphere, and either storing it in geological formations or utilising it as a feedstock for valuable products. Geological storage involves injecting compressed CO_2 into underground rock formations such as depleted oil and gas fields or deep saline aquifers, preventing it from entering the atmosphere. Alternatively, captured CO_2 can be used in the production of building materials, chemicals, and synthetic fuels, including e-MeOH, which is the focus of this thesis.

2.4.3 CO_2 Feedstock for the Production of E-MeOH

From the Figure 2.8, the sources of CO_2 used for e-MeOH production can be grouped into two categories: industrial sources and atmospheric sources.
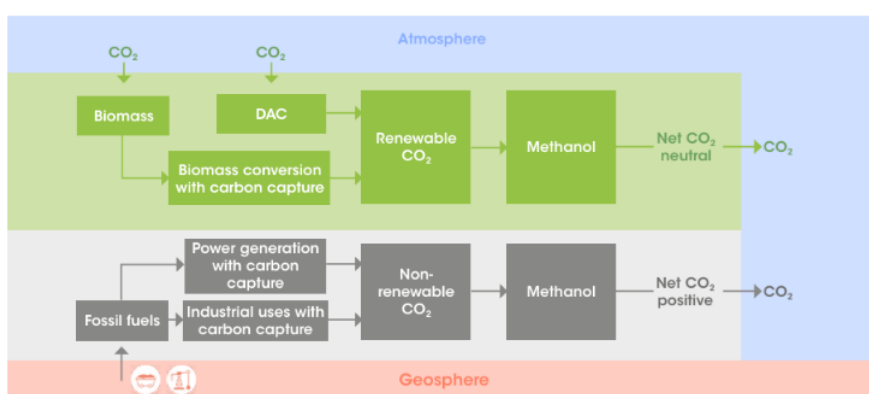
Figure 2.8: Overview of CO_2 feedstock sources for MeOH production [1]

Industrial CO_2 comes from fossil fuel-based processes such as power generation, cement production, and steel manufacturing. In these cases, CO_2 is a by-product of burning fossil fuels. Although capturing and reusing this CO_2 can reduce emissions, it is considered non-renewable because the carbon originates from fossil sources. The overall process is therefore carbon positive. Atmospheric CO_2 includes carbon captured directly from the air through Direct Air Capture (DAC) or from biogenic sources such as biomass. Since the carbon in biomass or air was originally taken from the atmosphere via natural processes, using it for e-MeOH production is considered renewable and can be nearly carbon negative.

2.4.4 CO_2 Cost Considerations

The cost of captured CO_2 depends on its source and the technology used to collect and purify it. The cheapest sources are facilities that already produce concentrated CO_2 as part of their operations. These include natural gas processing plants, fertilizer production, and bioethanol plants. In such cases, the cost of capturing CO_2 is usually between 20 and 30 € per tonne. However, these sources are limited in availability. Capturing CO_2 from industrial plants such as cement factories, steel mills, or power stations requires the installation of carbon capture units. This increases the cost to around 50 to 100 € per tonne. Biomass-based CO_2 can also be used as a renewable source, but the cost can vary greatly.

It usually falls somewhere between 200 and 400 € per tonne, depending on the type of feedstock, the size of the facility, and the technology applied. DAC, is currently the most expensive method. The cost typically ranges from 300 to 600 € per tonne. However, this is expected to decrease in the future. As the technology improves and scales up, costs could drop to between 50 and 150 € per tonne. [1]. In the short term, using industrial CO_2 sources may be the most cost-effective option. But for e-MeOH production to be truly renewable and carbon-neutral, the use of biogenic CO_2 or CO_2 from DAC would need to be implemented.

2.5 MeOH Properties and Production

MeOH has emerged as a versatile and promising energy carrier, particularly in the context of renewable energy integration and decarbonisation. As a liquid fuel, it offers a practical alternative to fossil-based fuels, with advantages in both physical handling and application. This section provides a comprehensive overview of MeOH's role in the energy transition. It begins by classifying the different types of MeOH based on production routes and feedstock sources. It then evaluates the cost competitiveness of renewable MeOH and presents forecasts for its future production potential. Following this, the physical properties and energy characteristics of MeOH are discussed to highlight its fuel potential. Finally, the broader MeOH value chain is examined, illustrating its relevance across multiple industrial sectors.

2.5.1 Types of MeOH

MeOH can be categorised into two broad groups: conventional fossil-based MeOH (f-MeOH) and renewable MeOH (green MeOH). F-MeOH includes brown, grey, and blue MeOH, which are produced from fossil fuels such as coal, natural gas, and oil. On the other hand, renewable MeOH is produced using sustainable feedstocks and energy sources. It includes:

- **Bio-MeOH:** Produced from biomass or biogas through gasification or reforming.

- **E-MeOH:** Produced from captured CO_2 (either from biogenic sources or direct air capture) and green hydrogen obtained via electrolysis powered by renewable electricity.

These pathways are illustrated in Figure 2.9.
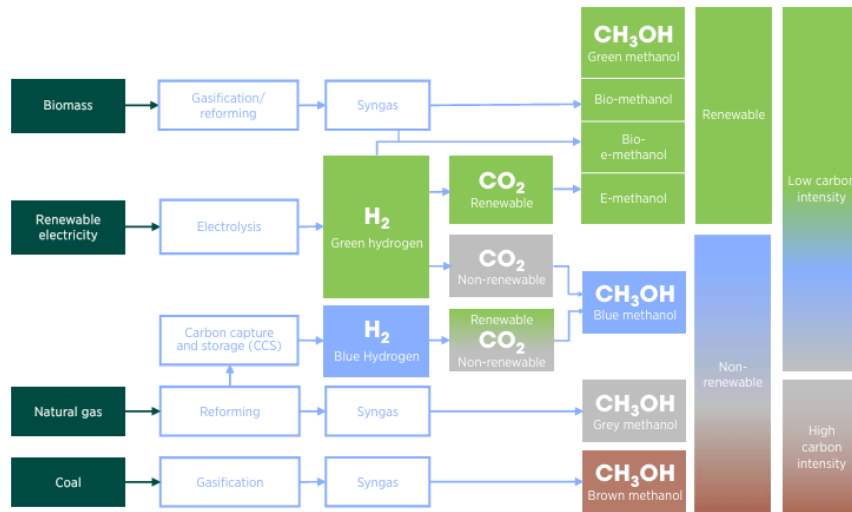
Figure 2.9: MeOH production pathways based on feedstock and energy sources [1].

2.5.2 Cost Competitiveness of Renewable MeOH

Currently, the production cost of renewable MeOH is significantly higher than that of f-MeOH. E-MeOH in particular, when derived from CO_2 via direct air capture and green hydrogen, have high costs due to the energy-intensive processes and immature technologies involved. However, cost projections indicate that as electrolyser efficiency improves, renewable electricity becomes more affordable, and carbon pricing mechanisms are adopted, the production cost of renewable MeOH is expected to approach that of conventional MeOH. This trend is shown in Figure 2.10, where the cost evolution for different types of MeOH is compared. While bio- and e-MeOH remain expensive at present, mature production technologies and favourable policy support could make them competitive in the near future.
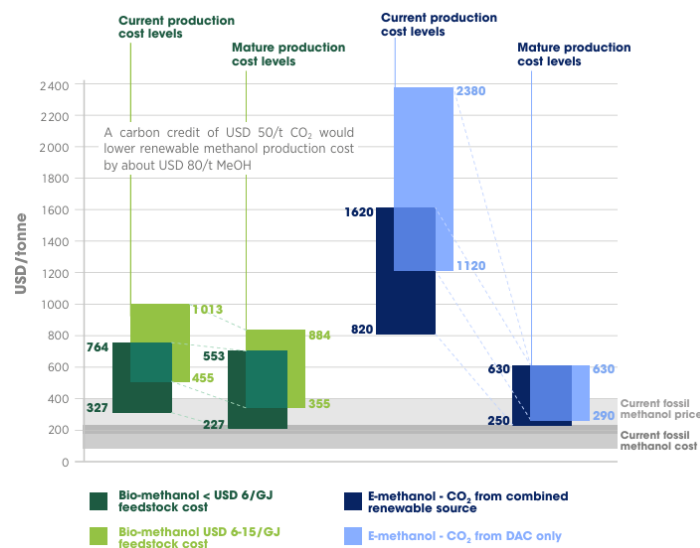
Figure 2.10: Current and projected production costs of MeOH types and competing fuels [1].

2.5.3 MeOH Forecast

At present, nearly 99% of global MeOH is derived from fossil-based sources. Only a small fraction comes from bio- and e-MeOH routes. However, with expected declines in renewable MeOH production costs and increasing climate policy pressures, the production landscape is projected to shift substantially by 2050.
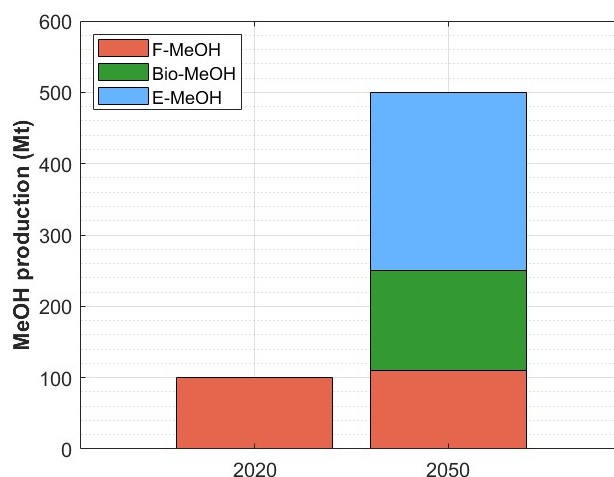
Figure 2.11: Current and projected MeOH production by [1] in 2020 and 2050.

The forecast 2.11 indicates that e-MeOH and bio-MeOH will jointly be more than half of total MeOH production by mid-century, displacing a significant share of f-MeOH and contributing to lower carbon intensity in industrial and energy applications.

2.5.4 Physical Properties and E-MeOH System Design

MeOH is a simple alcohol with favourable storage and transport characteristics. It remains in liquid form under ambient temperature and pressure, with a boiling point of 337.75 K and a freezing point of 175.55 K. Its volumetric energy density is approximately 17.8 MJ/L, which is higher than that of both compressed hydrogen at 700 bar and liquid hydrogen [35]. The gravimetric energy density of methanol is 22.4 MJ/kg, which is about half the value of conventional petrol [36].These characteristics make MeOH attractive as a transportation fuel. Additionally, its low volatility and relatively low toxicity enhance its suitability as a marine fuel, especially for heavy-duty and long-distance transport.

To be viable in global markets, e-MeOH must meet strict quality specifications, such as AA or IMPCA chemical-grade MeOH standards. This necessitates a purification system, such as distillation, to achieve and maintain the required product purity. Unlike conventional MeOH plants that operate continuously at steady loads, e-MeOH systems must accommodate the variability of renewable electricity. This intermittency presents challenges in the synthesis and distillation stages, particularly with regard to process control and system responsiveness. As hydrogen generation fluctuates, the downstream units must be capable of stable performance under varying input conditions. Furthermore, switching from syngas-based feedstock to CO_2-rich gas alters reactor equilibrium and increases water formation, affecting catalyst performance and reactor design.

Chapter 3

Problem Formulation

3.1 Electrolyser Technology Selection

This report evaluates available electrolyser technologies for hydrogen (H2) production in power-to-MeOH (PtMeOH) systems, with a focus on Proton Exchange Membrane Electrolysis (PEMEL). Only a PEM-based model is developed in these report, but capital expenditure (CAPEX) estimation for both PEM and Alkaline Electrolysis (AEL) are included to provide a comprehensive overview of viable options. (5

AEL is a mature and historically dominant technology, widely used in earlier studies and pilot plants due to its relatively low capital costs and simple design (e.g. Y.Zheng et al. (2022) [9]). However, despite its higher CAPEX at the moment, PEMEL is more often selected for real-world projects lately, particularly where flexibility of operation is required. Examples include the Kassø e-MeOH plant in Denmark [10] and Iberdrola's Puertollano facility in Spain [37], both using PEM electrolysers powered by renewable energy. The choice of PEM in this report is driven by its superior dynamic performance and compact design. Industry trends and recent studies indicate that PEM costs are declining more rapidly than those of AEL, and are expected to become comparable in the near future due to manufacturing scale-up and policy support. [38, 39] Also, studies shows that PEMEL can withstand a higher pressure than other electrolysers, so it could be possible to build a system that requires smaller compressor, or not compressor at all, before H_2 enters the MeOH synthesis (MS) reactor [15]. A possible limitation to the large-scale deployment of PEMEL is the use of rare and expensive catalyst materials such as iridium, primarily sourced from regions like South Africa and Russia. The long-term availability and pricing of these materials introduce uncertainty that is not quantified in this analysis.

Solid Oxide Electrolysis (SOEL) is also a promising technology, offering the highest efficiency due to high-temperature operation. However, its lack of operational flexibility at the current development phase makes it unsuitable for integration with variable renewable energy, and it is therefore excluded from the scope of this study. However, there is a potential the operational flexibility of SOEL will be improved, so this could also be a competitive technology in the future.

In summary, while the techno-economic model is built around PEMEL, the report includes comparative CAPEX data for both PEMEL and AEL to support broader insight into technology selection.

3.2 Problem Configuration

Following the analysis of current challenges and technological foundations in e-MeOH production, the problem can be configured as an integrated PtMeOH production system designed to convert surplus renewable electricity from the grid into e-MeOH through optimal operational strategies. The configuration comprises three main subsystems connected

in series: a PEMEL system with rated power of 50 MW, MeOH synthesis and distillation system (MSD), and finally optimisation model 3.1.

A PEMEL system converts surplus electrical energy and water into H_2 and O_2. The electrolyser is designed to operate dynamically, responding to electricity price fluctuations and grid conditions while maintaining safe operational parameters. MSD system consists of an integrated process combining CO_2 hydrogenation in a catalytic reactor and distillation for product purification. The system uses industrial CO_2 emissions and operates under dynamic conditions to accommodate for varying H_2 supply rates from PEMEL. Optimisation is done at the end to find operational scheduling based on real-time electricity prices and production demands, targeting cost-effective e-MeOH production while maintaining product quality specifications. The system operates within a dynamic electricity market environment where prices fluctuate hourly.
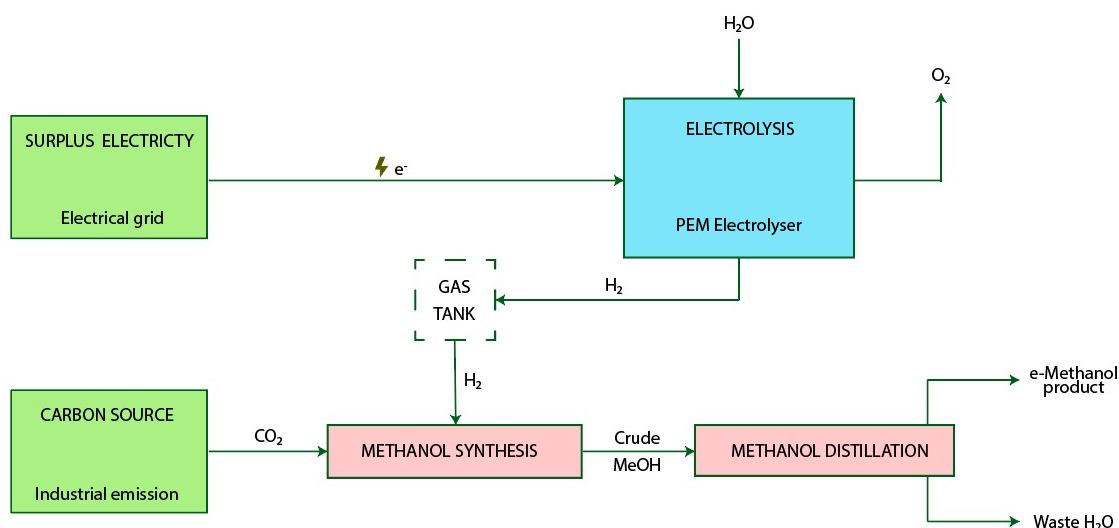
Figure 3.1: Overview of the PtMeOH system configuration developed in this thesis

3.3 Problem Statement

Despite the technological maturity of individual components in e-MeOH production systems (TRL 8-9), three critical challenges still prevent its commercial deployment:

- Current e-MeOH production costs significantly exceed fossil MeOH prices

- Operational strategies of e-MeOH plants are limited in the available resources, indicating that existing plants may lack quality operational strategies. The inability to optimise production scheduling based on price fluctuations results in suboptimal economic performance.

- The dynamic coupling between PEMEL and MSD systems under varying operational conditions is not well understood, leading to conservative operational strategies that sacrifice economic potential for system stability. Usage of big H_2 tanks in between

the systems is considered in some cases, but here it is not considered as viable option due to limitations of H_2 tanks explained in 2.3

This study aims to address these challenges through three main objectives:

1. **Development of steady-state and dynamic models** for the main units of e-MeOH production, including electrolyser systems and MSD processes

2. **Evaluation of system flexibility** related to dynamic behaviour of developed systems

3. **Optimisation of flexible operation** targeting cost-effective e-MeOH production while meeting defined demand and maintaining product quality

The solution approach involves developing integrated modeling frameworks, implementing optimisation strategies for operational scheduling, and validating the system performance under realistic operating conditions to establish the technical and economic feasibility of developed models.

Chapter 4

Methodology

This chapter presents the modelling approach used to simulate the main components of the system. It includes the development of a PEM electrolyser (PEMEL), a MeOH synthesis (MS), and a MeOH distillation (MD) model, each described in detail in the following sections. Also, it covers the development of surrogate model, calculation of capital expenditures (CAPEX) and the optimisation model. To make this chapter self-contained, some equations introduced previously are rewritten where relevant. All constants and relevant other values are listed in their relevant tables.

4.1   Steady State Model Of PEM Electrolyser

In order to build a dynamic model of the electrolyser, first steady state model must be developed. The model describes electrochemical and physical behaviour of the system, and is based on V.Liso et al. (2018) [40], R.Datta et al. (2016) [41], L.Garibaldi (2022) [23]and S.Asiaban et al. (2024) [42]. The model is developed in MathWorks's graphical simulation environment called Simulink. It consists of several subsystems that interacts with each other: Anode, Cathode, Membrane, Voltage, Efficiency and thermal module. The constants not commented throughout the section are presented in a Table 4.2 at the end of the section.

Hypotheses made for the simplification of the system are:

- Hydrogen (H_2), oxygen (O_2), and water (H_2O) in a vapour phase are assumed to be ideal gasses

- H_2O concentration gradient is assumed to be linear

- Ohmic overpotential in the electrode plates is neglected

- Some of the parameters are set up as fixed values (e.g. osmotic drag coefficient, diffusivity of hydrogen ions (H^+), etc.)

- Only input flow to the electrolyser is H_2O on the anode side

- There are no energy losses due to radiation or convection

- Temperature is uniform across the cell

As mentioned in the previous chapter, water is fed to the electrolyser on the anode side, where oxidation reaction occurs due to the applied electric current, and water is decomposed to H^+, O_2, and electrons (Eq. 4.1). Electrons travel through the electric circuit, and meet with the H^+, that passed through the proton-conductive membrane, on the cathode side. Connection of the H^+, and electrons is called reduction reaction (Eq.4.2). O_2 produced in the oxidation reaction exits the electrolyser on the anode side, together with the

surplus H_2O The overall reaction is called redox reaction, and is shown in Equation 4.3.

$$\text{Anode:} \quad 2H_2O \rightarrow 4H^+ + 4e^- + O_2 \tag{4.1}$$

$$\text{Cathode:} \quad 4H^+ + 4e^- \rightarrow 2H_2 \tag{4.2}$$

$$\text{Overall:} \quad H_2O \rightarrow H_2 + \tfrac{1}{2}O_2 \tag{4.3}$$
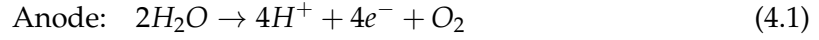
4.1.1 Anode Module

The molar balances of the species on the anode side of the electrolyser are described according to the law of conservation of mass (Eq.4.4 and 4.5), as follows:

$$\dot{N}_{H_2O,an} = \dot{N}^{in}_{H_2O,an} - \dot{N}^{cons}_{H_2O,an} - \dot{N}^{mem}_{H_2O} - \dot{N}^{out}_{H_2O,an} \tag{4.4}$$

$$\dot{N}_{O_2,an} = \dot{N}^{in}_{O_2,an} + \dot{N}^{gen}_{O_2,an} - \dot{N}^{out}_{O_2,an} \tag{4.5}$$

Where $\dot{N}^{in}_{H_2O,an}$ and $\dot{N}^{out}_{H_2O,an}$ are inlet and outlet flows of H_2O, respectively, while $\dot{N}^{in}_{O_2,an}$ and $\dot{N}^{out}_{O_2,an}$ are inlet and outlet flows of O_2, respectively. Of course, inlet flow of O_2 is zero in this case, but is shown here only to have a complete molar balance equation. $\dot{N}^{cons}_{H_2O,an}$ and $\dot{N}^{gen}_{O_2,an}$ are the flow of consumed H_2O and the flow of generated O_2, respectively, and they are calculated with the Faraday's first law of electrolysis (Eq.4.6):

$$\dot{N}^{cons}_{H_2O,an} = \frac{NI}{2F} \qquad\qquad \dot{N}^{gen}_{O_2,an} = \frac{NI}{4F} \tag{4.6}$$

where N is a number of cells, I is a current, and F is a Faraday constant. $\dot{N}^{mem}_{H_2O}$ is the flow of H_2O that passes through the cell's membrane due to few physical phenomena that will be explained below in this section. In the anode module, molar fluxes (Eq.4.7) and partial pressures are also calculated, since they will be used later in other modules.

$$\dot{n}_{O_2} = \frac{\dot{N}^{gen}_{O_2}}{A} \qquad\qquad \dot{n}_{H_2O,an} = \frac{\dot{N}^{cons}_{H_2O} + \dot{N}^{mem}_{H_2O}}{A} \tag{4.7}$$

A represents the total are of MEA (Membrane Electrode Assembly). Partial pressure is calculated with Dalton's law (Eq. 4.8). p_{H_2O} is a partial pressure of H_2O, which is assumed to be the same as the saturated pressure of H_2O ($p_{H_2O,sat}$), due to the assumption that the electrolyser is well-humidified. It is calculated using Equation 4.9.

$$p_{O_2} = P_{anode} - p_{H_2O} \tag{4.8}$$

$$p_{H_2O,sat} = p_{H_2O} = 10^{A - \frac{B}{C+T}} \cdot 133.322 \tag{4.9}$$

Table 4.1: Antoine equation parameters, with T [°C] and p_{sat} [Pa]

A	B	C	T_{min}	T_{max}
8.07131	1730.63	233.426	1	100

4.1.2 Cathode Module

The cathode module is built similarly to the anode module. Firstly, mole balances are presented:

$$\dot{N}_{H_2O,cat} = \dot{N}^{in}_{H_2O,cat} + \dot{N}^{mem}_{H_2O} - \dot{N}^{out}_{H_2O,cat} \tag{4.10}$$

$$\dot{N}_{H_2,cat} = \dot{N}^{in}_{H_2,cat} + \dot{N}^{gen}_{H_2,ca} - \dot{N}^{out}_{H_2,cat} \tag{4.11}$$

$\dot{N}^{in}_{H_2O,cat}$ and $\dot{N}^{in}_{H_2,cat}$ presents H_2O and H_2 inputs on the cathode side, respectively, which are zero, so these terms are neglected in the model. $\dot{N}^{out}_{H_2O,cat}$ and $\dot{N}^{out}_{H_2,cat}$ presents the outputs of the species on the cathode side, and $dotN^{gen}_{H_2,ca}$ is the flow of generated H_2 on the cathode side. It can be calculated using Faraday's law (Eq. 4.6):

$$\dot{N}^{gen}_{H_2,cat} = \frac{nI}{2F} \tag{4.12}$$

Same as in anode module, molar fluxes (Eq.4.13) and partial pressures (Eq.4.14) are also calculated, since they will be used later in other modules.

$$\dot{n}_{H_2} = \frac{\dot{N}^{gen}_{H_2}}{A} \qquad \dot{n}_{H_2O,cat} = \frac{\dot{N}^{mem}_{H_2O}}{A} \tag{4.13}$$

$$p_{H_2} = P_{cathode} - p_{H_2O} \tag{4.14}$$

4.1.3 Membrane Module

Membrane module is built in order to calculate the flow of H_2O passing through the membrane ($\dot{N}^{mem}_{H_2O}$) because of electro-osmotic drag, pressure gradient, and concentration gradient:

$$\dot{N}^{mem}_{H_2O} = \dot{N}^{eod}_{H_2O} - \dot{N}^{pg}_{H_2O} + \dot{N}^{conc}_{H_2O} \tag{4.15}$$

$$\dot{N}^{eod}_{H_2O} = \frac{n_d I}{F} \qquad \dot{N}^{pg}_{H_2O} = K_{darcy} \frac{A\rho_{H_2O}\Delta p}{\delta_{mem}\mu_{H_2O}M_{H_2O}} \qquad \dot{N}^{conc}_{H_2O} = AD_w \frac{C^{mem}_{H_2O,cat} - C^{mem}_{H_2O,an}}{\delta_{mem}} \tag{4.16}$$

$\dot{N}^{eod}_{H_2O}$ represents the flow caused by electro-osmotic drag, which is caused by proton movement through the membrane, that drag some of the water particles with them. Therefore, this phenomena drags water from anode to cathode side. It is dependent on n_d, electro-osmotic drag coefficient, which is taken as a constant in this report, based on A.Awasthi et al. (2011) [43]. $\dot{N}^{pg}_{H_2O}$ is the flow due to pressure difference across the membrane, is calculated using Darcy's law, and it is going from higher to lower pressure side. K_{darcy} is the membrane permeability to H_2O, ρ_{H_2O} is the density, δ_{mem} is the membrane thickness, μ_{H_2O} is the water viscosity, and M_{H_2O} is its molar mass. $\dot{N}^{conc}_{H_2O}$ is the water flow due to the water diffusion, where H_2O is moving from higher concentration (anode) to lower concentration (cathode) region. D_w is the membrane water diffusion coefficient, and $C^{mem}_{H_2O,cat}$ and $C^{mem}_{H_2O,an}$ are H_2O concentration between the membrane and cathode, or anode, respectively. These are calculated with Fick's first law, which explains that flux of a species across the membrane is proportional to the difference in concentration between the two sides (Eq.

4.17):

$$C_{H_2O,cat}^{mem} = C_{H_2O,cat}^{ch} + n_{H_2O,cat}\frac{\delta_{cat}}{D_{eff,cat}^{H_2-H_2O}} \qquad C_{H_2O,an}^{mem} = C_{H_2O,an}^{ch} - n_{H_2O,an}\frac{\delta_{an}}{D_{eff,an}^{O_2-H_2O}} \qquad (4.17)$$

$C_{H_2O}^{ch}$ is the H_2O concentration in the electrode channel, calculated with the equation 4.18, δ_{cat} and δ_{an} are thicknesses of the electrodes, and $D_{eff,cat}^{H_2-H_2O}$ and $D_{eff,an}^{O_2-H_2O}$ are effective binary diffusion coefficients for cathode and anode, respectively. The effective binary diffusion coefficient is a coefficient of a 2 species through a medium, and is calculated with Equation 4.19 (A and B represents the species, and the relevant values are given in the Table 4.2).

$$C_{H_2O,ch} = \frac{\rho_{H_2O}}{M_{H_2O}} \qquad (4.18)$$

$$D_{eff,A-B} = D_{A-B}\,\varepsilon\left(\frac{\varepsilon_f - \varepsilon_p}{1 - \varepsilon_p}\right)^{\alpha_{exp}} \qquad (4.19)$$

$$D_{A-B} = \left(a\left(\frac{T}{\sqrt{T_{c,a}T_{c,b}}}\right)^b (p_{c,a}p_{c,b})^{1/3}(T_{c,a}T_{c,b})^{5/12}\left(\frac{1}{M_mA} + \frac{1}{M_mB}\right)^{1/2}\right)\frac{1}{p} \qquad (4.20)$$

4.1.4 Voltage Module

The purpose of voltage module is the calculation of cell voltage, V_{cell} (Eq. 4.21), which is further used for the calculation of efficiency and generated heat. It is a sum of open circuit voltage, V_{OC}, and different overpotentials (voltage losses).

$$V = V_{OC} + V_{act} + V_{ohm} + V_{conc} \qquad (4.21)$$

$$V_{OC} = V_{rev} + \frac{RT}{2F}\ln\left(\frac{p_{H_2}}{p_{cat}}\left(\frac{p_{O_2}}{p_{an}}\right)^{\frac{1}{2}}\right) \qquad V_{rev} = \frac{\Delta G_R^0}{2F} - 0.0009(T - T_{std}) \qquad (4.22)$$

$$V_{act} = \frac{RT}{\alpha_t F}\operatorname{arcsinh}\left(\frac{i}{2i_0}\right) \qquad V_{ohm}^{mem} = \frac{\delta_{mem}}{\sigma_{mem}}i \qquad V_{conc} = \frac{RT}{2F}\ln\left(\frac{C_1}{C_0}\right) \qquad (4.23)$$

V_{OC} is obtained with the expression of the Nerst equation (Eq. 4.22). V_{rev} is the reversible cell voltage, which is calculated with the empirical expression shown above, and ΔG_R^0 is the standard Gibbs free energy. The Activation overpotential (V_{act}) is due to the energy barrier that must be overcome for the electrochemical reaction to occur, and to transfer the electrons from the electrolyte to the electrode. It is calculated using Butler-Volmer equation, can be determined both for anode and cathode, and their sum is the activation overpotential of the cell. Here, i is the current density (Eq. 4.24), and i_0 is the exchange current density (rate at which reactions exchange electrones at equilibrium). i_0 is a product of a membrane roughness factor, γ_M, and the referent exchange current density, i_0^* (calculated using Arhenius equation, the last part of Eq. 4.24). Constants needed to calculate these parameters are taken from V.Liso et al. (2018) [40] and are presented in the Table 4.2.

$$i_0 = \gamma_M i_0^* = \left(\varphi_I m_M \frac{6}{\rho_M d_M}\right)\left(i_{0,ref}\, e^{\left[-\frac{E_a}{R}\left(\frac{1}{T} - \frac{1}{T_{ref}}\right)\right]}\right) \qquad (4.24)$$

The ohmic overpotential arises from the resistance of species to the flow through cell components. It consists of resistance through electrodes, external circuit, bipolar plates,

and membrane, but since the membrane resistance is predominant, it is the only one considered in here. σ_{mem} is a membrane conductivity, calculated with the Bernardi and Verbrugge's expression (Eq. 4.25):

$$\sigma_{mem} = \frac{F^2 C_{H^+} D_{H^+}}{RT} \tag{4.25}$$

The concentration overpotential, V_{conc}, is caused by limitation of mass transport at high current densities, is calculated with an expression of a Nerst equation, and can be determined both for anode and cathode, their sum being the concentration overpotential of the cell. C_1 and C_0 represents the species concentration at operation condition and in standard condition, respectively. To obtain the values of species concentrations, the Fick's first law is used (Eq. 4.17). Note that the Nernst equation can be written using either partial pressures or concentrations because it is originally based on activity. For gases, activity is usually approximated by partial pressure, and for solutions, it is approximated by concentration. These approximations are valid when the gas behaves ideally and the solution is diluted. Also, the temperature and pressure should not be extremely high, since it can also lead to inaccuracies.

4.1.5 Efficiency Module

The efficiency module calculates the efficiency of the electrolyser based on the First law of thermodynamics, which is the principle of energy conservation. This means that the first-law efficiency indicates how much of the input electrical energy (W) is stored as chemical energy in the form of H_2 (ΔH^0_{reac}) (Eq. 4.26). In addition, the Faradaic efficiency, ε_i, is included, which shows how much of the input electric current is actually used for the electrochemical reaction, rather than being lost to side processes. The first-law efficiency can also be described as the product of three factors: Faradaic efficiency (Eq. 4.27), Voltage efficiency, ε_V (Eq. 4.28), and Thermodynamic ("First law potential") efficiency, ε_0 (Eq. 4.29) [41].

$$\varepsilon_{\Delta H} = \frac{\Delta H^0_{reac}}{W} = \varepsilon_i \varepsilon_V \varepsilon_0 \quad W = nFV \tag{4.26}$$

$$\varepsilon_i = 1 - \left(\frac{i_{H_2,X} + i_{O_2,X}}{i} \right) \quad i_{k,X} = \frac{2Fk_k}{\delta_{mem}} p_k \quad k_{H_2} = 6.6 \times 10^{-13} \exp\left(\frac{-21030}{RT} \right) = 2k_{O_2} \tag{4.27}$$

$$\varepsilon_V = \frac{V_0}{V_{cell}} \tag{4.28}$$

$$\varepsilon_0 = \frac{\Delta H^0_{reac}}{2F} \frac{1}{V_0} \tag{4.29}$$

Here, $i_{H2,x}$ and $i_{O2,x}$ are current densities of H_2 and O_2 crossover, respectively. Permeability of the species through a membrane, k_k, is expressed with Arrhenius equation. The subscript k represents either H_2 or O_2 here.

Table 4.2: Model Parameters for steady-state electrolyser model [40, 41]

Description	Parameter	Value	Unit
Thickness of MEA	δ_{mem}	175×10^{-4}	cm
Thickness of anode electrode	$\delta_{el,an}$	8×10^{-3}	cm
Thickness of cathode electrode	$\delta_{el,cat}$	8×10^{-3}	cm
Electro-osmotic drag coefficient	n_d	5	–
Membrane permeability	K_{darcy}	1.58×10^{-14}	cm^2
Water viscosity	μ_{H_2O}	1.1×10^{-2}	$Pa\,s$
Membrane water diffusion coefficient	D_w	1.28×10^{-10}	m^2/s
H$_2$O molar mass	M_{m,H_2O}	18	g mol^{-1}
O$_2$ molar mass	M_{m,O_2}	32	g mol^{-1}
H$_2$ molar mass	M_{m,H_2}	2	g mol^{-1}
Porosity correction factor	ε_f	0.3	–
Percolation threshold factor	ε_p	0.11	–
Gas dependent coefficient a	a	3.640×10^{-4}	–
Gas dependent coefficient b	b	2.334	–
H$_2$O critical temperature	T_{C,H_2O}	647.3	K
H$_2$ critical temperature	T_{C,H_2}	33.3	K
O$_2$ critical temperature	T_{C,O_2}	154.4	K
H$_2$O critical pressure	P_{C,H_2O}	218.3	atm
H$_2$ critical pressure	P_{C,H_2}	12.8	atm
O$_2$ critical pressure	P_{C,O_2}	49.7	atm
Standard Gibbs free energy	ΔG_R	237.2	kJ mol^{-1}
Experimental factor	α_{exp}	0.785	–
Catalyst density (IrO$_2$)	ρ_{M,IrO_2}	11.7	g cm^{-3}
Catalyst density (Pt)	$\rho_{M,Pt}$	21.45	g cm^{-3}
Catalyst loading (anode)	$m_{M,an}$	1.0×10^{-3}	g cm^{-2}
Catalyst loading (cathode)	$m_{M,cat}$	0.3×10^{-3}	g cm^{-2}
Crystallite diameter (anode)	$d_{M,an}$	2.9	nm
Crystallite diameter (cathode)	$d_{M,cat}$	2.7	nm
Catalyst surface-ionomer fraction	φ_I	0.75	–
Exchange current density (anode)	$i_{0,an,ref}$	5×10^{-12}	A/cm^2
Exchange current density (cathode)	$i_{0,ca,ref}$	1×10^{-3}	A/cm^2
Reference temperature	T_{ref}	333	K
Transfer coefficient (anode)	α_{an}	1.2	–
Transfer coefficient (cathode)	α_{ca}	0.5	–
Faraday constant	F	96.485	C mol^{-1}
Gas constant	R	8.314	J mol^{-1} K^{-1}
H$^+$ concentration	C_{H^+}	1000	mol m^{-3}
H$^+$ diffusivity	D_{H^+}	2.4×10^{-9}	m^2/s
Standard enthalpy change	ΔH_{reac}^0	285.8	kJ mol^{-1}
Activation energy (anode)	$E_{a,ano}$	76	kJ mol^{-1}
Activation energy (cathode)	$E_{a,cat}$	4.3	kJ mol^{-1}

4.2 Dynamic Model of PEM Electrolyser

While the steady-state model presented in the previous section provides essential insights into the electrolyser's equilibrium behaviour, real-world applications require understand-

ing of transient phenomena, control strategies, and operational flexibility. This section extends the steady-state model to capture the dynamic behaviour of the PEMEL system, which is crucial for several reasons:

- managing temperature variations during operation,

- implementing safe start-up and shut-down procedures,

- and enabling the model to respond to fluctuating electricity prices.

The dynamic model extends the steady-state electrolyser model by incorporating thermal dynamics and control systems directly in Simulink. It includes a thermal module that calculates heat balance and manages heat removal through a controlled heat exchanger (HEX). The thermal module is connected with other developed modules during the simulation. The following section provides the equations used in the thermal module, present the control strategies employed, and discuss the model's limitations. It is based on Garibaldi (2022) [23], Zheng et al. (2022)[9], Pfenning et al. (2025)[44] and Saari (2005) [45].

4.2.1 Thermal Module

The thermal module is a time-dependent module that calculates the transient temperature change of the electrolyser during operation. Its primary purpose is to determine temperature changes throughout time, caused by surplus or deficit net heat in the system as it is heating up, cooling down, or maintaining constant temperature. The module balances heat gained or lost via various sources and sinks, enabling temperature control through the coordinated operation of a HEX (which cools the system with refrigerant) and an electrical heater (which provides heating when required). The Figure 4.1 shows a simplified diagram of how the modelled system should look like. Together with stacks, HEX and heater, the system must include the separators and dehumidifiers to separate H_2O from H_2 and O_2. All this parts of the PEMEL system, that are managing dynamic flow of species and heat are not modelled independently, but a zero-dimensional (0D) modelling approach is applied, which assumes no spatial variation and treats the entire electrolyser as having uniform properties, such as total system's heat capacity and temperature. This simplification is appropriate for system-level energy balance calculations where detailed temperature distributions within the stack are not required. 0D approximation significantly reduces computational complexity while maintaining sufficient accuracy for dynamic thermal analysis and control applications. Temperature change of the system follows the Equation 4.30:

$$C_{tot}\frac{dT}{dt} = \sum_i \Phi_i - \sum_j \dot{N}_j \Delta h_j \tag{4.30}$$

In this equation, C_{tot} represents a total lumped heat of the system, which is a sum of heat capacities of H_2O that flows inside the system and all electrolyser stacks (Eq. 4.31). Total amount of H_2O constantly circulating in the PEMEL system is estimated to be 10 m^3 here, and heat capacity of H_2O in the system ($C_{water\ in\ system}$) is based on this value. Heat capacity of a single stack is calculated precisely for Siemen's electrolyser Sylzer 300 in Pfenning et al.(2025) [44] and its value is 717 924 JK. $\frac{dT}{dt}$ represents the change of the temperature in time, $\sum_i \Phi_i$ is a sum of all heat rates (Eq. 4.32), and $\sum_j \dot{N}_j \Delta h_j$ is the value
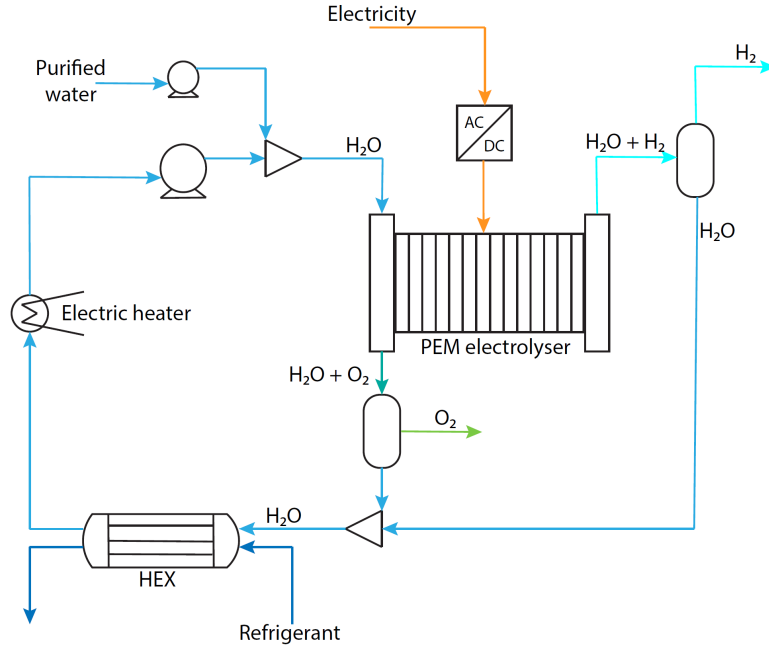
Figure 4.1: Schematic representation of a high-pressure PEMEL system [46]

of heat released from the system with the mass transport out of the system (Eq. 4.33).

$$C_{tot} = C_{water\ in\ system} + C_{stack} \cdot N_{stacks} \tag{4.31}$$

$$\sum_i \Phi_i = \Phi_{gen} + \Phi_{pump} + \Phi_{heater} - \Phi_{loss} - \Phi_{cooling} \tag{4.32}$$

$$\sum_j \dot{N}_j \Delta h_j = \dot{N}_{O_2} \Delta h_{O_2}(T) + \dot{N}_{H_2} \Delta h_{H_2}(T) - \dot{N}_{H_2O}^{inj} \Delta h_{H_2O}(T_{amb}) \tag{4.33}$$

Φ_{gen} is a heat rate corresponding to the heat released from the electrolyser thanks to inefficiencies in nonspontaneous electrochemical reactions, and other losses, like ohmic overpotential (Eq. 4.34). At first, electrolyser absorbs heat by endothermic reaction, but exothermic processes caused by irreversibilities (losses) are usually more significant, so electrolyser is realising heat. In the equation (Eq. 4.34), V_{tn} is thermal neutral voltage which has the value of 1.48 V at standard conditions, and it represents the voltage at which there is no heat loss or gain in the electrolyser.

Φ_{pump} is a heat flux transferred to H_2O via friction losses, which is accounted here in the equation thanks to the large H_2O flow throughout the system (Eq. 4.35). ρ_{molar,H_2O} here is a molar density of water with a value of 54604 mol/m^3, ΔP_{pump} is a pressure difference that pump head which is assumed to be 2 bars, and is caused by pressure losses in the system. efficiency of electrical motor (η_{motor}) and pump's mechanical efficiency (η_{pump}) are both assumed to be 0.75.

Φ_{heater} is a heat flux provided by the electrical heater and is usually zero, except when the system is heating up before running. Later on, it is not necessary, so it is turned off.

Φ_{loss} is a heat flux lost to the environment (Eq. 4.36), $T_{ambient}$ is the outdoor temperature assumed to be 298.15 K, and R_{th} is a thermal insulation factor, which is calculated precisely for one stack of Siemen's electrolyser Sylzer 300 in Pfenning et al.(2025) [44] and its value is 1/67 K/W.

$\Phi_{cooling}$ is a heat taken away with a HEX, and it is calculated using $\epsilon - NTU$ method 4.37.

$$\Phi_{gen} = NI(V_{cell} - V_{tn}) \tag{4.34}$$

$$\Phi_{pump} = \frac{\dot{N}_{H_2O,an}}{\rho_{molar,H_2O}} \Delta P_{pump} \left(\frac{1}{\eta_{motor}\eta_{pump}} - 1 \right) \tag{4.35}$$

$$\Phi_{loss} = \frac{T - T_{ambient}}{R_{th}} \tag{4.36}$$

$$\Phi_{cooling} = \Phi_{cooling}^{max} \epsilon \tag{4.37}$$

In this project, coaxial tube HEX in parallel flow is considered, based on Garibaldi (2022)[23]. It has two streams that are flowing in the same direction in separated pipes, while heat is transferred from a hot stream to a cold one (see Figure 4.2).

$\epsilon - NTU$ **method**

$\epsilon - NTU$ method is a way of calculating the heat rate exchanged in the HEX without requiring 4 temperature values: the inlet and outlet ones for both streams. This alternative approach for calculating exchanged heat rate requires only inlet temperatures of both streams. With these 2 values, the maximal theoretical heat flux that can be exchanged between streams is calculated ($\Phi_{cooling}^{max}$) with Equation 4.38. This term is then multiplied with the effectiveness factor (ϵ), which is, for parallel flow HEX, calculated with equation 4.39. In this equation, NTU represents a non-dimensional value called the number of transfer unit, and r_c is a heat capacity ratio, a function of stream's heat capacity rates (Eq. 4.42). The value U in the expression for NTU is overall heat transfer coefficient, which has a value of 1500 W/(m²K), and is taken from Saari (2005) [45]. The area of HEX (A_{ex}) is estimated for this case to be 700 m², and is also based on the Saari (2005) [45]. The temperature of the refrigerant (T_{refr}^{in}) is assumed to be 293.15 K.

$$\Phi_{cooling}^{max} = C_{min} \left(T^{in} - T_{ref}^{in} \right) \tag{4.38}$$

$$\epsilon = \frac{1 - \exp\left[-NTU(1 + r_c) \right]}{1 + r_c} \tag{4.39}$$

$$C_{max} = \max(C_h, C_c); \qquad C_{min} = \min(C_h, C_c); \tag{4.40}$$

$$C_h = \dot{m}\, c_{H_2O}; \quad C_c = \dot{m}_{refr}\, c_{refr} \tag{4.41}$$

$$NTU = \frac{UA_{ex}}{C_{min}}; \qquad r_c = \frac{C_{min}}{C_{max}}; \tag{4.42}$$

PI controller

In the developed model, the refrigerant mass flow rate ($\dot{m}_{refr}$) is not fixed but dynamically controlled to maintain the electrolyser temperature constantly at 338 K. A controller, positioned at the hot stream outlet of the HEX, adjusts the refrigerant valve to match the net heat rate generated by the PEMEL system (Figure 4.2). To ensure sufficient heat removal from the stack, the system is designed to supply H_2O to the electrolyser at a flow rate 65 times greater than the amount of H_2O that is decomposed in the electrolyser. This excess H_2O absorbs the heat produced in the stack and then flows to the HEX, where it is cooled by transferring heat to the refrigerant. After cooling, feed H_2O equal to the amount elec-

trolytically converted previously in the stack is added, and the combined flow is pumped back to the electrolyser, completing the thermal management loop (Figure 4.1).
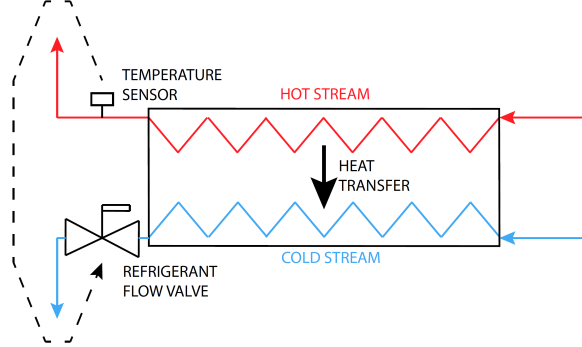
Figure 4.2: Qualitative representation of the HEX [23]

The controller used for the purpose of regulating the refrigerant mass flow in this case is a proportional-integral (PI) controller. It works on the principle that it receives the temperature error, defined as the difference between the desired and actual temperature (Eq. 4.43), and computes the control signal based on its proportional (K_p) and integral contributions (K_i) (Eq. 4.44).

$$e(\tau) = T_{ref} - T_{stack} \tag{4.43}$$

$$u(t) = K_p \cdot e(\tau) + K_i \cdot \int_0^t e(\tau) \, d\tau \tag{4.44}$$

PI controllers are widely adopted in industrial applications due to their simplicity, robustness, and ability to eliminate steady-state errors. Unlike open-loop systems, which cannot correct for disturbances, the PI controller uses continuous feedback to iteratively adjust the system input. It combines two terms: a proportional term that reacts to the current error, and an integral term that accounts for the accumulated error over time. Together, these ensure that the system quickly and smoothly converges to the setpoint.

To further improve the reliability of the control, an anti-windup mechanism is implemented in this case. In systems like this one, where the control signal represents a physical quantity such as refrigerant mass flow, it's important to prevent the controller from producing unrealistic outputs, like negative flow rates. During large disturbances or long-lasting errors, the integral term can accumulate too much, a problem known as integral windup, which can cause the system to overshoot or respond too slowly. To avoid this, a saturation block is introduced to limit the controller output to only positive values, and a feedback loop is added to prevent the integral term from continuing to grow when the output hits this limit. This so called "anti-windup mechanism" was essential for stable operation of the thermal control system. Without it, the model became unstable and could not maintain the desired temperature. Figure 4.3 shows the simplified PI controlled close loop, with additional anti-windup mechanism.
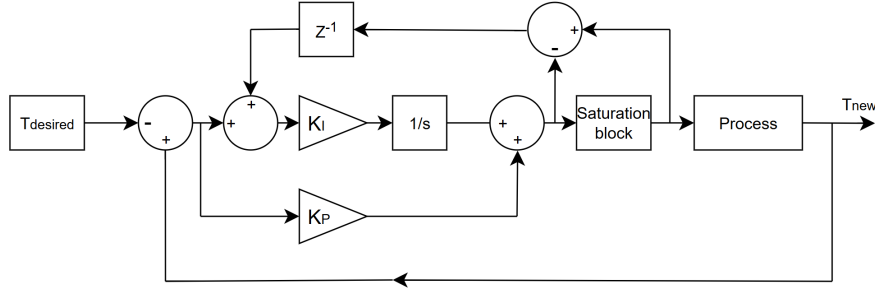
Figure 4.3: PI controller with anti-windup mechanism logic

4.2.2 Constant Pressure Assumption

In this model, pressure is assumed to remain constant throughout the electrolyser system, despite the fact that in reality, pressure dynamics do occur in various components such as separators, dehumidifiers, and gas channels. This simplification is justified for several reasons.

First, most pressure variations take place outside the electrolyser stack, in auxiliary units where their impact on core electrochemical performance is minimal. Moreover, the system usually includes additional flow control components such as smaller compressors or pumps, which compensate for pressure losses and maintain near-steady conditions within the stack. These pressure drops are implicitly accounted for in the equation for energy consumption of the pumps (Eq. 4.35), eliminating the need for explicit pressure modelling.

Second, during short shut-off periods, such as daily operating cycles, it is common practice not to depressurise the system. Frequent pressure cycling is known to contribute to membrane degradation, so maintaining stable pressure during brief shutdowns is beneficial for system longevity. This aligns with operational strategies in commercial high-power systems.

Furthermore, as discussed by Garibaldi (2022) [23], pressure variations tend to influence the system gradually over time, unlike current or temperature, which respond more immediately to changes in power input. From a system-level modelling perspective, omitting dynamic pressure control allows the model to focus on faster, more impactful variables, such as current density and temperature, without significantly compromising accuracy in the operational scenarios considered here.

Now, after whole PEMEL model is explained, a scheme of the built system in Simulink is presented below in the Figure 4.4, showing how different model interact with each other during the calculation of result.
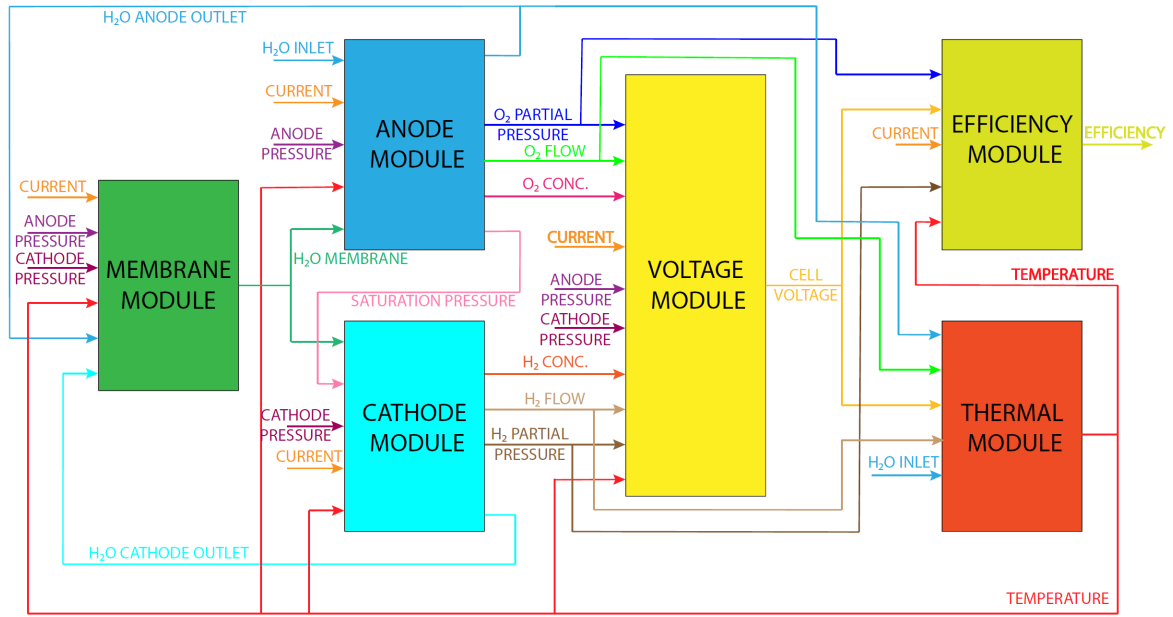
Figure 4.4: Scheme of the Simulink model showing interactions between modules

4.2.3 Operational Modes

Electrolysers, particularly when operated dynamically in response to electricity market fluctuations, require well-defined operational modes to ensure good performance and meet its production demand.

The developed system of the electrolyser includes 3 main states (modes): off state, standby state, and running state. Off state considered here can also be referred to as the cold standby state in the literature. In this state, the electrolyser is not producing H_2, and heat required to keep the electrolyser warm is not provided, but the system is still pressurised. The reason for keeping the system pressurised here is because constant pressure changes can degrade the electrolyser (see 4.2.2), and it would take more time to turn it on again. Therefore, pressure changes are not considered here. Purpose of this state is not to spend energy for keeping the system in a standby for a long time if there is a long period of high electricity prices. Standby state considered here can also be referred to as the hot standby state in the literature. Here, the system is pressurised, and the temperature is kept just below the operating temperature with the electrical heater (controlled with PI controller), so the electrolyser is capable of starting the production in a short interval. There is no production of H_2 in this state as well. Running state is a state where there is a production of H_2 and the system is modelled in a way that the electrolyser can operate on various loads.

Between these 3 main stages, there are 4 transitional stages: cold start, hot start, shutdown transition, and standby transition. Transitioning between these states allows the electrolyser to adapt to variations in electricity prices and system demands. All these states are illustrated in the triangular state diagram below (Figure 4.5):
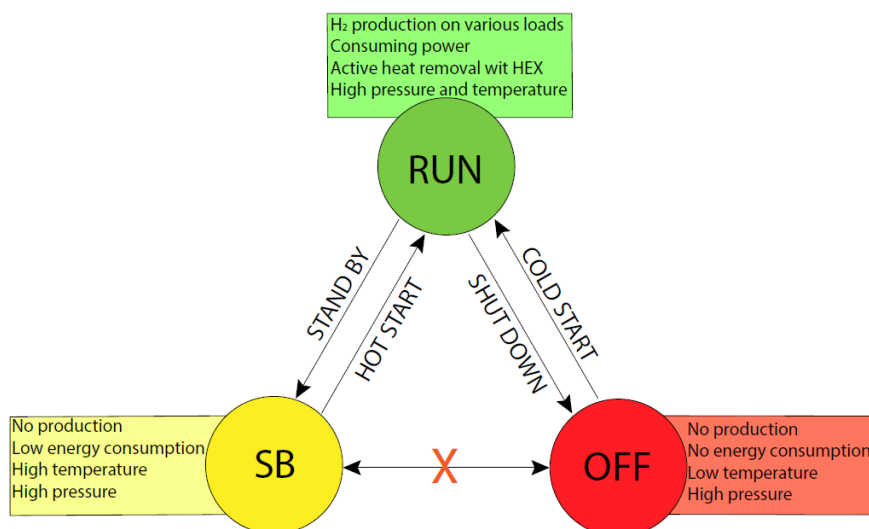
Figure 4.5: Representation of states and mutual state transitions

PEMELs are sensitive to rapid changes in temperature and load, which can stress internal components and reduce durability of the stack. To avoid degradation and ensure reliable performance, transitions between operational modes must be carefully defined and controlled. The key parameter here is temperature rise rate. Temperature rise data for PEMELs is rarely given explicitly, but reported studies show it typically falls within a range of 0.58–1.36 K/min. Rauls et al. (2023) [47] tested several warm-up strategies on a 100 kW PEM system, achieving operational temperatures (298 K to 348 K) in 53 to 86 minutes, depending on the method, highlighting the importance of combining gradual current increase with external heating. Barisione (2024) [22] observed similar rates in a 1.1 MW dynamic model, with average heating at 1.1 K/min and peaks at 1.36 K/min, showing a strong dependence on the stack's thermal capacity. Although some manufacturers claim cold start can be done within 5 minutes, these probably refer to time-to-operation rather than reaching full thermal stability. More precise data on this matter is not found. A manufacturer called Enapter [48], for instance, reports 1 K/min for alkaline electrolyser (AEL) systems. Rapid heating can lead to material stress and degradation, especially in large systems where thermal gradients pose additional risks. For this reason, conservative ramp rates are typically preferred to ensure uniform heating and protect long-term durability.

To address this, a cold start involves a controlled increase in temperature using both a low-level current input and an auxiliary electrical heater, maintaining a nearly constant temperature rise. The hot start, on the other hand, uses only the current load to return the stack to operating temperature from standby. Since reliable operational data for these transitions are limited and often vary with scale and system type, strategies used here are based on safety margins from literature and conservative engineering judgment, ensuring realistic system behaviour within safe limits. This strategies are discussed more detailed in Section 4.9.

4.3 Methanol Synthesis

A steady-state model of the MS process has been developed to define the system configuration, establish operating conditions, and generate key design parameters. In addition,

catalyst behaviour and kinetic parameters are incorporated to ensure an accurate representation of reaction mechanisms in the reactor. As with the PEMEL, the steady-state model forms a critical foundation before dynamic simulations can be implemented.

4.3.1 System Configuration

The MS system begins with two primary feed streams: H_2 and CO_2. These gases are mixed and then preheated before entering the fixed-bed reactor (R1). Within the reactor, MeOH is primarily produced via the hydrogenation of CO_2, as described by Equation 4.45, while the Equation 4.46 also occurs as a competing side reaction. The reactor effluent contains a mixture of MeOH, H_2O, unreacted H_2 and CO_2, and CO as a byproduct. To separate these components, the outlet stream (S31) is first cooled and sent to a vapour–liquid separator (SEP). Here, the light gases (VAP), mainly unreacted H_2, CO_2 and CO, are separated from the heavier liquid phase, which is rich in MeOH and H_2O.

Given the relatively low single-pass conversion typical of MS, a recycle loop is implemented to enhance overall yield. The separated light gases are compressed in a compressor (COMP) and recirculated back to the reactor inlet to maintain pressure compatibility with fresh feed streams. To ensure numerical stability during simulation and to prevent excessive accumulation of inert components, a purge stream (PUR) is introduced upstream of the recycle compressor. While increasing the purge ratio lowers the recycle flow and reduces reactor volume and capital costs, it also results in greater CO_2 losses and higher greenhouse gas emissions. Therefore, a compromise was made by selecting a purge ratio of 0.1%, balancing simulation stability with environmental and process efficiency. The liquid stream from the bottom of the first separator (LIQ) is routed to a second separation unit (SEP1). This step removes any remaining dissolved gases (LG) and helps condition the product stream (CR-METH) for the downstream distillation process, where the final MeOH purity is achieved. A schematic representation of this configuration is shown in Figure 4.6.
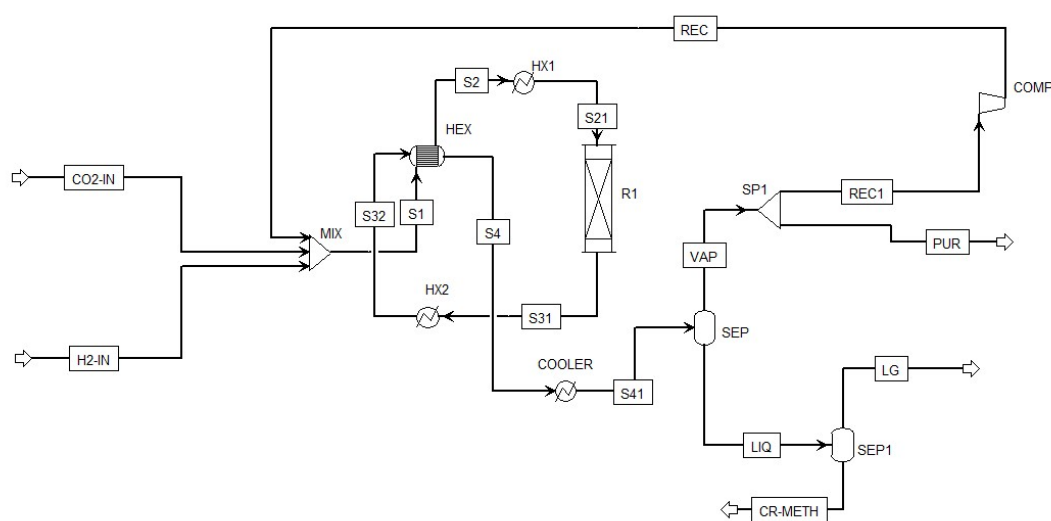
Figure 4.6: Process flow diagram for MS system.

4.3.2 Reaction Chemistry

As previously mentioned, e-MeOH is produced via the hydrogenation of CO_2. This process involves two main chemical reactions:

$$CO_2 + 3H_2 \rightleftharpoons CH_3OH + H_2O \quad \Delta H_{298} = -41.2 \text{ kJ mol}^{-1} \tag{4.45}$$

$$CO_2 + H_2 \rightleftharpoons CO + H_2O \quad \Delta H_{298} = +49.5 \text{ kJ mol}^{-1} \tag{4.46}$$
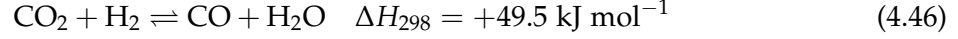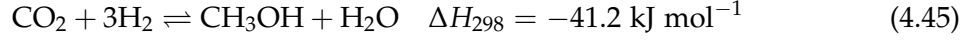
Equation 4.45 describe MS via the hydrogenation of CO_2, while Equation 4.46 represents the reverse water-gas shift (RWGS) reaction. The commercial catalyst used in this study is $Cu/Zn/Al_2O_3$, which remains the industry benchmark for low-temperature MS. Its widespread application is supported by extensive research and industrial deployment ([18, 49]).

4.3.3 Kinetic Modelling

In this study, the kinetic expressions for the MS and RWGS reactions are adopted from the model developed by V.Bussche et al. (1996) [50]. The rate equations used to describe the reaction rates of Equations 4.45 and 4.46 are presented in Table 4.3:

Table 4.3: Reaction kinetics

Reaction kinetics
$r_{\text{MeOH}} = k_1 \dfrac{P_{CO_2} P_{H_2} - K_{eq1}^{-1} P_{\text{MeOH}} P_{H_2O} / P_{H_2}^2}{(1 + K_a P_{H_2O}/P_{H_2} + K_b P_{H_2}^{0.5} + K_c P_{H_2O})^3}$
$r_{\text{RWGS}} = k_2 \dfrac{P_{CO_2} - K_{eq2} P_{H_2O} P_{CO} / P_{H_2}}{1 + K_a P_{H_2O}/P_{H_2} + K_b P_{H_2}^{0.5} + K_c P_{H_2O}}$
$K_{eq1} \approx \exp\left(-24.389 + \frac{7059.726}{T}\right)$
$K_{eq2} \approx \exp\left(-4.672 + \frac{4773.26}{T}\right)$

Here, K_{eq1} and K_{eq2} are the equilibrium constants for the MS and RWGS reactions, respectively. The terms k_1 and k_2 denote the reaction rate constants, while K_a, K_b, and K_c are adsorption constants. The values of these constants are listed in Table 4.4:

Table 4.4: Parameters for calculating the adsorption and rate constants [50]

Parameter	Units	A	ΔH or B [kJ/kmol]
Adsorption constants (Van't Hoff equation):		$K = A \cdot e^{\Delta H/RT}$	
K_a	[–]	3453.38	–
K_b	[bar$^{-0.5}$]	0.499	17197
K_c	[bar^{-1}]	6.62×10^{-11}	124119
Rate constants:	$k = A \cdot e^{E/RT}$		
k_1	[mol/(kg·s·bar^2)]	1.07	36696
k_2	[mol/(kg·s·bar)]	1.22×10^{10}	−94765

The implementation of these kinetic expressions and parameters was carried out in AspenTech's software Aspen Plus, based on the methodology described in L.M.Al-Mallah (2017) [51] and X.Cui et al. (2022)[52]. Model validation was performed using experimental data from K.M.V.Bussche et al. (1996) [50], where the temperature profile along the reactor length was documented under specific operating conditions. Figure 4.7 illustrates the comparison between the simulation results and the experimental data.
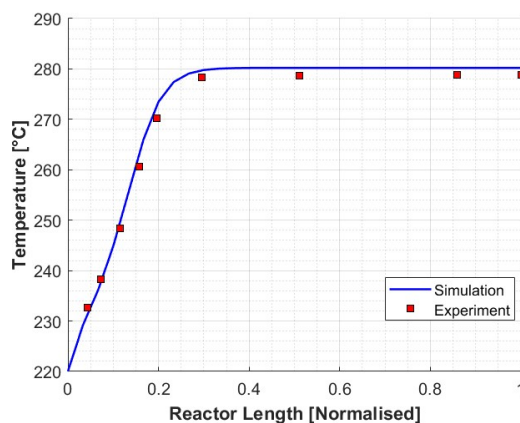
Figure 4.7: Comparison of temperature profiles along the reactor length between experimental data and model predictions [50]

As shown in Figure 4.7, the simulation closely follows the experimental data, demonstrating good agreement and confirming the accuracy and reliability of the developed kinetic model.

4.3.4 Reactor Design

The design and operation of the MS reactor are highly sensitive to both pressure and temperature due to the competing nature of the underlying chemical reactions. The primary reaction,CO_2 hydrogenation (Equation 4.45),is exothermic and involves a reduction in molar volume, while the RWGS reaction (Reaction 4.46) is endothermic and does not alter the number of gas-phase molecules. According to Le Chatelier's principle, high pressure and low temperature thermodynamically favour MeOH formation. However, these conditions must be balanced carefully in reactor design. Operating pressure directly influences both reaction equilibrium and equipment cost. In this work, the optimal pressure is determined through an economic assessment presented in a 5.1. Once pressure is established, it serves as a boundary condition for reactor sizing and thermal evaluation. Experimental studies and modelling efforts ([17, 18]) indicate that inlet temperatures below 463 K lead to significantly reduced CO_2 conversion. This is primarily attributed to poor catalyst utilisation at lower temperatures, particularly in fixed-bed reactor configurations. On the other hand, outlet temperatures exceeding 553 K result in diminished MeOH selectivity due to the increasing dominance of the RWGS reaction, along with accelerated catalyst deactivation. To ensure that the selected reactor inlet temperature enables optimal conversion without compromising long-term performance, a sensitivity analysis will be carried out in a subsequent chapter. This analysis is conducted only after the reactor pressure is fixed, as thermal behaviour depends on both thermodynamic and kinetic factors influenced by pressure.

A fixed-bed reactor configuration was selected based on the comparative analysis presented by Cui et al. (2020)[17], offering a balance between design simplicity, efficient conversion, and manageable capital costs. To support the mechanical design and ensure realistic pressure behaviour, the pressure drop across the packed bed is modelled using the Ergun equation, implemented directly in Aspen Plus.

4.4 Methanol Distillation

This section outlines the methodology used to design the MD system. The aim is to identify a column configuration that satisfies strict purity requirements while minimising total annual cost (TAC). The process is structured in sequential stages: starting from shortcut design using the Distillation Shortcut Model, Underwood-Wine-Gilliland (DSTWU) model, followed by detailed simulation and optimisation in Rigorous Algorithm Distillation Fractionation (RadFrac) column, and concluding with an economic evaluation. Only the design approach and methodology are presented here; detailed results and final configuration choices will be discussed in Subsection 5.3.2.

4.4.1 Design Objectives and Methodology

The primary design goal is to produce MeOH with a distillate purity of at least 99.7%, meeting specifications for fuel-grade e-MeOH applications [5]. Since the product stream from MS contains impurities and H_2O, it must be refined through distillation to ensure compliance with these standards. In parallel, the bottom product should contain H_2O with a purity above 99.9 wt% to reduce the burden on any downstream water treatment [52]. To meet these objectives while minimising capital and energy costs, the distillation system was designed following the methodology outlined in AspenTech's tutorials ([53, 54]). The NRTL (Non-Random Two-Liquid) property method was selected for both the DSTWU and RadFrac column simulations. This model was chosen due to its proven accuracy in representing non-ideal vapour–liquid equilibrium behaviour in strongly interacting polar systems, such as MeOH-H_2O mixtures, typical in e-MeOH production processes [5].

4.4.2 Shortcut Column Design - DSTWU

To initiate the design, the DSTWU model in Aspen Plus was used for preliminary analysis. This shortcut model provides quick estimates of the minimum number of theoretical stages and the minimum reflux ratio required to achieve target purities. While these estimates are not exact, they serve as a useful starting point for more detailed simulations. Following best practices in early-stage design, an initially high reflux ratio was used to simulate near-total reflux conditions. This allowed for estimation of the minimum number of stages required for feasible separation. Using this approach, a base case scenario was established where the top product was constrained to a MeOH purity of 99.7%. The resulting estimates for reflux ratio and stage count were then used to generate a sensitivity table showing how these two variables trade off against each other. This table forms the basis for selecting appropriate design points to be explored in the next phase using the RadFrac model. Additionally, it was observed that for different reflux ratios, the optimal feed stage (where the feed enters the distillation column) was consistently proposed to be 8 stages below the total number of theoretical stages. Therefore, this feed location was

fixed in all subsequent RadFrac simulations to maintain consistency and reflect the optimal configuration suggested by the shortcut analysis.

4.4.3 Detailed Column Design (RadFrac)

Configuration Adjustments

In transitioning to the RadFrac model, the system was modified to account for non-condensable gases (CO, CO_2, and H_2) that may enter the distillation unit as part of the upstream methanol synthesis output. A separation unit (SEP2) was inserted between the condenser and the reflux drum, as shown in Figure 4.8. This design improvement allows removal of these light gases before the liquid enters the reflux drum, thereby improving methanol purity in the final distillate.
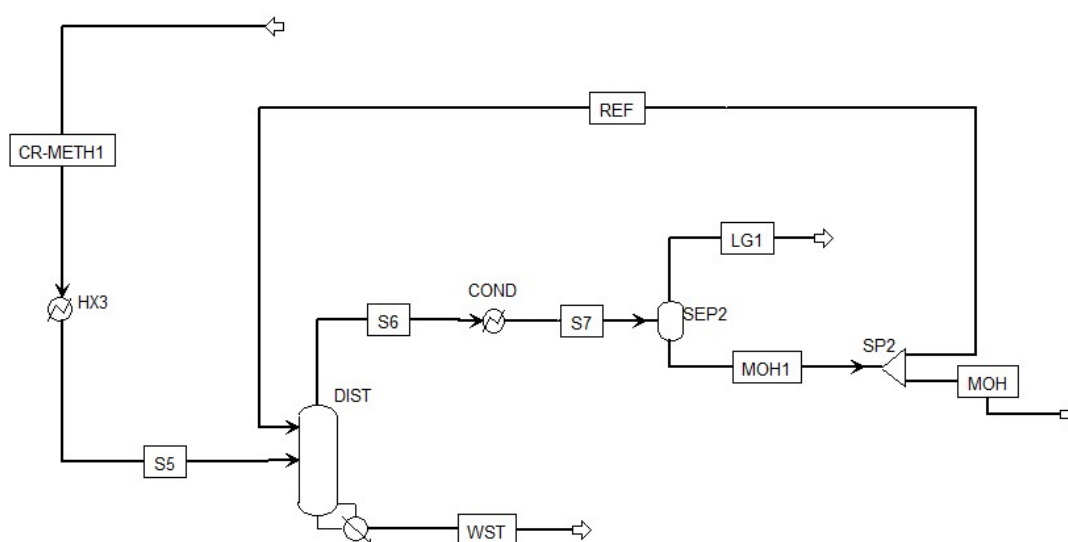
Figure 4.8: MD system configuration

RadFrac Optimisation Procedure

Once the system layout was finalised, RadFrac simulations were used to optimise the column. The optimisation strategy involved varying the number of equilibrium stages for a fixed reflux ratio and determining the minimum number of stages that would meet product specifications. Aspen Plus's model analysis tools enabled a systematic approach to this task. The reflux ratio range explored in RadFrac was based on results from the earlier DSTWU simulations. Since very high reflux ratios tend to offer diminishing returns, the optimisation began with a high value and was gradually decreased toward the minimum feasible reflux ratio. For each case, the number of stages and reboiler duty were optimised while maintaining target MeOH and water purities. This approach allowed for a comprehensive trade-off analysis between energy consumption and equipment size.

Reflux Ratio Sensitivity and Economic Trade-Off

It is expected that decreasing the reflux ratio will lead to an increase in the number of equilibrium stages, while reboiler duty decreases. Lower reflux ratios reduce internal column flow, thereby decreasing energy requirements, but at the same time demand more stages to achieve the same level of separation. This trade-off has a direct impact on capital cost, as taller columns with more trays are generally more expensive to construct and operate. To identify the most cost-effective configuration, several design points were evaluated across a range of reflux ratios. Each case was analysed based on the TAC, which includes both energy costs and capital amortisation. The optimal design is selected in the results chapter based on this economic criterion.

4.4.4   Economic Evaluation

Column Sizing and Configuration

To perform the cost analysis, Aspen Plus was used to calculate the physical dimensions of the distillation column for each design scenario. A sieve tray configuration was selected, and the software automatically determined the height and diameter based on internal vapour and liquid loads. Importantly, the column was divided into two sections: above and below the feed point. The upper section required a larger diameter due to increased vapour flow after feed entry, particularly if the feed includes hot or partially vaporised components. The lower section carried less vapour and more liquid, permitting a smaller diameter. This distinction ensures operational stability, minimises the risk of flooding and meets hydraulic requirements.

Cost Basis and Calculation

The TAC serves as the economic objective function and includes both capital and operating costs. Capital cost is annualised using a 3-year payback period, while energy costs are calculated based on utility requirements. Table 4.5 summarises all parameters and formulas used in the cost analysis.

<div align="center">

Table 4.5: Basis for economic optimisation [54]

</div>

Condenser	
Heat-transfer coefficient (U_{cond})	0.852 kW/(K·m²)
Differential temperature (ΔT)	50 K
Capital cost	$7296 \cdot A_{ex}^{0.65}$ (A_{ex} in m²)
Reboiler	
Heat-transfer coefficient (U_{reb})	0.568 kW/(K·m²)
Differential temperature (ΔT)	58.2 K
Capital cost	$7296 \cdot A_{ex}^{0.65}$ (A_{ex} in m²)
Heat Transfer Area	
Formula	$A_{ex} = \dfrac{Q_{\text{reb}}}{U_{\text{reb}} \cdot \Delta T}$ or $A_{ex} = \dfrac{Q_{\text{cond}}}{U_{\text{cond}} \cdot \Delta T}$
Column Vessel	
Capital cost	$17{,}640 \cdot D^{1.066} \cdot H^{0.802}$ (D and H in m)
Energy Cost	
Low-pressure steam (6 bar, 160°C)(C_{steam})	$7.78/GJ
Refrigeration	
Chilled water (5°C to 15°C)(C_{chill})	$4.43/GJ
Energy Cost Calculation	
Reboiler energy cost	$Q_{\text{reb}} \cdot t_{\text{op}} \cdot C_{\text{steam}}$
Condenser energy cost	$Q_{\text{cond}} \cdot t_{\text{op}} \cdot C_{\text{chill}}$
TAC Formula	$\text{TAC} = \dfrac{\text{capital cost}}{\text{payback period}} + \text{energy cost}$
Payback period	3 years

The outcome of this cost-based evaluation, which includes selected reflux ratio, column dimensions, energy demand, and total cost, will be presented and discussed in the Subsection 5.3.2.

4.5 Energy Efficiency of the MSD Process

The overall energy efficiency of the MSD process was evaluated using three parameters: MS efficiency (η_{MS}), MD efficiency (η_{MD}), and total MSD system efficiency (η_{MSD}). The corresponding equations are presented below, while the detailed power inputs and outputs are shown in the system energy balance diagram (refer to Figure 5.26).

The primary energy input to the MSD process is the H_2 produced by the electrolyser, which contributes the largest share of the input energy via its lower heating value (LHV). The main useful output is the MeOH product, also expressed in terms of its LHV. Additional energy exchanges include process HEXs, the recycle compressor, and various pumps. Notably, the purge stream (PUR), which contains a high fraction of H_2, is assumed to be combusted and used as a heat source for auxiliary systems. The reboiler duty is covered primarily by the heat recovered from HX2 and, if necessary, supplemented by external utilities. For simplification, the energy consumption related to cooling water circulation is not included in this analysis.

The energy efficiencies are calculated using the following expressions:

$$\eta_{\mathrm{MS}} = \frac{\dot{m}_{\mathrm{CR-METH}}LHV_{\mathrm{CR-METH}} + \dot{m}_{\mathrm{PUR}}LHV_{\mathrm{PUR}} - P_{\mathrm{HX1}}}{\dot{m}_{\mathrm{H2}}LHV_{\mathrm{H2}} + P_{\mathrm{HX2}} + P_{\mathrm{COMP}}} \tag{4.47}$$

$$\eta_{\mathrm{MD}} = \frac{\dot{m}_{\mathrm{MOH}}LHV_{\mathrm{MOH}}}{\dot{m}_{\mathrm{CR-METH}}LHV_{\mathrm{CR-METH}} + (P_{\mathrm{Reb}} + P_{\mathrm{HX3}}) + (P_{\mathrm{P1}} + P_{\mathrm{P2}})} \tag{4.48}$$

$$\eta_{\mathrm{MSD}} = \frac{\dot{m}_{\mathrm{MOH}}LHV_{\mathrm{MOH}} + \dot{m}_{\mathrm{PUR}}LHV_{\mathrm{PUR}}}{\dot{m}_{\mathrm{H2}}LHV_{\mathrm{H2}} + (P_{\mathrm{HX1}} + P_{\mathrm{HX3}} + P_{\mathrm{Reb}} + P_{\mathrm{HX2}}) + (P_{\mathrm{COMP}} + P_{\mathrm{P1}} + P_{\mathrm{P2}})} \tag{4.49}$$

Here, $\dot{m}$ represents molar flow rates (kmol/h), LHV is the lower heating value (kJ/kmol), and P refers to thermal duties or electrical power requirements (kW).

4.6 Dynamic Model of MSD

In the previous sections, the development of the steady-state model for the MeOH synthesis and distillation (MSD) system has been outlined. The steady-state model provides valuable insights into mass and energy balances, equipment sizing, and overall process feasibility under fixed operating conditions. However, industrial processes are inherently dynamic. Disturbances, load changes, and control actions occur frequently in day-to-day operations. To accurately represent and manage these variations, a dynamic model is essential. Before exploring the conversion process from a steady-state to a dynamic model, several assumptions must be stated:

- Heat transfer through the reactor walls has been neglected, implying no heat loss from the catalyst to the reactor shell or the environment.

- Heat transfer from all heaters to their surroundings has also been ignored for simplification.

4.6.1 Converting from Steady-State to Dynamic Operation

Unlike steady-state simulations, dynamic simulations require detailed information about equipment that influences time-dependent behaviour. This includes approximate sizing of separators, HEXs control valves, and more. The dynamic response of each unit depends on its size (volume or mass) in relation to flow rates and other fluxes. Therefore, sizing becomes a prerequisite for accurate dynamic modelling. Moreover, a complete dynamic simulation setup must incorporate the concept of plumbing: strategically installing pumps, compressors, and control valves to ensure proper material flow throughout the system. This work uses a pressure-driven simulation approach, where pressures and pressure drops guide material flow from high to low pressure regions. These principles and methodologies align with guidelines from W.L.Luyben (2002)[55]. Dynamic model of MSD is built using Aspen Tech's software Aspen Dynamics.

4.6.2 Sizing Equipment

To facilitate dynamic simulation, equipment volumes must be roughly estimated. The following subsections outline the approach used for different equipment types.

Separators

Separators are vertical vessels designed to disengage vapour and liquid phases, typically featuring both liquid and vapour outlets. Industry heuristics recommend at least five minutes of liquid holdup. Assuming a vertical cylindrical vessel with the liquid interface at 50% height, the total separator volume is calculated as:

- Determine steady-state liquid flow entering the separator in m^3/min.

- Multiply by 5 minutes for holdup volume.

- Multiply by 2 to account for half-full operation (liquid and vapour phases) to obtain full volume of separator.

The last step is to define the L/D ratio to obtain final dimensions. With an aspect ratio of two, the relationship between volume and diameter is:

$$\text{Volume} = \frac{\pi}{4}D^2 L = \frac{\pi}{4}D^2(2D) = \frac{\pi}{2}D^3 \qquad (4.50)$$

Surge Volumes

Tanks and reboilers serve as surge volumes wherever liquid pumping is involved. These vessels buffer disturbances and help maintain stable liquid levels. The common heuristic provides for 5 minutes of liquid holdup at half-full capacity, based on total inlet flow. The sizing procedure mirrors that of separators.

Heat Exchangers

The dynamics of heaters and coolers (and column reboilers and condensers) are usually assumed to be fast compared to the composition and flow dynamics. In Aspen Dynamics, these units are assumed to be instantaneous [55]. However, for HEX inlet and outlet volume will be specified in this project, and are defined using:

$$\text{volume} = \frac{(\text{residence time}) \times (\text{steady state volumetric flow rate})}{2}$$

The residence time is based on the phase and the side of the heat exchanger (shell or tube), as shown below:

Phase	Shell Side	Tube Side
Liquid/Mixed	15 minutes	5 minutes
Vapour	3 seconds	1 second

Table 4.6: Residence time guidelines for dynamic HEX modelling.

4.6.3 Plumbing

Correct configuration of piping and equipment placement is crucial. Materials flow from high to low pressure, necessitating appropriately positioned pumps, compressors, and valves. Therefore, three main plumbing laws needs to be followed:

- Place valves in liquid lines downstream of centrifugal pumps.

- Use only one control valve in each liquid-filled stream or branch (Note that if the flow is split into multiple streams (a tee in the line or a "splitter" in the simulation), there can only be one valve in each line)

- Never throttle the discharge of a compressor.

4.6.4 Control Valve Sizing

Once the locations of all control valves have been established by following the laws of plumping, their size must be specified. This boils down to setting their percent opening and their pressure drop under design conditions. A trade-off exists:

- Smaller pressure drops reduce pump/compressor energy consumption.

- Larger pressure drops improve controllability and rangeability.

4.6.5 Installing Controllers and Tuning

This section discusses the setup and tuning of PI controllers (see 4.2.1), as supported in W.L.Luyben (2002)[55].

Flow Controllers

Flow controllers are straightforward to tune due to fast dynamics. The time constants for moving the control values are small (several seconds) which results that controller can be tuned with small integral contribution K_i.

Level Controllers

Most level controllers use proportional-only action, which means that there will be some offset, but it avoids sluggish response and instability from overreaction. Reverse action is commonly used, and a typical gain setting is $K_p = 2$, unless the distillation column base level is controlled by reboiler heat input and bottoms flow is manipulated for temperature or composition, in which case a higher gain may be necessary.

Pressure Controllers

Pressure controllers, often set to direct action, are also quick to tune. Pressure controller settings in very fast loops such as compressor controls have much smaller integral times.

Inclusion of Lags and Temperature Controllers

Temperature control is more complex due to slower dynamics. First-order lags (e.g., 1-minute delay) are introduced to reflect real-life behaviour. Reverse controller action is typical. One important example of implementation of temperature controller in the distillation column is the choice of the stage where temperature will be controlled. In this thesis, the control stage is above the feed stage.

Relay-Feedback Testing

Relay-feedback testing is a simple and powerful way to tune controllers without requiring full knowledge of process dynamics. This method is used to oscillate the process around the setpoint, allowing calculation of:

- Ultimate gain K_u

- Ultimate period P_u

Tuning parameters are then derived via:
Ziegler-Nichols (aggressive, for flow/pressure control):

$$K_p = \frac{K_u}{2.2}, \qquad\qquad K_i = \frac{P_u}{1.2} \qquad\qquad (4.51)$$

Tyreus-Luyben (conservative, for level/temperature control):

$$K_p = \frac{K_u}{3.2}, \qquad\qquad K_i = 2.2P_u \qquad\qquad (4.52)$$

Aspen Dynamics includes Auto-Tune (ATV), which applies relay-feedback testing automatically. Users can select the preferred tuning method based on the controller type.

4.7 LSTM Surrogate Model Development for an MSD Process

Once the dynamic simulation model of the MSD system is established in Aspen Dynamics, it is possible to construct a data-driven surrogate model using machine learning techniques. Among the most suitable approaches for capturing temporal behaviour in dynamic processes is the long lhort-term memory (LSTM) neural network. This section outlines the development methodology for building an LSTM-based surrogate model that can predict key performance indicators (KPIs) of the MSD system based on variations in H_2 feed rates.

4.7.1 Methodology Overview

LSTM networks are a type of artificial intelligence (AI) designed to learn patterns from time-based data, making them ideal for creating fast surrogate models of complex chemical process simulations. Instead of relying on slow, detailed physics-based simulations (like MSD models) that can take hours to run, LSTM surrogate models learn from the input-output data of these complex simulations to quickly predict the same important outcomes like product quality, yield, and energy consumption. Once trained, these AI models can replicate the behaviour of the original detailed simulation in seconds, since they act as a black-box. Building an effective LSTM surrogate involves four main steps:

- Data preparation

- LSTM model configuration

- Model training and validation

- Deployment and use

This approach has proven successful across various chemical processes, offering a practical balance between prediction accuracy and computational speed.

4.7.2 Data Preparation

Dynamic Simulation Data Collection

The input to the surrogate model is the H_2 flow rate entering the MS unit. To create a diverse and representative dataset, dynamic simulations were conducted in Aspen Dynamics by applying a wide range of step changes of H_2 feed variations. This approach ensures that the entire spectrum of operating scenarios of the MSD process is covered.

Sequence Formation

Because the LSTM model processes sequential data, it is necessary to structure the input–output data as time-series sequences. Each sample consists of a sequence of H_2 feed rates over a defined time window, along with the corresponding outputs (KPIs). This approach allows the model to capture time-dependent relationships and delayed system responses.

Normalisation

To ensure stable model training and to prevent disproportionate influence of variables with large numerical scales (e.g., compressor power vs. flow rates), both input and output features are normalised. Common method include scaling values to the range [0, 1].

Data Splitting

The dataset is divided chronologically into training, validation, and testing sets. The training set is used to fit the model, the validation set is used for hyperparameter tuning and to prevent overfitting, and the testing set is reserved for final evaluation. Chronological splitting ensures that future data is not used to predict past events.

4.7.3 LSTM Model Configuration

LSTM networks are specifically designed to capture and update information across long sequences by using an internal memory structure. In this study, the LSTM surrogate model takes as input a sequence of H_2 flow rates from previous time steps (for example, the last 10 or 20 values) and predicts the corresponding KPIs at the next time step.

Each LSTM unit, or "cell", processes data corresponding to a single time step. These cells contain a memory component known as the cell state, as well as three gates: the input gate, the forget gate, and the output gate. These gates work together to manage the flow of information through the network. The forget gate determines which information should be discarded from the cell state. The input gate controls which new information should be written into the cell. Finally, the output gate decides what information should be passed forward to the next time step or to the following layer.

When using a sequence length of 20, for instance, the model forms 20 LSTM cells aligned along the time axis. These cells together make up a single LSTM layer. After the final time step is processed, the output from the LSTM layer is passed to a dense (fully connected) layer. This layer maps the learned representation to the predicted KPIs. The number of neurons in this dense layer corresponds to the number of KPIs being predicted (e.g.,

methanol flow rate, reboiler duty, compressor power, etc.). The more detailed explanation of LSTM configuration and operation can be found in Van Houdt et al.(2020)[56].

Hyperparameters

The model's architecture is defined by several key hyperparameters, which influence its performance and training behaviour

- Sequence length: Specifies how many past time steps are used as input to predict the next output. This should correspond to the physical time lag between input changes and system response.

- Number of LSTM layers: Defines how many LSTM layers are stacked, allowing the model to learn more complex temporal patterns.

- Number of units per layer: Indicates how many memory cells (neurons) are present in each LSTM layer, which affects the model's capacity.

- Number of epochs: Refers to how many complete passes through the training dataset are performed.

Initial values for these hyperparameters were selected based on existing literature and were later tuned using validation results to improve both prediction accuracy and training efficiency. A more detailed explanation of LSTM internals, including mathematical formulas and block diagrams, can be found in [57].

4.7.4 Model Training and Validation

As already mentioned, the LSTM surrogate model is trained by feeding it with sequences of hydrogen feed data and their associated KPIs. During this process, the model learns to approximate the nonlinear relationship between the input sequence and the target KPIs. To monitor the model's learning progress, performance is visualised by comparing predicted versus actual values on the validation set. A good model should capture both steady-state and transient dynamics of the system. Validation ensures that the trained LSTM surrogate model generalises well to unseen data. These scenarios may include new patterns of hydrogen feed variations. The model performance was evaluated by the mean absolute error (MAE) and coefficient of determination (R^2), which are given by the following equations [57]:

$$\text{MAE} = \frac{1}{N} \sum_{i=1}^{N} \left| \hat{Y}_i - Y_i \right| \tag{4.53}$$

$$R^2 = 1 - \frac{\sum_{i=1}^{N} \left(\hat{Y}_i - Y_i \right)^2}{\sum_{i=1}^{N} \left(\overline{Y} - Y_i \right)^2} \tag{4.54}$$

where N represents the number of data points, and $\hat{Y}_i$ and Y_i are the predicted and real target output values, respectively.

4.7.5 Deployment and Use

Once validated, the LSTM surrogate model becomes a useful tool for real-time prediction of process performance. It can evaluate KPIs such as MeOH production rate or system efficiency in milliseconds, avoiding time-consuming simulations in Aspen Dynamics. In practical applications, the surrogate model may be implemented in:

- Real-time monitoring systems that track process conditions and provide fast predictions of desired outputs.

- Optimisation frameworks, where system load or operation can be adjusted in response to electricity price fluctuations or renewable energy availability.

Further integration and optimisation based on this surrogate model will be explored in 5.3.4.

4.8 CAPEX

4.8.1 Methodology Overview

The capital expenditure (CAPEX) assessment in this study is conducted to support two key decisions in the design of the e-MeOH production system: determining the optimal operating pressure and selecting the appropriate type of electrolyser. These choices significantly influence the design and cost of various process units, particularly the MS section, the H_2 compression system, and the electrolyser itself.

This report compares MS at two operating pressures: 35 bar and 70 bar. The 35 bar case is included as it represents the upper pressure limit typically tolerated by AEL. The 70 bar case is considered based on findings from Teles et al. (2024) [58], which report that, for reactors of comparable scale to the one modelled here, optimal operating pressures range between 67 and 76 bar.

Configuration Scenarios

To evaluate these design trade-offs, 5 distinct process configurations were developed, each representing a different combination of operating pressures and electrolyser technology as it can be seen in Figure 4.9. The underlying principle is to explore how system pressure and electrolyser type affect overall investment cost, considering that higher pressure typically enhances methanol synthesis performance by increasing conversion and reducing reactor and recycle compressor sizes.

The first configuration (Case 1) is based on using an AEL operating at 35 bar, which is its maximum allowable pressure. In this case, the entire system, including the MeOH synthesis section, operates at 35 bar. This eliminates the need for a H_2 compressor between the electrolyser and the synthesis loop, resulting in simpler integration and lower compression costs. High pressure of the electrolyser is achieved with a H_2O pump, which is notably less expensive (both regarding CAPEX and OPEX). In the second configuration (Case 2), the AEL still operates at 35 bar, but a H_2 compressor is added to boost the pressure to 70 bar before entering the MS unit. This case is designed to assess the trade-off between reduced reactor and recycle compressor costs (due to improved conversion at higher pressure) and the added cost of H_2 compression. The third, fourth, and fifth case explore the
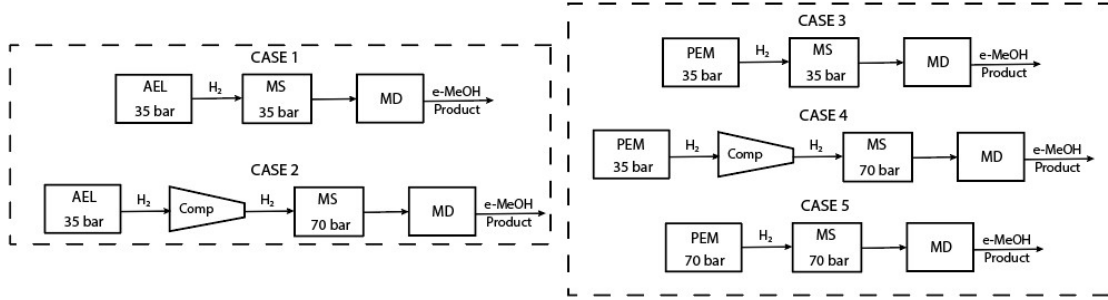
Figure 4.9: Schematic overview of the five configuration cases evaluated for CAPEX analysis.

use of PEMELs. The third case considers a case when the entire system operating at 35 bar. In the fourth case, the PEMEL operates at 35 bar while the MS loop is pressurised to 70 bar using a H_2 compressor. Finally, the fifth configuration assumes that both the PEMEL and the MS unit operate at 70 bar, eliminating the need for additional H_2 compression.

As established in Section 1.2, PEMELs are technically capable of operating at pressures up to 200 bar. However, such high pressures are not typical in industrial practice. According to a 2022 technology brief by the Electric Power Research Institute (EPRI) [59], PEMELs commonly operate at pressures up to 70 bar. This is further supported by a 2019 demonstration from the National Renewable Energy Laboratory (NREL), which showed that a commercial-scale PEMEL system can operate at pressures up to 70 bar [60].

This structured comparison of five cases allows for a clear evaluation of CAPEX impacts under realistic pressure and integration scenarios. Intermediate pressures were not considered.

4.8.2   Electrolyser Capital Cost Estimation

To estimate the CAPEX of AEL and PEMEL in this work, the methodology developed by Reksten et al. (2022) [38] was adopted. This techno-economic model accounts for both plant size and technological development as key cost drivers. The authors compiled a comprehensive cost database from detailed bottom-up estimates and direct manufacturer quotes. The included costs cover the electrolyser stack, balance of plant (e.g., water purification, gas separators, pumps, valves), and required power electronics. Installation costs, civil works, and compressors are excluded. Electrolyser cost is modelled using a modified power law:

$$C_{elec} = k_0 \left(k_0 + \frac{k}{Q} Q^\alpha \right) \left(\frac{V}{V_0} \right)^\beta \cdot 0.92 \qquad (4.55)$$

where C_{elec} is the projected CAPEX (€/kW), Q is the plant capacity (kW), V and V_0 are the installation and reference years. Parameters α and β are scaling and learning exponents, while k_0 and k are fitting constants. The factor 0.92 is conversion from dollars to euros. Table 4.7 summarises the fitted values for AEL and PEMEL systems.

Table 4.7: Projection parameters for CAPEX calculation of AEL and PEMEL systems [**reksten2022**].

Parameter	AEL	PEMEL
α	0.649	0.622
β	-27.33	-158.9
k_0	301.04	585.85
k	11603	9458.2
V_0	2020	2020
SE (standard error)	547	510

This formulation offers a validated and scalable foundation for projecting electrolyser capital costs until 2030. As presented in Section 5.1, the total electrolyser cost accounts for two complete units, reflecting the assumption that stack replacement will be required once during the 20-year project lifetime for which the cost estimation is conducted.

In addition to the electrolyser cost, two water pumps within the electrolyser system are considered as the components with the most significant impact on CAPEX after the electrolyser itself.
A large circulation pump handles the main H_2O circulation loop within the electrolyser system. It is responsible for compensating pressure losses throughout the system and maintaining the continuous circulation of large volumes of H_2O required for proper electrolyser operation. It operates within the closed circulation loop and handles flow rates needed for adequate heat removal and membrane hydration. A small feed water pump is positioned outside the main circulation loop and serves to introduce fresh H_2O into the system. While its flow rate is significantly lower than the circulation pump, it must perform the demanding task of pressurising the incoming H_2O from atmospheric pressure up to the system's operating pressure (35 or 70 bar). This pump ensures that H_2O can be continuously supplied to replace the water consumed in the electrolysis process.

4.8.3 Cost Estimation of Other Equipment

The capital cost of equipment such as reactors, compressors, and pumps was estimated using the standard capacity scaling correlation described in R.Smith (2005) [61]:

$$C_c = C_B \left(\frac{Q_c}{Q_B} \right)^M f_M f_P f_T \tag{4.56}$$

In this expression, C_B and Q_B represent the base cost and base capacity, respectively. Q_c is the actual design capacity of the equipment, and M is the cost exponent. The correction factors f_M, f_P, and f_T account for the effects of material of construction, operating pressure, and operating temperature, respectively.

Table 4.8: Simplified equipment base data for CAPEX estimation [61]

Equipment	Material	Capacity	Q_B	C_B (€)	M
Reactor (Pressure vessel)	SS (high grade)	Mass (t)	6	8.66×10^4	0.82
Compressor	SS (high grade)	Power (kW)	250	8.66×10^4	0.46
Pump	SS (high grade)	Power (kW)	1	1.73×10^3	0.35

Table 4.8 provides the selected parameters used for pressure vessels (representing the reactor), compressors, and pumps.

Table 4.9: Correction factors used for material, pressure, and temperature [61]

Factor type	Condition	Factor value
Material (f_M)	SS (high grade)	3.4
Pressure (f_P)	0.5-7 bar	1
Pressure (f_P)	50 bar	1.5
Pressure (f_P)	100 bar	1.9
Temperature (f_T)	0-100°C	1
Temperature (f_T)	300°C	1.6
Temperature (f_T)	500°C	2.1

The corresponding correction factors for materials, pressure, and temperature are summarised in Table 4.9. It should be noted that for pressure and temperature values not explicitly listed in the table, the correction factors were obtained by linear interpolation between the nearest available data points.

Only the CAPEX of major equipment components is included in this analysis. The cost of heaters and separators is not evaluated, as their influence is negligible when comparing the impact of different operating pressures and electrolyser types. These components are assumed to contribute similarly across all configurations. The CAPEX of the distillation column is calculated separately, as discussed in Section 4.4, since it is assumed to remain constant across all cases. This assumption is based on the fact that the crude methanol stream exiting the MS unit, in terms of both flow rate and composition, is considered unaffected by changes in the system's operating pressure.

4.8.4 Reactor Cost Estimation

The sizing of the MS reactor was conducted for both operating pressure cases (35 bar and 70 bar), using a consistent methodology to ensure comparability between configurations. For each case, the Gas Hourly Space Velocity (GHSV) was fixed at 10,000 h^{-1}, which defines the volumetric gas flow rate at standard conditions per unit of catalyst volume. This ensures that the amount of catalyst scales consistently with the process flow rate. To maintain acceptable flow conditions and avoid excessive pressure drop, the superficial gas velocity at the reactor inlet was constrained to remain below 2 m/s. An initial reactor geometry with a length-to-diameter (L/D) ratio of 5 was assumed. If this resulted in an inlet velocity above the 2 m/s limit, the L/D ratio was reduced iteratively until the constraint was satisfied. The final reactor dimensions were then used to estimate the capital cost of the reactor using the capacity-based scaling approach. The equipment cost was calculated

based on the reactor mass and the base data provided in Table 4.8, with correction factors applied for material, pressure, and temperature conditions. In addition to the vessel itself, the cost of the catalyst inside the reactor was also included. The commercial catalyst used is $Cu/Zn/Al_2O_3$, with a market price of €20000 per tonne, based on supplier data [62]. The catalyst mass was calculated based on the internal reactor volume and the bulk density typical for fixed-bed catalysts. It was assumed that the catalyst needs to be replaced every five years. As the operational lifetime of the plant is assumed to be 20 years, catalyst replacement was considered to occur four times during this period. The total cost of these replacements was therefore included in the overall capital cost of the reactor system.

4.9 Optimisation of Flexible Operation

After the PEMEL system and MSD systems were developed independently in the previous sections, this part of the project focuses on integrating these subsystems to determine the most cost-effective operational strategy for the PtMeOH plant under dynamic electricity pricing conditions. This section presents the development of a mathematical optimisation model that determines the optimal hourly operational schedule by considering variable electricity prices and meeting methanol production targets whilst minimising total operational costs. The optimisation model was implemented and solved using MathWorks software MATLAB.

4.9.1 General Setup Information

The optimisation model is formulated using discrete time periods and operational states to accurately represent the dynamic behaviour of the integrated PtMeOH system. The time step is an hour ($\mathcal{T}$), which aligns with typical electricity market pricing intervals enables capturing the operational dynamics of both the electrolyser and MSD systems.

The electrolyser operational flexibility is modelled through seven discrete load levels ($\mathcal{L}$), ranging from 40% to 100% of rated capacity in 10% increments. The lower operational boundary at 40% load is determined by the integrated system constraints, particularly the downstream MSD system. The load level fractions (λ_l) are used to calculate the corresponding power consumption and production rates.

The model considers seven distinct operating states ($\mathcal{S}$): running operation at various load levels, standby (SB) and shutdown (SD) modes for periods when operation is not economical, cold and hot startup procedures, and transition states to switch the system to standby and shutdown modes (4.2).

- $\mathcal{T}$: Set of time periods (hours), $t \in \{1, 2, \ldots, T\}$

- $\mathcal{L}$: Set of electrolyser load levels, $l \in \{1, 2, \ldots, 7\}$ corresponding to different current loads $\{40\%, 50\%, 60\%, 70\%, 80\%, 90\%, 100\%\}$

- λ_l: Load level fractions, $\lambda_l \in \{0.4, 0.5, 0.6, 0.7, 0.8, 0.9, 1.0\}$

- $\mathcal{S}$: Operating states, $s \in \{\text{Run}, \text{SB}, \text{SD}, \text{ColdStart}, \text{HotStart}, \text{SBTrans}, \text{SDTrans}\}$

Hydrogen Buffer Tank Conceptualisation

A H_2 buffer tank is conceptually positioned between the PEMEL and the MSD systems to accommodate the different dynamic response characteristics of these subsystems (Figure 5.26). The buffer tank is a temporary storage tank that serves two critical operational functions.

First, it provides the necessary H_2 supply to enable gradual MSD system ramp-down during electrolyser shutdown periods, allowing the electrolyser to stop operation immediately when electricity prices become too expensive while the MeOH reactor continues controlled gradual shutdown procedures using stored H_2 (part *c* of Figure 4.11). Once the electrolyser is turned on and begins production, the initial H_2 output is directed toward the buffer tank to compensate for this loss of capacity, so it is ready for another ramp-down procedure (part *c* of Figure 4.10).

Second, the tank compensates for the mismatch between electrolyser load changes, which can occur instantaneously, and MSD system load adjustments, which require gradual ramp-up and ramp-down periods. During electrolyser load increases, excess H_2 is temporarily stored until the MSD system completes its ramp-up to accommodate for higher H_2 flow rates (part *f* of Figure 4.10). Conversely, during load decreases, the stored H_2 supplements the reduced electrolyser output whilst the MSD system gradually reduces its H_2 consumption (part *a* of Figure 4.11). Although the buffer tank volume is estimated based on these operational requirements, it is not explicitly modelled as a separate optimisation variable. Instead, its effects are implicitly incorporated into the cost calculations and MeOH production constraints, with the simplifying assumption that the symmetric ramp-up and ramp-down rates ensure sufficient H_2 storage capacity for all operational scenarios. Hydrogen boil-off losses and tank-specific energy consumption are not considered in this analysis.

4.9.2 Objective Function

The objective function (Eq. 4.57) aims to minimise the total operational cost of the integrated PtMeOH plant over the given time period. The cost function includes all major operational expenditures (OPEX) including electricity consumption during normal operation, costs associated with maintaining the system in standby or shutdown states, and the economic penalties of startup procedures. Additionally, the model accounts for the MSD system's operational costs during standby and shutdown transition periods, when the methanol synthesis unit requires specific power consumption profiles whilst switching between operational modes.

$$\min Z = \sum_{t=1}^{T} \left[\sum_{l=1}^{7} c_{t,l} x_{t,l} + c_t^{\text{SB}} y_t^{\text{SB}} + c_t^{\text{SD}} y_t^{\text{SD}} + c_t^{\text{cold}} z_t^{\text{cold}} + c_t^{\text{hot}} z_t^{\text{hot}} + c_t^{\text{SB-trans}} w_t^{\text{SB}} + c_t^{\text{SD-trans}} w_t^{\text{SD}} \right]$$

(4.57)

4.9.3 Binary Decision Variables

The system's operational behaviour is represented with binary decision variables that indicate the active operational state at each time step (Table 4.10). These variables act as switches to include only the relevant parameters for each specific hour. The variables

include steady-state operational modes (running, standby, shutdown) and dynamic transition states to capture all aspects of system operation. The running state variables ($x_{t,l}$) define the specific load level when the electrolyser is operational (index l refers to load levels). The standby (y_t^{SB}) and shutdown (y_t^{SD}) variables represent non-productive states that may be economically advantageous during periods of high electricity prices. The startup variables differentiate between cold (z_t^{cold}) and hot (z_t^{hot}) starts based on the system's thermal condition, whilst the transition variables (w_t^{SB} and w_t^{SD}) account for switching the MSD system between standby and shutdown modes.

Table 4.10: Variable Definitions

Binary variables definition	
$x_{t,l} \in \{0,1\}$	Electrolyser running at load level l
$y_t^{SB} \in \{0,1\}$	System in standby mode
$y_t^{SD} \in \{0,1\}$	System in shutdown mode
$z_t^{cold} \in \{0,1\}$	Cold start initiated
$z_t^{hot} \in \{0,1\}$	Hot start initiated
$w_t^{SB} \in \{0,1\}$	Transition to standby mode
$w_t^{SD} \in \{0,1\}$	Transition to shutdown mode

4.9.4 Hourly Costs

Table 4.11 shows cost expressions for each system's mode. Running mode costs combine both electrolyser and MSD system power consumption, while standby and shutdown modes account for reduced power requirements needed to maintain system readiness. These visual representations below in the Figures 4.10 and 4.11 demonstrate the power consumption patterns during transitional modes.

Table 4.11: Cost equations

Cost equations	
$c_{t,l} = P_t^{el} \cdot (E_l^{con} + E_l^{MSD})$	Running mode costs
$c_t^{SB} = P_t^{el} \cdot (E^{con\text{-}SB} + E^{MSD\text{-}SB})$	Standby mode cost
$c_t^{SD} = P_t^{el} \cdot E^{MSD\text{-}SB}$	Shutdown mode cost
$c_t^{cold} = C^{cold} + P_t^{el} \cdot E_t^{cold\text{-}total}$	Cold start cost
$c_t^{hot} = C^{hot} + P_t^{el} \cdot E_t^{hot\text{-}total}$	Hot start cost
$c_t^{SB\text{-}trans} = P_t^{el} \cdot E_t^{SB\text{-}trans}$	Standby transition cost
$c_t^{SD\text{-}trans} = P_t^{el} \cdot E_t^{SD\text{-}trans}$	Shutdown transition cost

The expressions $E_t^{cold-total}$ and $E_t^{hot-total}$ from Table 4.11 represent the complex energy consumption in time step when cold and hot start occurs (4.58). Here, E^{MSD} represents

the sum of all power sinks in MSD system.

$$
\begin{aligned}
E_t^{cold-total} = {} & E_1^{con}(1 - D^{cold}) \\
& + E^{MSD-SB}(D^{cold} + D^{tank}) \\
& + E^{MSD-ramp}D^{MSD-heating} \\
& + E^{MSD}(1 - D^{cold} - D^{tank} - D^{MSD-heating})
\end{aligned}
\qquad
\begin{aligned}
E_t^{hot-total} = {} & E_1^{con}(1 - D^{hot}) \\
& + E^{MSD-SB}(D^{hot} + D^{tank}) \\
& + E^{MSD-ramp}D^{MSD-heating} \\
& + E^{MSD}(1 - D^{hot} - D^{tank} - D^{MSD-heating})
\end{aligned}
$$

$$(4.58)$$

These startup processes involve multiple sequential operations that are visually illustrated in Figure 4.10, showing the temporal changes in H_2 and MeOH flows. The startup sequence consists of several phases: period *a* represents the previous hour when the electrolyser was off and the MSD system remained in standby. During the startup hour *t*, the electrolyser begins heating (period *b*). Once heated, the current load increases and the produced H_2 initially compensates for H_2 consumed during the previous standby or shutdown transition (period *c*). After refilling the H_2 buffer tank, H_2 flows to the MSD system where MeOH production ramps up (period *d*). The final phase (period *e*) involves the MeOH reactor heating to operating temperature whilst production stabilises.

The MeOH flow ramp-up duration and reactor heating time are not directly calculated, but taken from the S.Mbatha et al. (2024) [20], where comprehensive study of MSD system's flexibility is done. Therefore, fixed values for flow ramp-up ($D^{MSD-ramp}$) and heating duration ($D^{MSD-heating}$) during the transition states are implemented in the optimisation model:

$$D^{MSD-ramp} = 6min \qquad (4.59)$$

$$D^{MSD-heating} = 39min \qquad (4.60)$$

Note that MeOH reactor heating initiates through exothermic reactions as soon as methanol production begins.
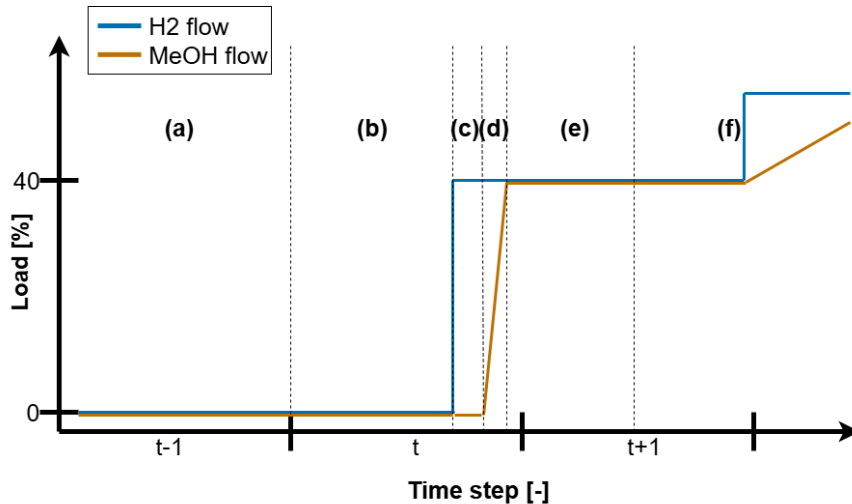

Figure 4.10: Temporal evolution of H_2 and MeOH flows during cold/hot startup procedure showing sequential operational phases

The expressions $E_t^{SB-trans}$ and $E_t^{SD-trans}$ from Table 4.11 represent the energy consumption

in time step when standby and shutdown transition occurs.

$$E_t^{\text{SB-trans}} = E^{\text{con-SB}} \cdot (1 - D^{\text{MSD-ramp}}) \qquad E_t^{\text{SD-trans}} = E^{\text{MSD-ramp}} \cdot D^{\text{SB}}$$
$$+ E^{\text{MSD-ramp}} \cdot D^{\text{MSD-ramp}} \qquad\qquad\qquad + E^{\text{MSD-SB}} \cdot (1 - D^{\text{MSD-cooling}}) \qquad (4.61)$$
$$+ E^{\text{MSD-SB}} \cdot (1 - D^{\text{MSD-cooling}})$$

These startup processes involve multiple sequential operations that are visually illustrated in Figure 4.11, showing the temporal changes in H_2 and MeOH flows. These transition sequences consist of several phases: phases *a* and *b* presents the operational mode. In the time step *t* in which the transition occurs, flow of H_2 drops almost instantly, while MeOH production drops gradually, with the same ramp rate that was defined for the flow ramp-up ($D^{MSD-ramp}$, based on S.Mbatha et al. (2024) [20]). After period *c* ends, there is no production of MeOH anymore, but MeOH reactor is still cooling down to its standby temperature, which is presented in period *d*. During this period, there is no energy consumption required to maintain the temperature of the MeOH reactor, but after the reactor reaches the standby temperature, an additional heater is turned on to maintain the constant temperature. The duration required for the reactor to cool down to standby temperature is taken from S.Mbatha et al. (2024) [20] ($D^{MSD-cooling}$):

$$D^{MSD-cooling} = 90min \qquad (4.62)$$
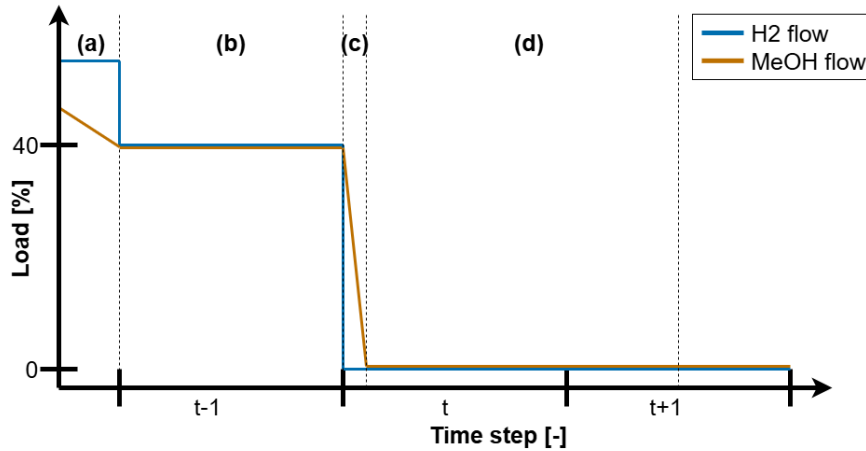
Figure 4.11: Temporal evolution of H_2 and MeOH flows during standby/shutdown transition showing sequential operational phases

Next, PEMEL require direct current (DC), while most electrical grids supply alternating current (AC). Because of it, an AC/DC converter must be used in the system, and it is considered here that 5% of the energy is lost due to conversion. Therefore, electrolyser power consumption (E_l^{elec}) including efficiency losses is used in the calculation of energy consumption, and it is referred to as E_l^{con}.

Variables not explicitly mentioned here are defined in the parameter list below.

- $E^{\text{con-standby}}$: Standby power consumption, including losses [MW]

- E_l^{MSD} : MSD power [MW]

- $E^{\text{MSD-SB}}$: MSD standby power [MW]

- $E^{\text{MSD-ramp}}$: MSD ramp-up/down power [MW]

- D^{cold} : Cold start duration [h]

- D^{hot} : Hot start duration [h]

- D^{tank} : Tank filling duration [h]

- P_t^{el} : Electricity price at time t [€/MWh]

- C^{cold} : Cold start cost [€]

- C^{hot} : Hot start cost [€]

- C^{CO_2} : CO$_2$ credit price [€/ton]

- C^{heat} : Excess heat value [€/MW]

4.9.5 Constraints

Having defined the objective function, the optimisation model requires constraints to define the feasible solution space. These constraints should ensure that only realistic operational scenarios are considered. The constraint set enforces operational logic, defines what system state transitions are permitted, implements required limitations, and ensures production targets are met. Together with the previously defined objective function and decision variables, these constraints establish a complete optimisation problem.

Single Mode Operation

This constraint ensures that exactly one operational mode is active during each time step. The sum of all binary decision variables equals unity, preventing simultaneous activation of multiple operational states and guaranteeing that the system operates in only one mode at any given hour.

$$\sum_{l=1}^{7} x_{t,l} + y_t^{\text{SB}} + y_t^{\text{SD}} + z_t^{\text{cold}} + z_t^{\text{hot}} + w_t^{\text{SB}} + w_t^{\text{SD}} = 1 \quad \forall t \in \mathcal{T} \tag{4.63}$$

Initial State

The optimisation requires a defined starting condition to establish the system's initial operational state. The system is set to begin operation at 40% electrolyser load, representing a typical minimum stable operating point that ensures a feasible starting configuration for the optimisation algorithm. After this step, the system can go to whatever mode is found to be the optimal one for the following hour.

$$x_{1,1} = 1 \tag{4.64}$$

State Transition Constraints

The set of constraints listed below in Table 4.12 presents the permitted and forbidden transitions between operational states of the electrolyser system in the optimisation model. The mandatory transitions ensure that when a transition mode (e.g., cold start, hot start, standby transition, or shutdown transition) is activated, the system correctly progresses to the corresponding next operational state. Conversely, the forbidden direct transitions explicitly restrict unrealistic switches between states, such as transitioning directly from shutdown to running, or from standby to hot start. These logical constraints enforce a physically and operationally consistent mode transition logic within the optimisation problem.

Table 4.12: Transition constraints

Transition constraints		
Mandatory transitions		
$z_{t-1}^{\text{cold}} = x_{t,1}$	$\forall t \geq 2$	After cold start, 40% operation follows
$z_{t-1}^{\text{hot}} = x_{t,1}$	$\forall t \geq 2$	After hot start, 40% operation follows
$w_{t-1}^{\text{SB}} = y_t^{\text{SB}}$	$\forall t \geq 2$	After standby transition, standby mode follows
$w_{t-1}^{\text{SD}} = y_t^{\text{SD}}$	$\forall t \geq 2$	After shutdown transition, shutdown mode follows
$w_{t+1}^{\text{SB}} = x_{t,1}$	$\forall t \in \{2, \ldots, T-1\}$	Standby transition only from 40% load
$w_{t+1}^{\text{SD}} = x_{t,1}$	$\forall t \in \{2, \ldots, T-1\}$	Shutdown transition only from 40% load
Forbidden transitions		
$x_{t-1,l} + z_t^{\text{cold}} \leq 1$	$\forall t \geq 2, \forall l \in \mathcal{L}$	No cold start from running state
$x_{t-1,l} + z_t^{\text{hot}} \leq 1$	$\forall t \geq 2, \forall l \in \mathcal{L}$	No hot start from running state
$x_{t-1,l} + y_t^{\text{SD}} \leq 1$	$\forall t \geq 2, \forall l \in \mathcal{L}$	No direct shutdown from running state
$x_{t-1,l} + y_t^{\text{SB}} \leq 1$	$\forall t \geq 2, \forall l \in \mathcal{L}$	No direct standby from running state
$y_{t-1}^{\text{SB}} + x_{t,l} \leq 1$	$\forall t \geq 2, \forall l \in \mathcal{L}$	No direct running from standby
$y_{t-1}^{\text{SB}} + y_t^{\text{SD}} \leq 1$	$\forall t \geq 2$	No direct shutdown from standby
$y_{t-1}^{\text{SB}} + w_t^{\text{SB}} \leq 1$	$\forall t \geq 2$	No standby transition from standby
$y_{t-1}^{\text{SB}} + w_t^{\text{SD}} \leq 1$	$\forall t \geq 2$	No shutdown transition from standby
$y_{t-1}^{\text{SB}} + z_t^{\text{cold}} \leq 1$	$\forall t \geq 2$	No cold start from standby
$y_{t-1}^{\text{SD}} + x_{t,l} \leq 1$	$\forall t \geq 2, \forall l \in \mathcal{L}$	No direct running from shutdown
$y_{t-1}^{\text{SD}} + y_t^{\text{SB}} \leq 1$	$\forall t \geq 2$	No direct standby from shutdown
$y_{t-1}^{\text{SD}} + z_t^{\text{hot}} \leq 1$	$\forall t \geq 2$	No hot start from shutdown
$y_{t-1}^{\text{SD}} + w_t^{\text{SB}} \leq 1$	$\forall t \geq 2$	No standby transition from shutdown
$y_{t-1}^{\text{SD}} + w_t^{\text{SD}} \leq 1$	$\forall t \geq 2$	No shutdown transition from shutdown

Minimum Operating Time Constraints

These constraints reflect the physical and technical limitations of the system, preventing excessive switching between operational states that could cause equipment stress or operational inefficiencies. The exact values that such systems must have in real-life scenarios are not available in the literature. Instead, the values defined here are chosen to simplify the model by ensuring that after a certain operational change occurs, both PEMEL and MSD models reach quasi-steady-state conditions before transitioning to another operational state. The minimum operating times provide sufficient duration for the system to stabilise after each transition, preventing unrealistic rapid cycling between states that would complicate the modelling framework and potentially lead to infeasible operational scenarios.

$t^{\text{min-run}} = 3h$**:** Minimum continuous running time

$t^{\text{min-SB}} = 2h$**:** Minimum standby time

$t^{\text{min-SD}} = 12h$**:** Minimum shutdown time

The mathematical formulations in Table 4.13 ensure that when a transition to any of these states occurs, the system remains in the corresponding operational mode for the specified minimum duration.

Table 4.13: Minimum time constraints

Minimum time constraints		
Minimum running time		
$z_t^{\text{cold}} \leq x_{t+k,l}$ $\quad \forall t \in \{1, \ldots, T - t^{\text{min-run}}\}, \forall k \in \{1, \ldots, t^{\text{min-run}}\}, \forall l$		After cold start
$z_t^{\text{hot}} \leq x_{t+k,l}$ $\quad \forall t \in \{1, \ldots, T - t^{\text{min-run}}\}, \forall k \in \{1, \ldots, t^{\text{min-run}}\}, \forall l$		After hot start
Minimum standby time		
$w_t^{\text{SB}} \leq y_{t+k}^{\text{SB}}$ $\quad \forall t \in \{1, \ldots, T - t^{\text{min-SB}}\}, \forall k \in \{1, \ldots, t^{\text{min-SB}}\}$		Minimum standby time
Minimum shutdown time		
$w_t^{\text{SD}} \leq y_{t+k}^{\text{SD}}$ $\quad \forall t \in \{1, \ldots, T - t^{\text{min-SD}}\}, \forall k \in \{1, \ldots, t^{\text{min-SD}}\}$		Minimum shutdown time

Methanol Production Constraint

This constraint ensures that the total MeOH production over the planning horizon meets the specified target while accounting for the varying production rates during different operational phases (see Figures 4.10 and 4.11).
Rather than integrating the full Aspen Dynamics MSD model or its surrogate directly into the optimisation framework, the model employs a matrix-based approach that captures steady-state MeOH production rates and average production rates during transitions between different load levels. This matrix representation significantly reduces computational complexity while maintaining accuracy in production calculations, and is described in detail later in this section.
The production calculation accounts for steady-state operation with transitions between different load levels, as well as reduced production during startup and transition periods. During cold and hot starts, MeOH production follows the same temporal phases as

described in the Hourly costs subsection (see 4.9.4), where initial periods involve system stabilisation with limited production, followed by gradual ramp-up to full capacity. The transition states also result in reduced MeOH output due to the ramp-down of the MSD system.

The Equation 4.65 captures mentioned production variations by applying different production rates for each operational mode, ensuring that the optimisation considers both the cost implications and production demand when determining the optimal operational schedule. Variables not mentioned already in text are defined in the list below the equations.

$$M_{TOTAL}^{MeOH} = \sum_{t=1}^{T} \left[\sum_{l=1}^{7} \sum_{l'=1}^{7} M_{l',l} x_{t-1,l'} x_{t,l} + M_t^{cold} z_t^{cold} + M_t^{hot} z_t^{hot} + M_t^{trans}(w_t^{SB} + w_t^{SD}) \right] \geq M_{TARGET}^{MeOH}$$

(4.65)

$$M_t^{cold} = M^{start}(D^{MSD-ramp}/2 + D^{MSD-heating} - D^{MSD-ramp})$$
$$+ M_1^{load}(1 - D^{cold} - D^{tank} - D^{MSD-heating})$$
$$M_t^{hot} = M^{start}(D^{MSD-ramp}/2 + D^{MSD-heating} - D^{MSD-ramp})$$
$$+ M_1^{load}(1 - D^{cold} - D^{tank} - D^{MSD-heating})$$
$$M_t^{trans} = \frac{M_1^{load}}{2} D^{MSD-ramp}$$

- M_{TOTAL}^{MeOH}: Total MeOH production over planning horizon [kg]

- $M_{l',l}$ = MeOH production rate transitioning from load l' to l [kg/h]

- M_t^{cold}: MeOH production during cold start [kg]

- M_t^{hot}: MeOH production during hot start [kg]

- M_t^{trans}: MeOH production during transition mode [kg]

- M^{start}: MeOH production rate during cold/hot start [kg/min]

- M_1^{load}: MeOH production rate at 40% load [kg/h]

4.9.6 Complete Economic Objective

The complete economic objective extends the basic OPEX function to include additional economic factors that impact the overall profitability of the PtMeOH plant. This total cost function (Z_{TOTAL}) accounts for CO_2 consumption costs, which represent a significant expense in MS, and revenue from useful excess heat that can be utilised for district heating (Eq. 4.66). These economic values are taken as fixed values from M.S.Taslimi et al. (2024) [10].

The conversion factors relating MeOH production to CO_2 consumption and excess heat generation are based on results from Aspen Dynamics simulations. The inclusion of these terms provides a more accurate representation of the true economic performance, although some factors remain unaccounted for (e.g., revenue from O_2 sales or expenses for H_2O purification).

$$Z_{TOTAL} = Z + 1.416 M_{TOTAL}^{MeOH} C^{CO_2} - 0.0009 M_{TOTAL}^{MeOH} C^{heat}$$

(4.66)

The variables in the equation above represent the following:

- 1.416 = CO_2 consumption factor [kg CO_2/kg MeOH]

- $C^{CO_2} = 55.3$ €/tonne (CO_2 credit price)

- 0.0009 = Excess heat generation factor [MW/kg MeOH]

- $C^{heat} = 30.2$ €/MW (Excess heat value)

4.9.7 Practical Solutions

To make the model less computationally demanding while maintaining high accuracy in the optimisation results, several practical solutions were implemented. These approaches reduce the mathematical complexity of the model without notably reducing the precision of the calculations.

Regression Model for Electrolyser

Rather than implementing the complete Simulink electrolyser model directly within the MATLAB optimisation code, a regression-based approach was adopted to represent electrolyser electricity consumption. Since the electricity demand of the PEMEL represents the major operational expense of the integrated plant, it has the most significant impact on total costs and therefore requires a precise approach.
The regression model was developed by calculating energy consumption values across the full range of operational current loads, followed by quadratic regression analysis between these data points. The coefficient of determination (R-squared) was employed to evaluate the goodness of fit (Equation 4.54) The resulting quadratic regression equation for electrolyser energy consumption takes the form:

$$E_l^{elec} = a \cdot \lambda_l^2 + b \cdot \lambda_l + c \tag{4.67}$$

where a, b, c are the regression coefficients. This approach enables the optimisation algorithm to evaluate different operational scenarios without sacrificing the accuracy needed for reliable economic assessment of the electrolyser's performance.

Matrix Representation of MSD Subsystem

Rather than implementing the computationally demanding surrogate model of the MSD system directly into the optimisation framework, a simplified matrix-based approach was developed. This method is based on results obtained from Aspen Dynamics simulations, where changes in MeOH production rates were systematically observed when H_2 input flows were varied.
The matrix development involved calculating average hourly MeOH production rates for every possible load transition scenario, including both constant production cases where the load remains unchanged and dynamic cases where load transitions occur between time steps. The resulting production matrix is structured such that each row represents the electrolyser load from the previous hour (l') and each column represents the load in the current observed hour (l). This configuration enables the model to account for transient production variations caused by H_2 flow changes in the system.

The H$_2$ load changes considered during matrix construction were directly based on current load variations from the Simulink electrolyser model, ensuring that MeOH production calculations remain directly connected to the actual current load changes experienced by the electrolyser. This approach captures the dynamic coupling between electrolyser operation and MeOH synthesis performance whilst maintaining computational efficiency.
The complete matrix is presented in Chapter 5. Additionally, the accuracy of this matrix-based approach is validated through direct comparison with the full surrogate model, to confirm that the simplified method maintains high precision while achieving significant computational advantages.

MATLAB Solver

The developed optimisation model is formulated as a mixed-integer linear programming (MILP) problem, which is suitable for systems that involve both binary decision-making and linear relationships. In this case, binary variables are used to represent discrete operational modes (e.g., load levels, standby, shutdown), while the objective function and all constraints remain linear.
The model was implemented and solved using MATLAB R2023a's `intlinprog` solver, which is designed to handle MILP problems. It uses branch-and-bound techniques with linear relaxations to efficiently explore feasible solutions. This solver converges to near-optimal solution within practical time limits.

Chapter 5

Results

This chapter presents the main results of the study, starting with a comparison of capital expenditure (CAPEX) for five different system configurations. The PEM electrolyser (PEMEL) is then analysed through steady-state and dynamic modelling, covering model validation, efficiency trends, control strategies, and thermal performance. Next, the methanol synthesis and distillation (MSD) processes are evaluated, including key design parameters and dynamic behaviour of the integrated system. The chapter finishes with a case study, developed in collaboration with another student, in which the dynamic operation of the full power-to-methanol (PtMeOH) system is explored. The goal of the case study is to determine an optimal operational strategy of the plant over the course of a year, based on variable electricity prices and the system's flexibility.

5.1 CAPEX Results

The results of the CAPEX comparison for all five configurations are presented in Table 5.1. The analysis was performed assuming a 20-year project lifetime. Accordingly, both PEM and alkaline electrolysers (AEL) were assumed to be replaced twice, as previously described in Section 4.8.

Table 5.1: CAPEX Breakdown for Different Cases

Category	Item	CASE 1	CASE 2	CASE 3	CASE 4	CASE 5
Electrolyser	Type of electrolyser	AEL	AEL	PEM	PEM	PEM
	Rated Power [MW]	50	50	50	50	50
	Operating pressure [bar]	35	35	35	35	70
	Cost [€/kW]	482.57	482.57	462.24	462.24	462.24
	Total cost [k€]	**48257**	**48257**	**46224**	**46224**	**46224**
H_2O Pump	Power duty [kW]	12	12	12	12	25
	Cost [k€]	**75**	**75**	**75**	**75**	**140**
H_2O Pump - Big	Power duty [kW]	47	47	47	47	47
	Cost [k€]	**158**	**158**	**158**	**158**	**196**
H_2 Compressor	Power duty [kW]	0	364	0	364	0
	Cost [k€]	**0**	**447**	**0**	**447**	**0**
Reactor	L/D ratio	4	5	4	5	5
	Length [m]	8.15	8.35	8.15	8.35	8.35
	Thickness [m]	0.013	0.022	0.013	0.022	0.022
	Pressure [bar]	35	70	35	70	70
	Cost [k€]	**2881**	**2502**	**2881**	**2502**	**2502**
Recycle Compressor	Power duty [kW]	1268	334	1268	334	334
	Cost [k€]	**616**	**423**	**616**	**423**	**423**
Distillation Column	Cost [k€]	**549**	**549**	**549**	**549**	**549**
Total Cost [k€]		**52536**	**52411**	**50504**	**50378**	**50035**

Among all configurations, Case 5, which features a PEMEL operating at 70 bar, exhibits the lowest total CAPEX. This result is a direct outcome of effective pressure alignment throughout the system, coupled with the efficient utilisation of higher operating pressure. Since the PEMEL operates at the same pressure as the MSD unit (70 bar), there is no need for intermediate H_2 compression. This simplifies the system and reduces equipment count and energy demand. Additionally, the higher system pressure improves MeOH conversion, allowing for a smaller reactor volume and consequently lower reactor cost. Improved conversion also reduces the amount of unreacted H_2 and CO_2, which in turn decreases the recycle load and the required power of the recycle compressor. Furthermore, this result confirms the technical and economic advantage of PEMEL over AEL ones in pressure-integrated systems (Chapter 3).
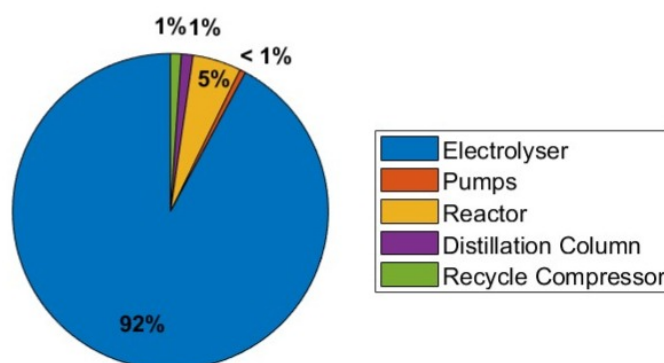

Figure 5.1: Distribution of CAPEX by equipment category for Case 5

A visual breakdown of the CAPEX distribution for Case 5 is shown in Figure 5.1. It clearly highlights that the electrolyser accounts for nearly 90% of the total investment. While this figure shows slightly higher values than reported in literature, such as the 85% electrolyser contribution found by [63], the difference can be explained by the use of an adiabatic fixed-bed reactor in the present study. This reactor type is one of the most cost-effective options for methanol synthesis (MS). If a water-cooled or gas-cooled reactor were used instead, its higher cost would reduce the relative share of the electrolyser in the total CAPEX.

5.2 PEM Electrolyser

This section describes the modelling, validation, and performance analysis of the PEMEL system. It begins by presenting the key design parameters and justifying their selection. A steady-state model is then developed and validated using reference data. Then follows the analysis of the overpotentials, parametric study and efficiency results.
The dynamic model is introduced to capture the transient behaviour of the PEMEL under varying operating conditions. This section examines the system's response over time, with a focus on control strategies and thermal management. Simulations with changing current inputs reveal the evolution of key variables. Finally, transition states are explored, along with different temperature ramp rates, to evaluate the system's startup performance.

5.2.1 Electrolyser Parameters Summary

In Section 4.1, constants used in the steady-state part of the model, taken from V. Liso et al. (2018) [40], were presented. The remaining system parameters required for calculations across all model modules are presented below in Table 5.2. The electrolyser model chosen as a reference is Siemens' PEMEL called Silyzer 300, which has a rated power of 17.5 MW. In this study, one Silyzer 300 unit is referred to as a single module. To meet the system's rated capacity of 50 MW, three modules are considered here.

Since many of the detailed technical parameters for the Silyzer 300 are not publicly available from the manufacturer, most values were obtained from M. Pfennig et al. (2025) [44]. In that work, some parameters were sourced from existing literature, while others were calculated. The operating temperature was set to 338 K. This value was selected because temperatures above 338 K lead to heat exchanger (HEX) dimensions that deviate significantly from design recommendations, such as those provided by Saari (2005) [45]. This problem can be solved by adding additional oil cooling mechanism, but to avoid the need for this, the temperature was limited to this value. Later in this section, it is shown that the effect this choice has on the system's efficiency is almost negligible.

The H_2O feed rate into the electrolyser was estimated based on the stoichiometric H_2O requirement for H_2 production, scaled by a factor of 65 (see 4.2). This ensures sufficient membrane hydration and provides adequate coolant capacity to remove the heat generated within the cell. While a portion of the heat is transferred through the membrane or released to the atmosphere, the remaining heat must be absorbed by the incoming H_2O.

HEX parameters were defined based on the total heat that needs to be removed from the system and the H_2O flow rate. Finally, it should be noted that the nominal values presented in this chapter correspond to the case where the electrolyser operates at 50 MW of power input, and this case is further in the report referred to as the 100% load case.

Table 5.2: Parameters of the electrolyser model

Description	Parameter	Value	Unit	Source
Rated power of electrolyser	P_{rated}	50	MW	–
Referent electrolyser model	–	Sylizer 300 (Siemens)	–	[44]
Number of cells	N	25	–	[44]
Thickness of MEA	δ_{mem}	175×10^{-4}	cm	[40]
Total area of MEA	A	6000	cm^2	[44]
Number of stacks	N_{stacks}	24	–	[44]
Number of modules	N_{module}	3	–	[44]
H$_2$O flow	$\dot{N}_{\text{H}_2\text{O}}$	500	m^3/h	–
Nominal current density	i	2.14	A/cm^2	calculated
Nominal cell voltage	V	2.16	V	calculated
Efficiency at nominal parameters	$\varepsilon_{\Delta H}$	67.5	%	calculated
Pressure anode	P_{anode}	70	bar	5.1
Pressure cathode	P_{cathode}	70	bar	5.1
Operating temperature	T	338	K	5.2.2
Atmosphere temperature	T_{atm}	298	K	–
Refrigerant temperature	$T_{\text{refrigerant}}$	293	K	4.2.1
Stack heat capacity	C_{stack}	717	kJ/K	[44]
Total lumped heat capacity	C_{tot}	52618	kJ/K	calculated
Stack thermal resistance	R_{th}	1/67	K/W	[44]
Heat transfer coefficient	U	1500	W/m^{2}K	[45]
Area of heat exchanger	A_{ex}	700	m^2	[45]
Nominal H$_2$ production	$\dot{m}_{\text{H}_2}$	869	kg/h	calculated

5.2.2 Electrolyser Model Validation and Results

Steady-State Part Of The Model

Four modules of the electrolyser model were built based on the work of V. Liso et al. (2018) [40], making it a reasonable and consistent choice to validate the model using the experimental results provided in the same paper. The results of this validation are shown in Figure 5.2. The constant parameters used for the validation are the same as those defined in Section 4.1, while the operating conditions of the electrolyser were adjusted to match the experimental setup, specifically $T = 333\,\text{K}$, $P_{\text{anode}} = P_{\text{cathode}} = 1\,\text{atm}$, and $A_{\text{cell}} = 2.89\,\text{cm}^2$. The close agreement between the experimental and simulated results on the $V-i$ curve confirms the accuracy of the steady-state model. The mean absolute error (MAE) of the simulation compared to the experimental data is calculated to be 0.89% (Eq. 4.53). After validating the steady-state part of the model, a brief sensitivity analysis was conducted to assess the influence of changes in electrolyser pressure and temperature on cell voltage. Since cell voltage directly impacts the overall system efficiency (see 4.28), it is important to understand how operating conditions affect performance. Figure 5.3 *a* shows the cell voltage across a pressure range of 1–70 bar. This range was selected because it reflects typical PEMEL operating conditions, as discussed in Section 4.8. As shown in the figure, decreasing the pressure reduces cell voltage and therefore increases efficiency. However, higher operating pressures minimise or eliminate the need for a H$_2$ compressor, so operating the electrolyser at elevated pressures is considered beneficial in the broader system context.
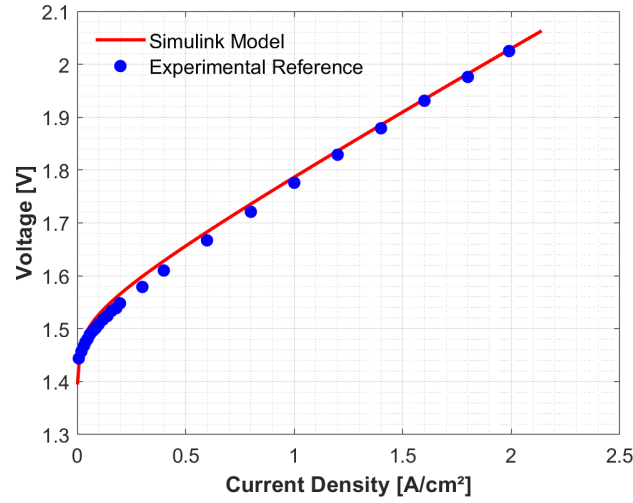
Figure 5.2: Comparison of the simulated steady-state polarisation curve with experimental data from V. Liso et al. (2018) [40]

Figure 5.3 *b* presents the influence of varying operating temperatures on cell voltage. It is evident that temperature has a significantly smaller effect on performance, particularly at current densities of 1 A/cm² and above. Consequently, the decision to limit the operating temperature to 338 K, as previously noted in this section, is reasonable and does not introduce major side effects.
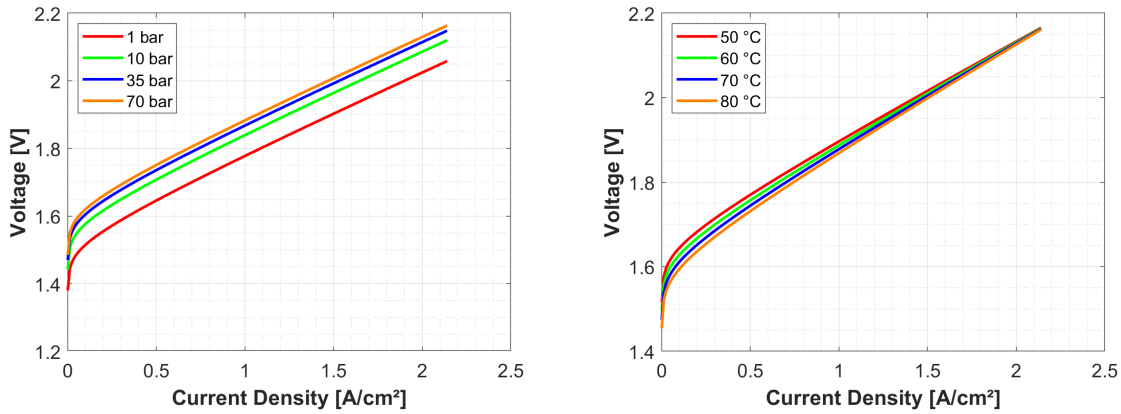
Figure 5.3: Sensitivity of cell voltage to pressure (left) and temperature (right) variations in the steady-state electrolyser model

To further analyse the behaviour of the electrolyser model, the individual contributions of various voltage losses are examined at two operating points: 40% load ($i = 0.856 \, \text{A/cm}^2$) and 100% load ($i = 2.14 \, \text{A/cm}^2$). The results, shown in Figure 5.4, illustrate how different overpotentials contribute to the total cell voltage. At higher current density, the ohmic loss increases significantly, becoming the dominant loss component (similar results are shown in A.Awasthi et al. (2011)[43]). In contrast, the activation loss shows only a slight increase, maintaining a relatively stable percentage of the total loss. Since ohmic overpotential is related to the resistance to the transport of H^+ ions through the system, this behaviour

suggests that improving membrane conductivity could significantly benefit system performance at high current densities by reducing ohmic losses and thereby increasing the system's efficiency.
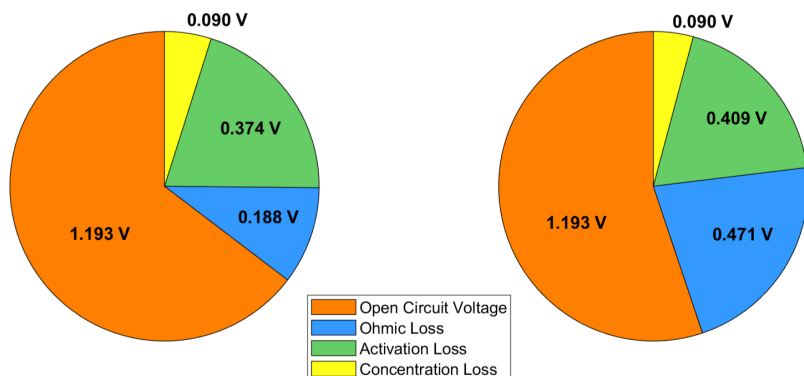

Figure 5.4: Breakdown of voltage overpotentials at 40% load (left) and 100% load (right)

Figure 5.5 illustrates the variation of first-law efficiency with current density for both the current model and the reference case. Efficiency peaks at moderate current densities and declines at higher loads due to increasing overpotentials (particularly ohmic loss) which raise the cell voltage and energy input. At very low current densities (around 0.2 A/cm²), efficiency also drops sharply, mainly due to parasitic losses becoming more dominant relative to hydrogen production (more heat is generated related to H_2 production). These trends are crucial for optimising the PtMeOH system. If efficiency were constant, operating the electrolyser only at full load would be optimal. However, since efficiency varies with load, the optimisation model adjusts current input dynamically to balance H_2 output with electricity cost. This justifies the use of a variable-load strategy, discussed in detail later in this chapter.

In the reference case (1 bar, 353 K[40]), the first-law efficiency (4.26) exceeds 100% at very low current densities (around 0.1 A/cm^2). This is because the electrical input is minimal, while the reaction still requires a fixed enthalpy (ΔH_{reac}^0). The remaining energy is supplied as heat absorbed from the surroundings, allowing the cell to operate partly endothermically. This effect is only possible at low pressure and elevated temperatures. By contrast, our model operates at 70 bar and 338 K, where higher pressure increases the Nernst potential (4.22), raising the required cell voltage and electrical input (4.26). Here, the electrical work exceeds the reaction enthalpy (ΔH_{reac}^0), so the cell releases rather than absorbs heat. As a result, the process is exothermic, and efficiency remains below 100%.

At nominal load (2.14 A/cm²), the difference in efficiency between our case and the reference is approximately 5%, further highlighting the sensitivity of system performance to operating conditions.
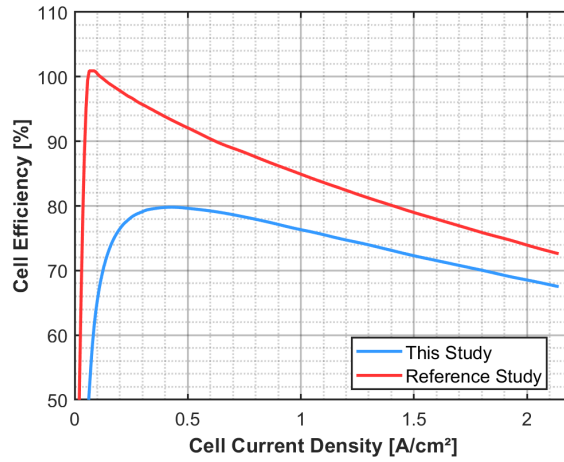
Figure 5.5: [40]

Dynamic State Part Of The Model

To ensure safe and stable operation of the electrolyser under dynamic conditions, the integration of an actively regulated cooling system is essential. During nominal operation, the electrolyser generates approximately 15.79 MW of heat, which must be effectively dissipated to prevent excessive temperature rise. Given the system's total lumped heat capacity of 52618 kJ/K, the temperature would increase rapidly if this heat were not properly managed, especially considering that only a portion is removed by species flow and ambient losses. As illustrated in Figure 5.6, without cooling, the stack temperature exceeds the reference limit of 338 K in less than three minutes. In contrast, with a PI-controlled cooling system, the temperature is stabilised around the desired setpoint shortly after heat-up. This demonstrates that the cooling system, along with its control, is a needed for enabling dynamic operation and maintaining thermal stability under varying load conditions.
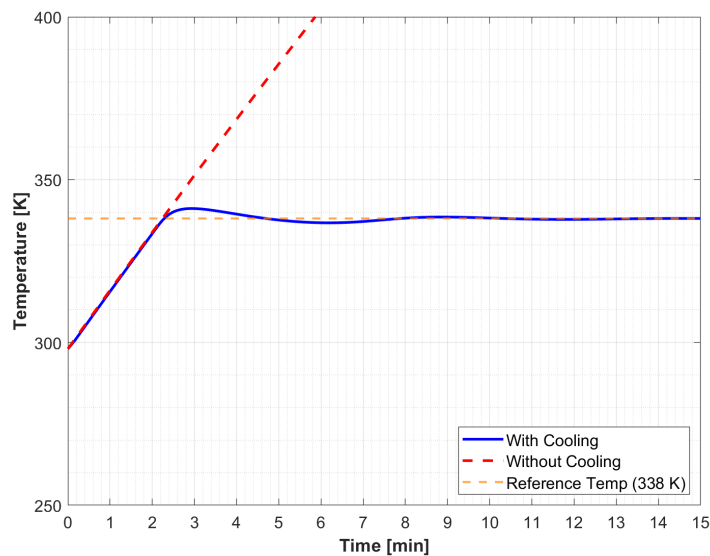

Figure 5.6: Comparison of the heating of a PEMEL with and without included cooling system

As it was explained in the Section 4.2 the pressure changes are negligible in this system, even though in reality there are some pressure variations.

To evaluate the impact of the anti-windup mechanism described in Section 4.2, its effect on the thermal control system is shown in Figure 5.7. The figure compares system behaviour with and without anti-windup integrated into the PI controller, which regulates refrigerant mass flow to remove excess heat. Without anti-windup (*a* and *b*), significant overshoot in both temperature and refrigerant flow occurs, resulting in poor control performance.
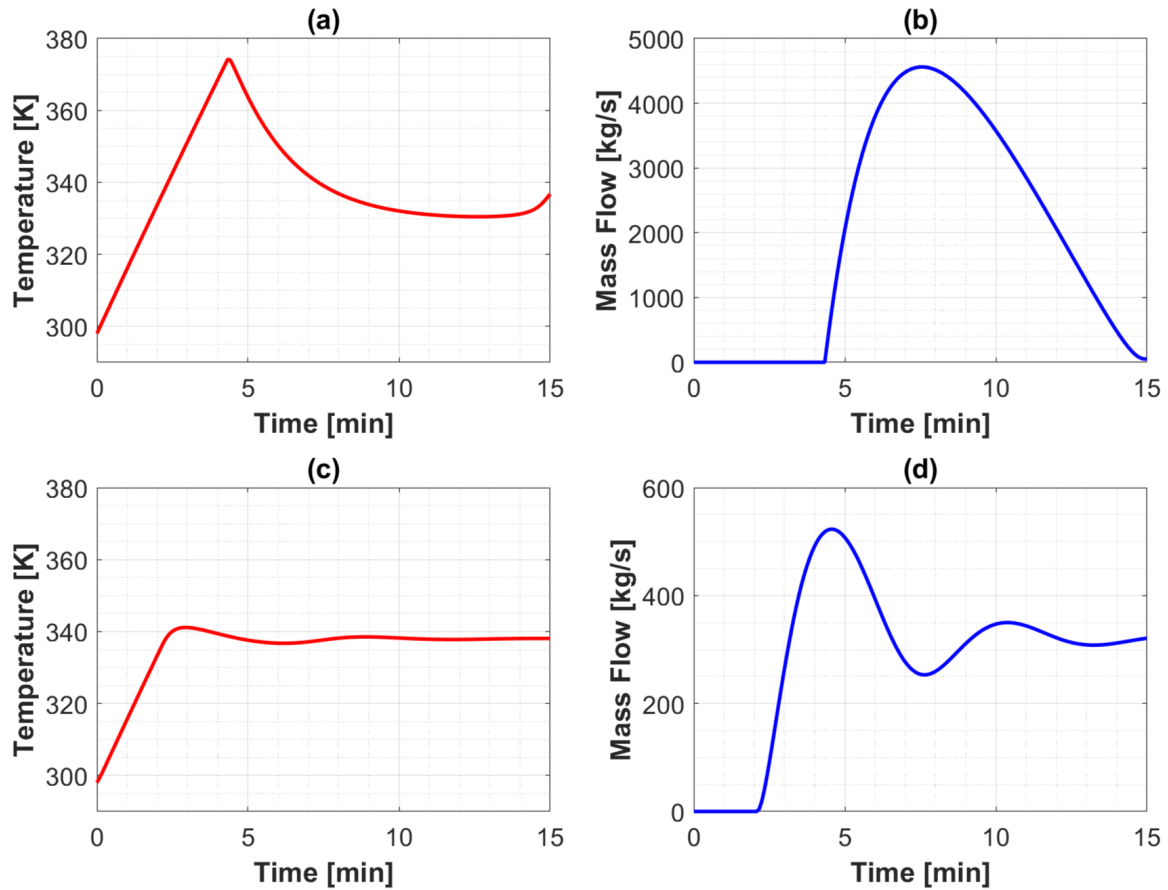

Figure 5.7: Comparison of system response with and without anti-windup: Stack temperature without anti-windup (a), Refrigerant mass flow without anti-windup (b), Stack temperature with anti-windup (c), Refrigerant mass flow with anti-windup (d)

With anti-windup (*c* and *d*), the system responds more smoothly, maintaining temperature near the reference point and keeping mass flow within realistic bounds. This highlights the importance of anti-windup for stable and effective thermal regulation during dynamic operation.

To confirm the effectiveness of the implemented PI controller with anti-windup mechanism, Figure 5.8 shows how the control error is minimising over time. The error initially rises as the system reacts to the temperature difference, but it quickly stabilises and converges toward zero. This demonstrates that the controller is able to regulate the cooling demand effectively, adjusting the refrigerant flow rate to remove the generated heat and maintain the desired stack temperature.
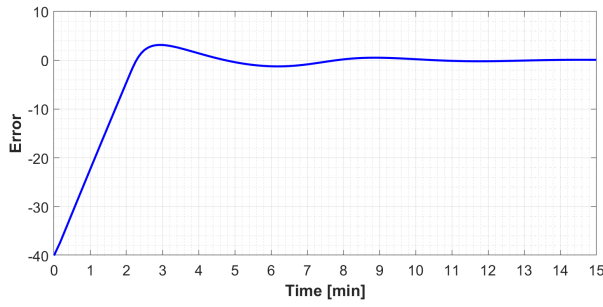
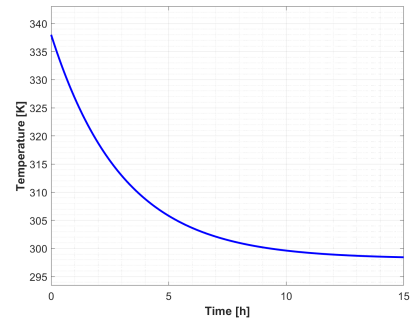**Figure 5.8:** Control error of the PI controller over time.

Figure 5.9: Cooldown profile of the electrolyser temperature after shutdown.

Figure 5.9 presents the passive cooldown behaviour of the electrolyser following a system shutdown. The temperature gradually decreases toward ambient levels over around 12 hours, reflecting realistic thermal dynamics based on the system's heat capacity and heat loss. This response is consistent with observed behaviour in other high-power systems [44] and confirms that the model accurately captures the physical characteristics of the system's thermal inertia and dissipation.

The graphs in Figure 5.10 demonstrate the system's dynamic response to step changes in operating current load. The upper plot shows current density transitions in intervals of one hour, simulating changes from 40% to 90%, then down to 50%, and finally to 60% load. The bottom plot captures the corresponding cell voltage response, which adapts almost instantaneously to each change in current density. This instant voltage response reflects the fast electrochemical dynamics of the PEMEL, consistent with findings from Gorgun (2006) [64], who similarly observed instantaneously voltage transients in response to current changes.
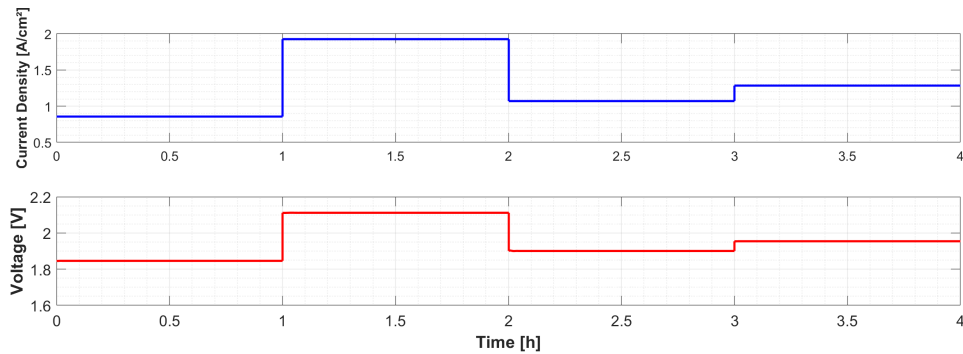

Figure 5.10: Dynamic response of current density and corresponding voltage under varying load conditions

Figure 5.11 further illustrates the thermal response of the system under the same varying load conditions by showing the changes in stack temperature and refrigerant mass flow rate in the HEX. As the current load increases, the system quickly adjusts the refrigerant mass flow to accommodate the increased heat generation, stabilising the stack temperature near the defined operational setpoint. The sharp spikes in refrigerant flow correspond to rapid changes in load, where the PI controller reacts to compensate for the thermal disturbances. The transient oscillations seen in both temperature and flow are

short-lived and settle quickly, demonstrating the controller's effectiveness in regulating the thermal dynamics. The proportional ($K_p = 1000$) and integral ($K_i = 100$) gains of the PI controller were selected based on trail-and-error approach and showed satisfactory performance (4.44). Therefore, no further tuning was performed here.
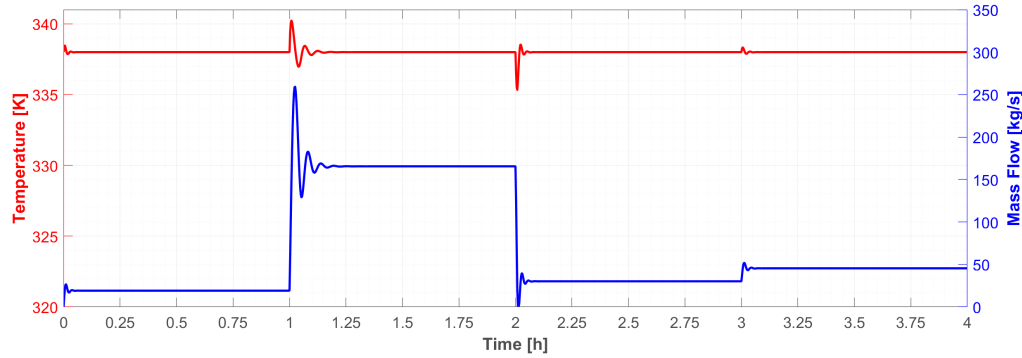

Figure 5.11: Thermal response of stack temperature and refrigerant mass flow to changing current loads

These two figures confirm that the developed model accurately captures the transient electrical behaviour of the system while also maintaining thermal stability under dynamic operation.

Figure 5.12 compares cold start scenarios at different temperature rise rates: 2.0 K/min, 1.5 K/min, and the selected 1.0 K/min. While faster heating reduces the time needed to reach the operational temperature (338 K), it increases thermal stress, which can compromise the durability of PEM stacks. Therefore, a conservative heating rate of 1.0 K/min was chosen.

In this scenario, the system is gradually heated from 298 K to 338 K in three phases: the first phase lasts 15 minutes and uses 3% current load with 250 kW of electric heating; the second phase lasts 15 minutes at 6% current load and 350 kW of heating; and the final phase continues until the end of the warm-up (12.5 minutes) with the same 6% current and increased 450 kW of heating. The full cold start takes 42.5 minutes and results in an estimated energy cost of 161 €, assuming electricity is priced at 100 €/MWh. After the system reaches its operating temperature, current load increases and H_2 production starts. Although some H_2 is produced during this phase due to the small current, it is purged from the system as the cathode outlet stream primarily consists of H_2O.

The hot start transition is illustrated in Figure 5.13, which captures the system behaviour during standby and the following ramp-up to running mode. At the beginning of the simulation, the PI controller takes a few minutes to stabilise, adjusting the electrical heating input to compensate for ambient heat losses and maintain the stack at a stable standby temperature. This standby temperature is set at 337 K, just below the full operating level, to minimise the duration of the hot start.

At 10 minute in the simulation, a hot start is triggered by supplying 8% of the nominal current load. This current input generates sufficient internal heat to raise the temperature, allowing the system to reach the operational level of 338 K within approximately two minutes. The total cost of this transition is estimated at 11 €. After reaching the target temperature, the same goes as for the cold start. Current load is increased, the heater is

deactivated, and minor temperature oscillations follow due to the sudden surplus heat from the electrochemical reactions. These transient fluctuations quickly settle as the refrigerant flow is regulated, showing the responsiveness of the thermal control strategy during transitional stages.

To keep the electrolyser in the off mode, no energy is required, while keeping the electrolyser in standby mode requires around 165 kW. A summary of duration, costs and energy requirements of the modes mentioned in this section is presented in Table 5.3.
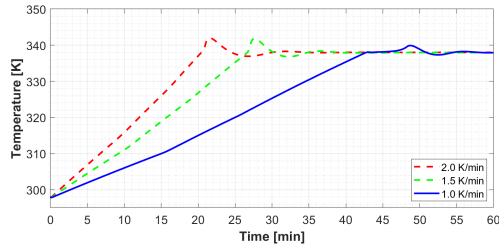

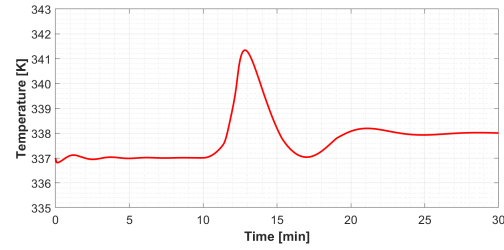**Figure 5.12:** Cold start performance of the PEM cell.

Figure 5.13: Hot start performance of the PEMEL.

Table 5.3: Duration, cost, and energy requirement associated with different transition modes.

Transition Mode	Duration [min]	Cost [€]
Cold Start	42.5	161
Hot Start	2	11

Mode	Energy Required [kW]
Shutdown Transition	0
Standby Transition	165

## 5.3 Methanol Synthesis and Distillation (MSD) Unit

This section presents a complete evaluation of the MSD system. It begins with the steady-state configuration and parameter definition for both the MS and MD subsystems. These are established using the methodologies previously discussed in Sections 4.3 and 4.4. The analysis then advances to a dynamic simulation framework, where the system's behaviour under variable load conditions is studied. Finally, a data-driven surrogate model is developed.

5.3.1 Steady State Model of MS

This subsection illustrates final operating parameters of MS unit under steady-state operation, where focus is on the reactor and separator unit. The design of the reactor is build on the CAPEX analysis (5.1), which determined the reactor's operating pressure and dimensions. A key design variable requiring further analysis is the reactor inlet temperature.

Inlet Temperature of Reactor

A sensitivity study was conducted to evaluate three inlet temperatures, as illustrated in Figure 5.14a.
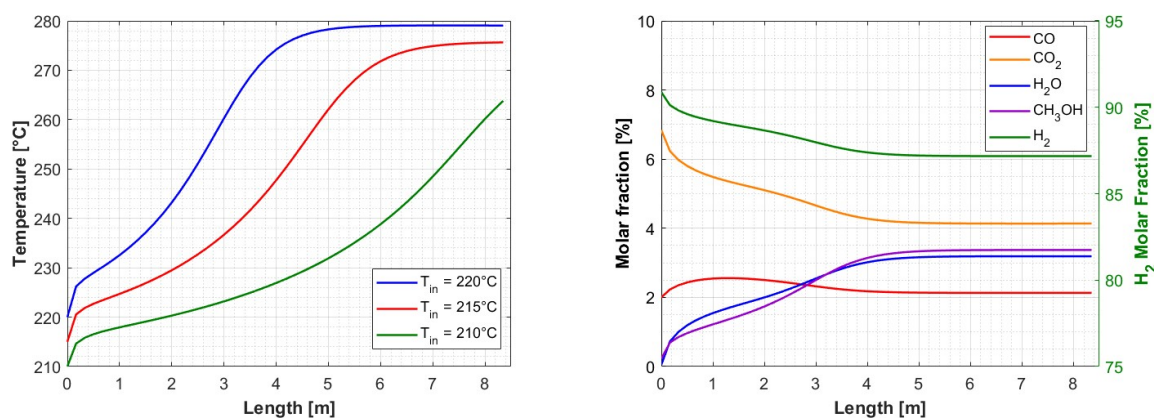
(a) Sensitivity study on the MS reactor with respect to inlet temperature.

(b) Composition profile along the reactor length for the selected 220 °C inlet temperature.

Figure 5.14: MS reactor performance: (a) effect of varying inlet temperature, (b) profile composition under optimal conditions.

Higher inlet temperatures were not tested due to constrains already mentioned in Section 4.3.4. At 488 K, the reactor closely approaches thermodynamic equilibrium near its outlet, ensuring efficient conversion while leaving minimal margin for catalyst degradation over time. At 483 K, equilibrium is not reached, implying a need for significantly greater reactor volume. Based on these findings, an inlet temperature of 493 K was selected as optimal. With this condition fixed, the species composition profile along the reactor length is shown in Figure 5.14b where progression of the MS reaction is shown and approach to equilibrium.

Separator Unit

Following the reactor, a separation unit (SEP in Figure 4.6) is employed to condense most of the MeOH and H_2O into the liquid phase, while gaseous components (CO_2, H_2, CO) are retained in the vapour phase. Figure 5.15 presents a sensitivity study on separator temperature, revealing that lower temperatures enhance MeOH recovery by reducing its vaporisation.
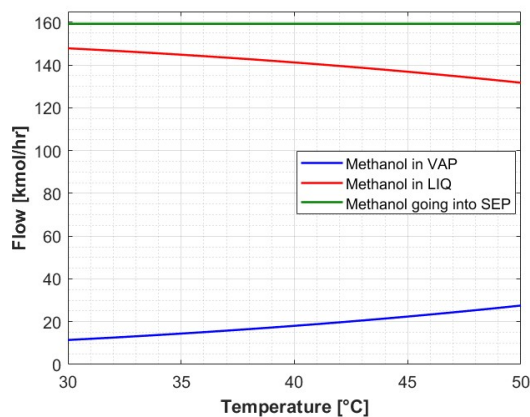

Figure 5.15: Impact of separator temperature on MeOH distribution between vapour and liquid phases.

A temperature of 303 K was chosen, considering a minimum feasible coolant temperature of 293 K. The condensed liquid is then directed to a second flash separator (SEP2) that operates at a pressure of 3 bar. The reduction in pressure promotes the removal of dissolved gases, particularly CO_2, H_2, and CO, through desorption in accordance with Henry's Law. Additionally, operating at this pressure ensures compatibility with the downstream distillation column, which functions close to ambient pressure.

Performance with and without Recycle

An initial simulation was performed using a single-pass configuration, where fresh CO_2 and H_2 enter the reactor without any form of recycling. Under these conditions, the MeOH yield was limited to just 13.7%, indicating that a significant portion of the reactants remained unconverted. To address this inefficiency, a vapour–liquid separator and recycle compressor were introduced. With the recycle loop in place, the overall MeOH yield increased dramatically to 98.5%, demonstrating the critical role of recycling in achieving high conversion efficiency.

MS Parameters

The Table 5.4 summarises all specified parameters used in the finalised MS section of the MSD unit.

Table 5.4: Key operating and design parameters for the MS section

Parameter	Value	Unit
Operating conditions		
H_2 flow rate	450	kmol/h
CO_2 flow rate	150	kmol/h
Temperature of feed gases	333	K
Pressure of feed gases	70	bar
Ratio for purging gas	0.1	%
Pressure drop across heat exchangers	0.5	bar
Methanol reactor		
Reactor inlet temperature	493	K
Reactor inlet pressure	66	bar
Gas hourly space velocity (GHSV)	10000	h^{-1}
Inner diameter	1.67	m
Length	8.35	m
Wall thickness	0.022	m
Reactor wall density	7700	kg/m^3
Catalyst		
Particle density	1950	kg/m^3
Porosity of catalyst bed	0.385	–
Catalyst particle diameter	0.006	m
Gas-liquid separator (SEP)		
Separator temperature	303	K
Separator pressure	64	bar
Diameter	1.1	m
Length	2.2	m
Gas-liquid separator (SEP1)		
Separator temperature	305	K
Separator pressure	3	bar
Diameter	1.1	m
Length	2.2	m
Compressor		
Isentropic efficiency	0.75	–
Discharge pressure	67	bar
Heat exchanger (HEX)		
Heat exchanger area	460	m^2

5.3.2 Steady State Model of MD

In line with the MS design, this subsection presents the final steady-state parameter configuration of the MD module. Following the methodology outlined in 4.4, an optimised configuration of the distillation column was achieved by focusing on the reflux ratio, which critically affects both separation performance and the trade-off between capital investment and energy consumption.

Shortcut Analysis: Reflux Ratio vs. Theoretical Stages

Figure 5.16 illustrates the relationship between reflux ratio and the corresponding minimum number of theoretical stages, as estimated by the DSTWU shortcut model. As expected, higher reflux ratios reduce the number of stages required for separation, whereas lower reflux ratios demand significantly more stages. A reflux ratio of 0.8 represents a

practical lower limit; further reductions result in a disproportionately large increase in required stages, making such configurations economically and technically inefficient. Based on this sensitivity, a range of reflux ratios-1.4, 1.2, 1.0, 0.9, 0.85, and 0.8—was selected for detailed evaluation in the RadFrac model.
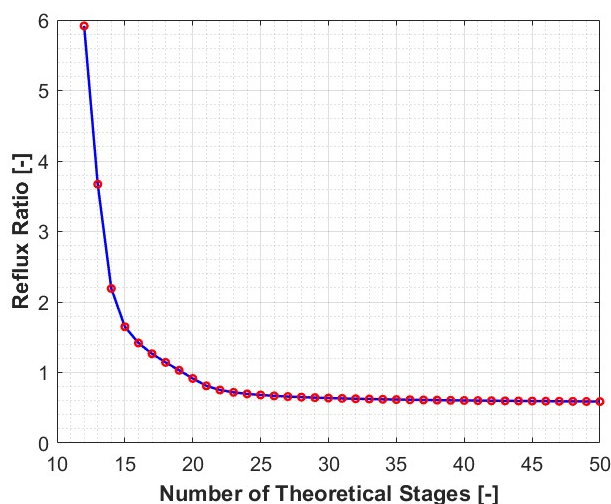

Figure 5.16: Reflux ratio vs. minimum number of theoretical stages from DSTWU analysis

RadFrac Analysis: Required Equilibrium Stages

The selected reflux ratios were then simulated using the RadFrac model to determine the minimum number of equilibrium stages required to achieve the specified product purities. As shown in Figure 5.17, lower reflux ratios significantly increase the number of required stages. At a reflux ratio of 0.8, the column requires approximately 90 equilibrium stages, indicating that this value is close to the theoretical minimum. Due to the impractically high column height and associated capital cost, the 0.8 case was excluded from further consideration.
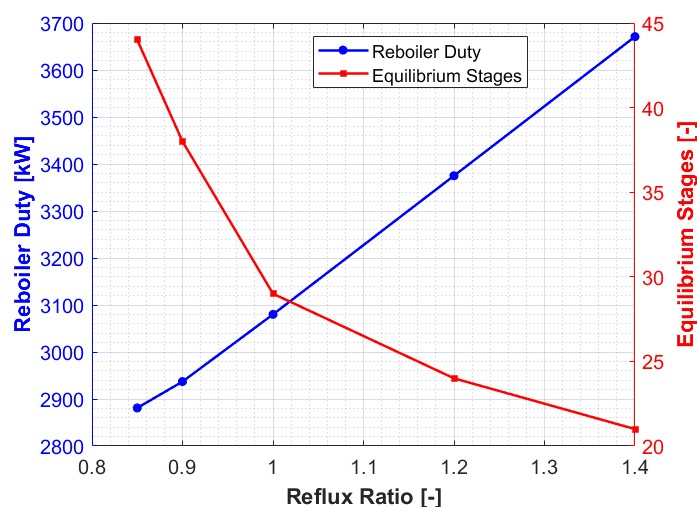

Figure 5.17: Number of equilibrium stages and reboiler duty vs. reflux ratio from RadFrac simulation

Total Annual Cost (TAC) Optimisation

To evaluate the economic trade-offs of each configuration, both CAPEX and OPEX were calculated based on RadFrac output. As depicted in Figure 5.18a, lower reflux ratios require more stages, increasing CAPEX. Conversely, higher reflux ratios increase internal liquid flow and reboiler duty, thereby raising energy consumption. This inverse relationship highlights the need for a balanced operating point. To identify the most economically favourable design, the total annual cost (TAC) was calculated for each reflux ratio scenario, as shown in Figure 5.18b. The TAC combines both capital and operating costs. The analysis reveals that reflux ratios of 0.85 and 0.9 yield similar TAC values. However, a reflux ratio of 0.9 was selected as the final design point. This choice offers a practical compromise by reducing column height while staying on the conservative side of energy consumption. It is important to note that for this TAC estimation, energy costs were based on [54] to ensure fair comparison. In future sections phases, it will be assumed that energy is supplied by electric heaters.
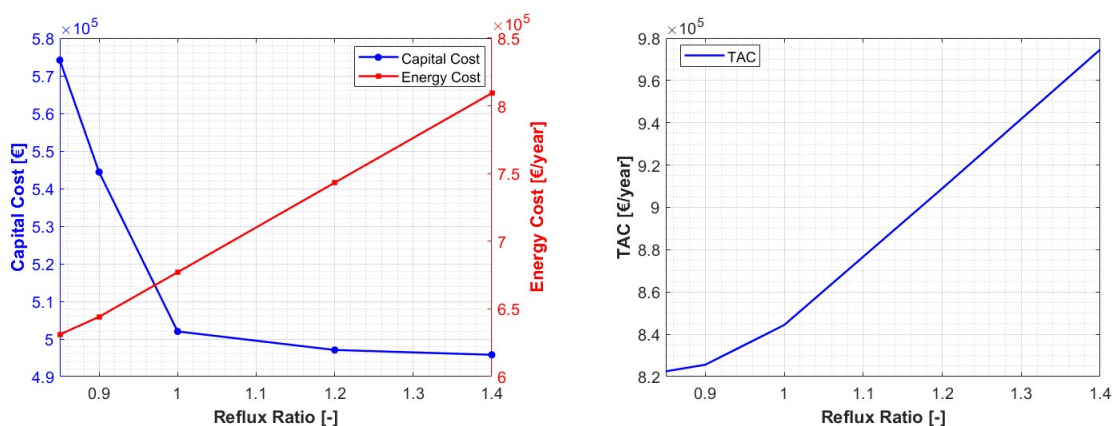
(a) Capital and energy costs as a function of reflux ratio.

(b) Total annual cost (TAC) as a function of reflux ratio.

Figure 5.18: Economic evaluation of distillation configurations: (a) trade-off between capital and energy costs, (b) total annual cost for different reflux ratios.

MD Parameters

Table 5.5 summarises all specified parameters used in the MD part of the overall MSD system.

Table 5.5: Key operating and design parameters for the MD section

Parameter	Value	Unit
Distillation column (D1)		
Feed inlet temperature	348	K
Number of stages	38	–
Stage number for feed	20	–
Pressure at stage 1	1.1	bar
Pressure drop per stage	0.007	bar
Column type	Trayed (sieve)	–
Tray spacing	0.61	m
Diameter (stage 1–29)	1.225	m
Diameter (stage 30–38)	1.05	m
Total column height	22.5	m
Height of sump	1.56	m
Diameter of sump	1.05	m
Gas-liquid separator (SEP2)		
Diameter	1.18	m
Height	2.36	m
Pump (P1/P2)		
Discharge pressure	2.0	bar
Efficiency	0.8	–

5.3.3 Dynamic Operation of MSD

The dynamic modelling of the MSD process was carried out using Aspen Plus Dynamics. The initial conditions for the dynamic simulations were derived from steady-state results obtained via Aspen Plus, as detailed in Sections 5.3.1 and 5.3.2, where the final process configurations and operating parameters were established. The complete MSD system flowsheet, combining both the MS and MD units, is shown in Figure 5.19.

Controller Settings

To enable dynamic simulation, a comprehensive control structure was implemented across both MS and MD sections. Controllers were installed and tuned following the methodology described in Section 4.6.5. Tables 5.6 and 5.7 summarise the key controllers used in the model, including the controlled variables, manipulated units, and tuning parameters.

Table 5.6: Controller settings and parameters for the MS section

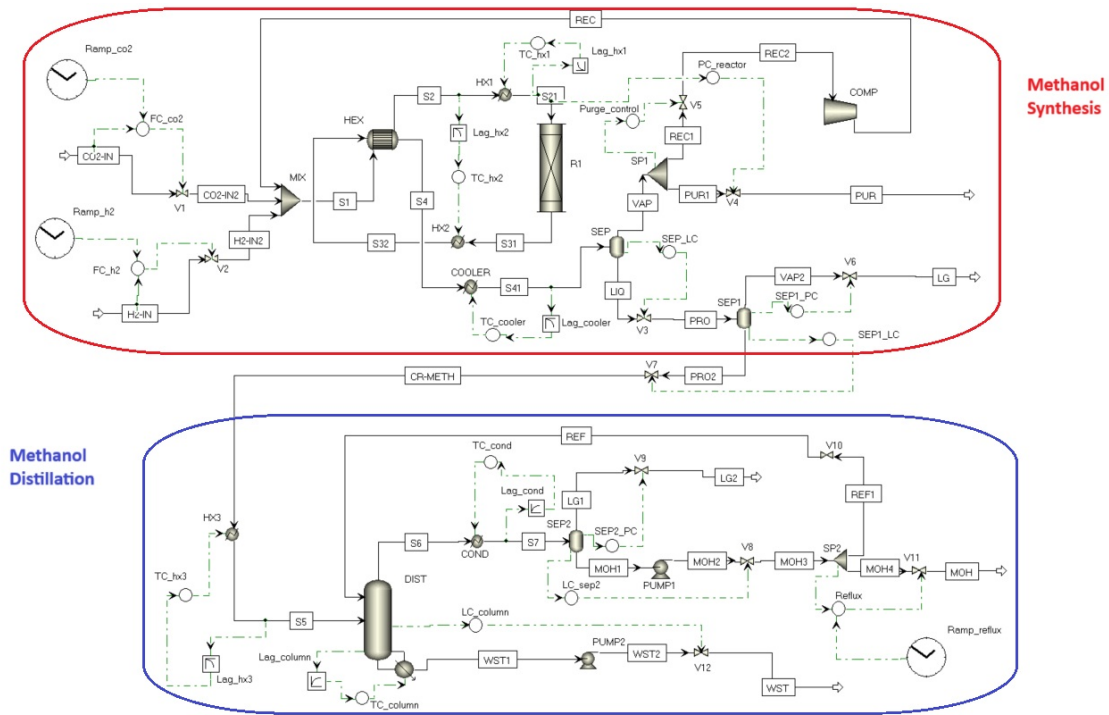| Tag	Controlled Objective	Actuator	Range of Change	P	I (min)
FC_co2	CO_2 flow rate	Valve V1	0–100%	0.93	0.264
FC_h2	H_2 flow rate	Valve V2	0–100%	0.99	0.264
TC_hx2	Temperature of stream S2	HX2	−3.2 to 0 MW	25	20
TC_hx1	Reactor inlet temperature	HX1	0 to 2 MW	25	20
Purge_control	Ratio of purging flow	Valve V5	0–100%	1.72	0.264
PC_reactor	Reactor inlet pressure	Valve V4	0–100%	2	10
TC_cooler	Temperature of stream S41	COOLER	−8.5 to 0 MW	5.71	0.528
SEP_LC	Liquid level of SEP	Valve V3	0–100%	10	–
SEP1_PC	Pressure of SEP1	Valve V6	0–100%	20	12
SEP1_LC	Liquid level of SEP1	Valve V7	0–100%	10	–

Figure 5.19: Flowsheet of the integrated MSD system used for dynamic simulations.

Table 5.7: Controller settings and parameters for the MD section

| Tag	Controlled Objective	Actuator	Range of Change	P	I (min)
TC_hx3	Temperature of S5	HX3	0 to 0.7 MW	456	0.528
LC_column	Liquid level of column sump	Valve V12	0–100%	10	–
TC_column	Temperature of stage 31	Reboiler	0 to 5.9 MW	95.2	1.716
TC_cond	Temperature of S8	HX5	−5.8 to 0 MW	6.44	0.396
LC_sep2	Liquid level of SEP2	Valve V8	0–100%	2	–
Reflux	Reflux ratio for D1	Valve V11	0–100%	1.5	0.264
SEP2_PC	Pressure of SEP2	Valve V9	0–100%	20	12

Dynamic Simulation: Load Variation Scenario

To assess the dynamic behaviour of the integrated MSD system, a 15-hour simulation was conducted. The scenario involves a load transition from full capacity (100%) down to partial load (40%) and then back to full load. Due to limitations in the compressor model, the system cannot operate below 40% load. As a result, 40% is set as the minimum operational limit and will be used consistently throughout the rest of the report, including in the optimisation phase. This test is intended to evaluate system flexibility and control performance under varying operating conditions.

In the steady-state design, the maximum H_2 feed was set at 450 kmol/hr. However, for dynamic simulations and all subsequent analyses, the maximum H_2 input was adjusted to 432 kmol/hr to reflect the real production constraint of the electrolyser. For load changes during the operation changes, a ramp rate of 60% per hour was imposed, corresponding to a change of 1%/min.

Figure 5.20a shows the dynamic response of the main process streams. The reduction in

load occurs between hours 1 and 2, while the system returns to full load between hours 8 and 9. As expected, the methanol-rich crude product (CR-METH) stream and purge (PUR) stream follow the trends of the H_2 and CO_2 inputs. The PUR stream plays a crucial role in maintaining process stability by removing excess reactants or inert components that may accumulate over time. For instance, impurities such as N_2 or CH_4 often present in biogas-derived CO_2. Additionally, since the PUR stream is typically rich in H_2, it can be repurposed as a fuel for internal combustion or other energy needs within the plant.
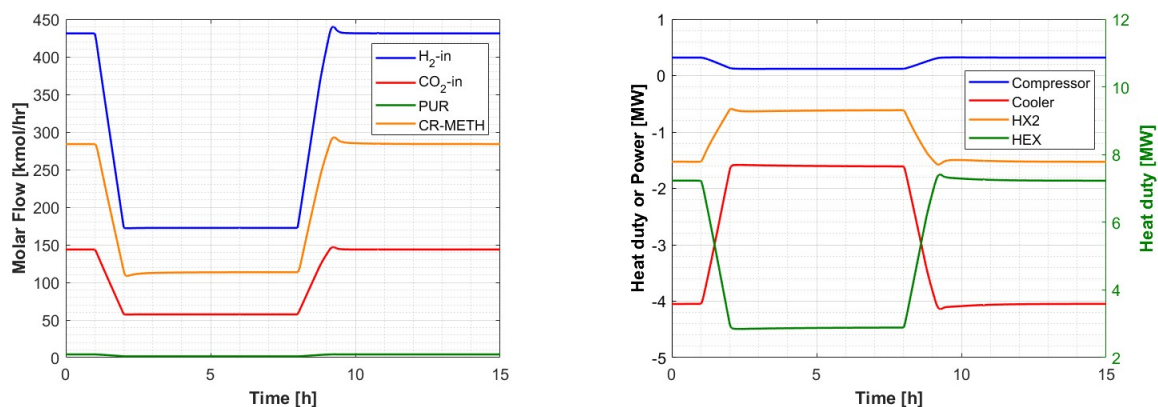
(a) Dynamic response of feed and product streams in MS during load transition.

(b) Compressor and heat exchanger duty profiles during dynamic load transition.

Figure 5.20: Dynamic simulation of the MS process: (a) molar flow of key streams, (b) heat and power duty response.

Figure 5.20b presents the heat duty and power profiles of MS key process units. All units respond smoothly, showing near-linear transitions during ramp-down and ramp-up periods. The largest thermal duty is observed in the cooler, which lowers the temperature of the methanol–water stream before entering the separator. Despite being a low-grade heat source, this stream offers potential for integration with district heating networks. Heat exchanger HX2 is used to recover part of the high-grade heat from the reactor outlet, which can partially reduce the reboiler's thermal demand in the distillation section. Compressor power and HEX duty remain well-behaved, indicating a well-tuned control structure for handling load variations.

Figure 5.21a compares the dynamic response of the product streams, MeOH (MOH) and wastewater (WST), with the inlet CO_2 flow. The results demonstrate a near-linear correlation between the feed and product flowrates. However, observable time lags are present during both ramp-down and ramp-up transitions. In the ramp-down case, the product streams stabilise approximately one hour after the change, whereas the ramp-up scenario requires nearly two hours to return to a quasi steady state. These lags are a result of the system's internal holdup and thermal inertia.
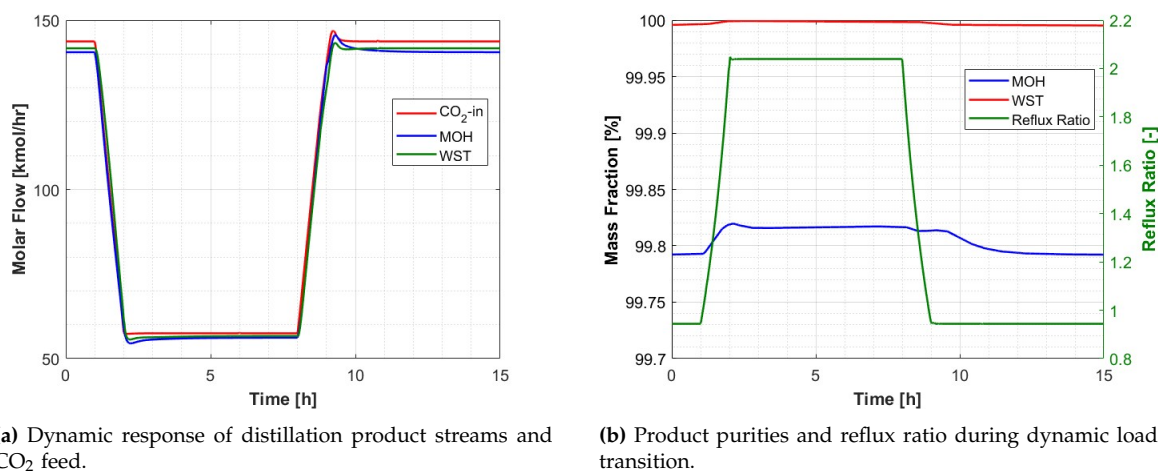
(a) Dynamic response of distillation product streams and CO_2 feed.

(b) Product purities and reflux ratio during dynamic load transition.

Figure 5.21: Dynamic performance of the MD system during ramp-down and ramp-up operation.

The Figure 5.21b, shows the purity of the MOH and WST streams, along with the dynamic variation in reflux ratio. Throughout the simulation, the methanol purity consistently remained above 99.7 wt%, while the water stream purity exceeded 99.9 wt%, thereby satisfying product quality specifications (mentioned in 4.4.1). As the system load decreased, the reflux ratio was increased manually from 0.95 to 2.05 to maintain hydraulic stability within the column. At reduced loads, the internal vapour and liquid flows are decreased, which can affect efficient mass and heat transfer of the distillation column. The increased reflux ratio at 40% load was selected based on prior Aspen Plus hydraulic analysis, which ensured that operational constraints were not violated.
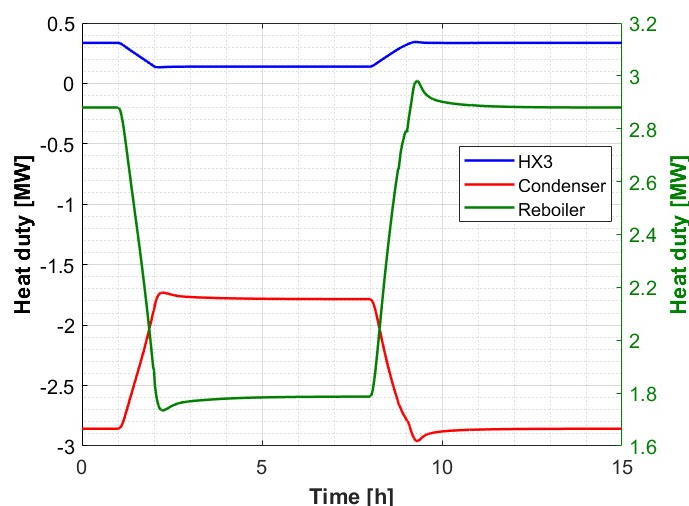

Figure 5.22: Dynamic heat duty profiles in the MD section.

Figure 5.22 presents the corresponding heat duties of the condenser, reboiler, and a heat exchanger (HX3). Unlike the rest, the reboiler duty in the distillation system does not scale linearly with system load. This is a direct result of the increased reflux ratio during partial load operation. While the system operates at full load, the reboiler duty is approximately 2.88 MW, decreasing to 1.78 MW at 40% load. This nonlinearity has important implications

for system efficiency and overall energy utilisation.

The overall system efficiency during dynamic operation is illustrated in Figure 5.23. Both the MS and MD efficiencies show fluctuations during transitions between load levels. These deviations can be primarily attributed to the thermal inertia and holdup effects within the system components. Additionally, suboptimal tuning of controllers may have contributed to the magnitude of these fluctuations. After the system stabilises post-transition, the MS unit maintains an efficiency of approximately 87.8%. In contrast, the MD unit experiences a notable efficiency drop from 87.8% at full load to 83% at 40% load. This decline is directly linked to the increased reflux ratio required at partial load, which, as previously discussed, elevates reboiler duty and energy consumption. Consequently, the overall system MSD efficiency decreases from 77.8% at 100% load to 74.2% at 40% load. Despite the dynamic transitions, the system successfully reaches quasi-steady-state conditions within approximately three hours.
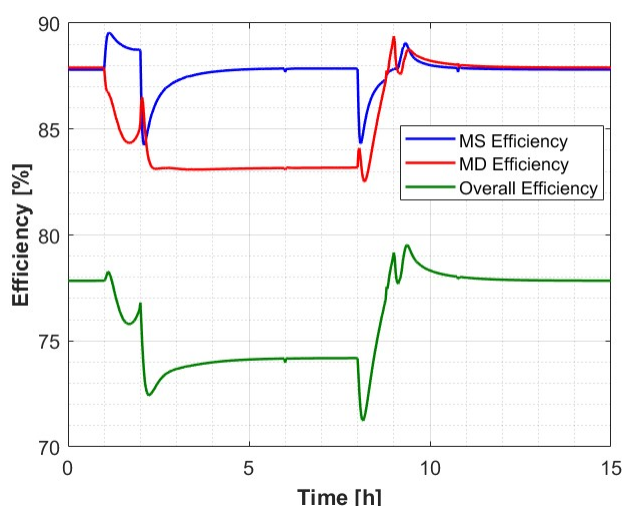

Figure 5.23: Dynamic efficiency profiles for MS, MD and the overall system (MSD).
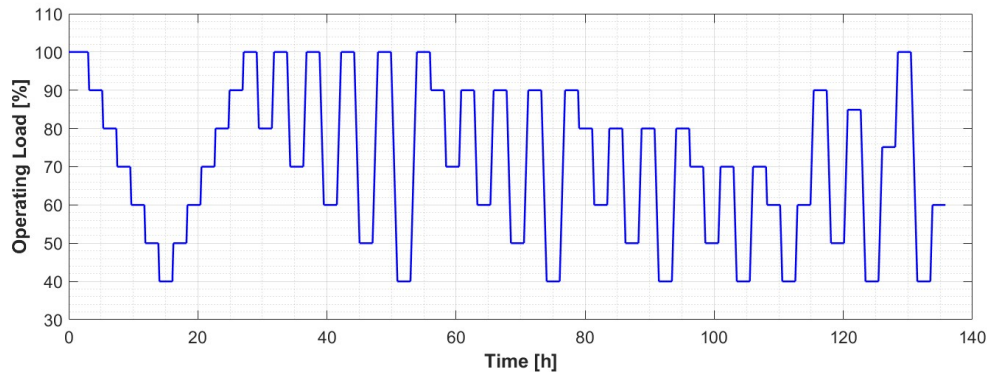
5.3.4 Surrogate Model

The surrogate model for the MSD system was developed based on dynamic simulation results obtained under varying load conditions. The key performance indicators (KPIs) include both the hydrogen flow rate, which serves as the model input, and a set of output variables that reflect the system's thermal and flow characteristics. These KPIs (presented in Table 5.8) were selected specifically to support the optimisation case study introduced in earlier chapters. The H_2 flow rate represents the operating load of the system, while the other KPIs capture its dynamic response.

Parameter	Unit	Range
Flow rate of MOH	kmol/h	56.3 to 140.7
Hydrogen flowrate (H_2)	kmol/h	172.4 to 431
Reboiler duty (Q_{reb})	MW	1.78 to 2.88
Heat exchanger duty (HX2)	MW	-1.52 to -0.62
Heat exchanger duty (HX3)	MW	0.14 to 0.34
Compressor power consumption	MW	0.12 to 0.32
Cooling or excess heat duty	MW	-4.06 to -1.61

Surrogate Model Dataset Generation

A dedicated dataset was generated to support the training, validation, and testing of the surrogate model. This dataset was designed to reflect a wide range of operating conditions and to capture the dynamic behaviour of the MSD system under load transitions used in the optimisation case study. To simulate load variations, a ramp rate of 60% per hour was applied. The load was held constant for two hours between transitions, based on the findings presented in Section 5.3.3, which showed that the system reaches quasi steady-state within this timeframe. As a result, each operating point in the dataset corresponds to a near steady-state condition, making it suitable for supervised learning.

Figure 5.24: Operating load variation over time used for training, validation, and testing of the surrogate model.

From Figure 5.24, the complete dataset spans 136 hours and contains 54 load changes. Sampling was performed at 90-second intervals to ensure sufficient resolution for training a time-series model. The dataset was divided into two segments. The first segment, covering the time period from 0 to 114 hours, includes 46 load changes. It features load levels restricted to rounded values between 40% and 100%. This portion of the dataset was used for training and validation. The second segment, covering the final 21 hours (from 114 to 136 hours), contains the remaining 8 load changes and was reserved for testing the model's predictive performance on unseen data

Surrogate Modelling with LSTM model

The surrogate model is built using a Long short-term memory (LSTM) neural network, previously described in Section 4.7. The model was implemented and trained in MAT-

LAB. Evaluation of the model on the testing dataset yielded strong results, with MAE of 0.0229 and an R^2 of 1.0, indicating excellent predictive accuracy. Figure 5.25 shows the LSTM model's prediction of flow rate of MOH compared with the actual dynamic data.
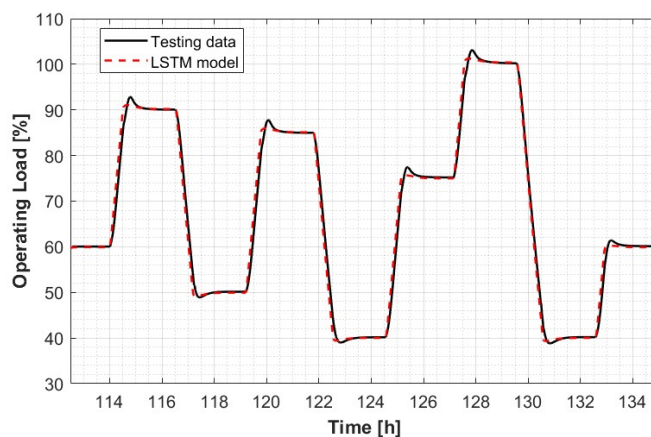

Figure 5.25: LSTM model prediction compared to testing data.

It is important to note that the surrogate model was not directly embedded in the optimisation model. Instead, its primary purpose was to validate the feasibility of simplifying the calculation of MeOH production across varying load conditions. This simplification was necessary to reduce computational time and was implemented in the optimisation framework.

5.4 Integrated System Overview

To establish the link between the PEMEL system and the MSD system, a complete process configuration is presented, as illustrated in Figure 5.26. This integrated setup serves as the foundation for the optimisation model and presents the primary energy flows relevant to the overall process.
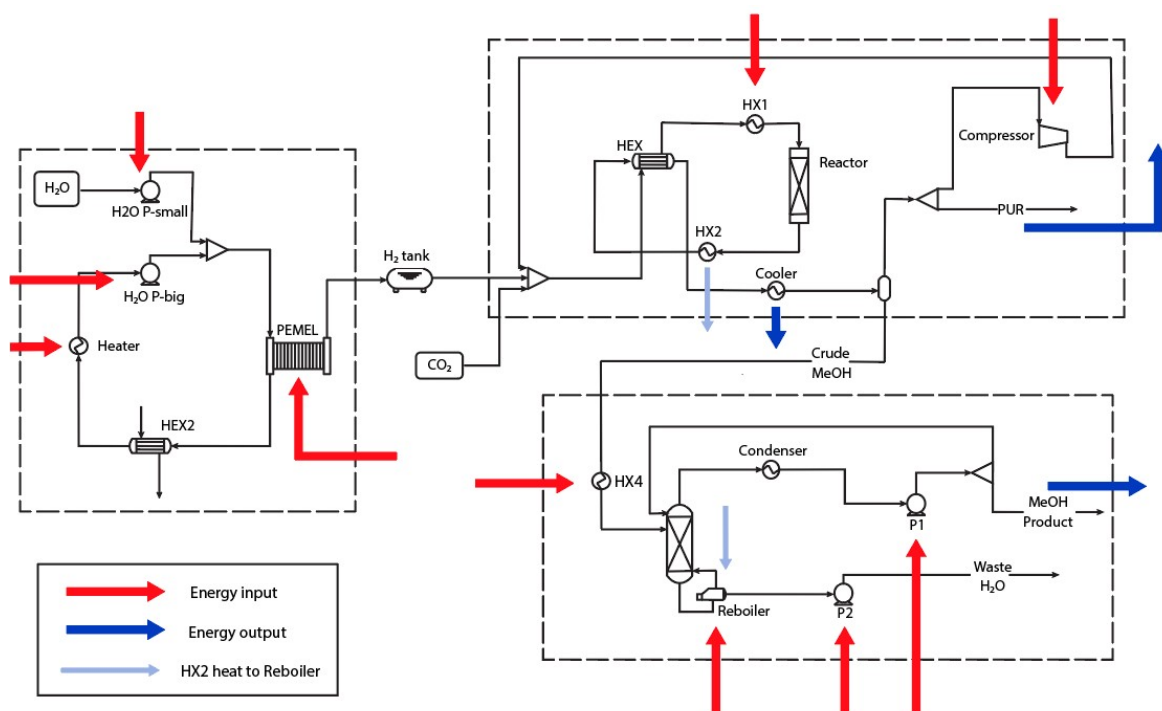
Figure 5.26: Overall system configuration connecting PEMEL and MSD process, highlighting energy inputs and outputs.

The system consists of two major subsystems: the PEMEL system on the left and the MSD section on the right. These two units are interconnected through a H_2 buffer tank, which improves the overall stability and flexibility of the system. The red arrows represent the main energy inputs, including electrical energy for the electrolyser, pumps, compressor, and all required heat duties. The blue arrows represent the useful energy outputs of the system, such as the final MeOH product, the purge stream, which contains a high concentration of H_2 and can possibly be utilised for combustion, and the excess heat from the cooler, which may be used for district heating. The light blue arrow indicates internal heat recovery within the system, where heat from heat exchanger HX2 is transferred to the distillation reboiler, reducing its external energy demand. This integrated system configuration establishes the foundation for dynamic operation scheduling, which has been discussed in detail in the following section

5.5   Optimisation Case Study Results

In the previous section, the overall system scheme (Figure 5.26) was presented after independently analysing different system components. These components are integrated into a unified PtMeOH system in order to capture dynamic interactions between subsystems and to obtain the optimisation of plant. The following optimisation case study demonstrates how dynamic electricity pricing can be leveraged to minimise MeOH production costs while respecting the operational limitations of each subsystem while meeting the defined demand.

The section is structured to first show the electricity price framework and optimisation parameters, followed by evaluation of different operational strategies, annual performance

assessment, and sensitivity analysis of key economic drivers.

5.5.1 Electricity Price Input and Demand Structuring

To enable the optimisation of electrolyser operations, a detailed hourly electricity price dataset was employed. Provided through external collaboration, this year-long profile is presented in Figure 5.27. No further evaluation of its underlying trends or forecasting methods is conducted, as the dataset is adopted directly.
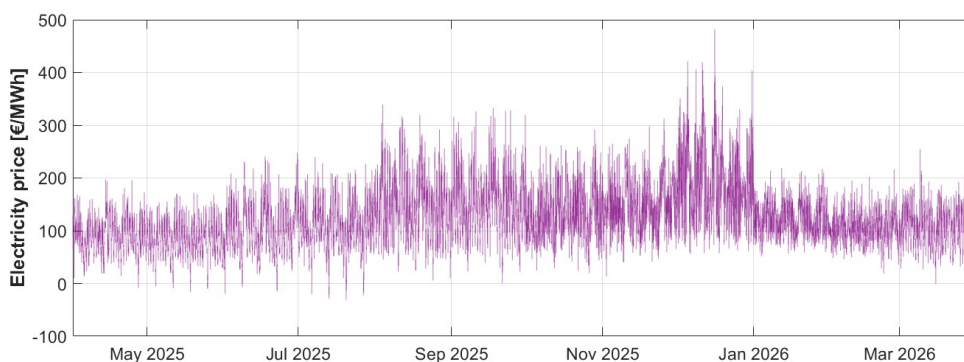

Figure 5.27: Hourly electricity price prediction over a one-year period.

Implementing a full-year hourly optimisation would be extremely demanding in terms of computational time and power. To address this challenge, a week-based discretisation strategy was adopted. Electricity prices were averaged over each week, and these weekly average values were used to assign a weighted MeOH production demand across the year. The underlying assumption is that weeks with lower electricity prices correspond to higher production potential and vice versa. The result of this structuring is shown in Figure 5.28, which presents both the weekly average electricity price and the corresponding MeOH production demand.

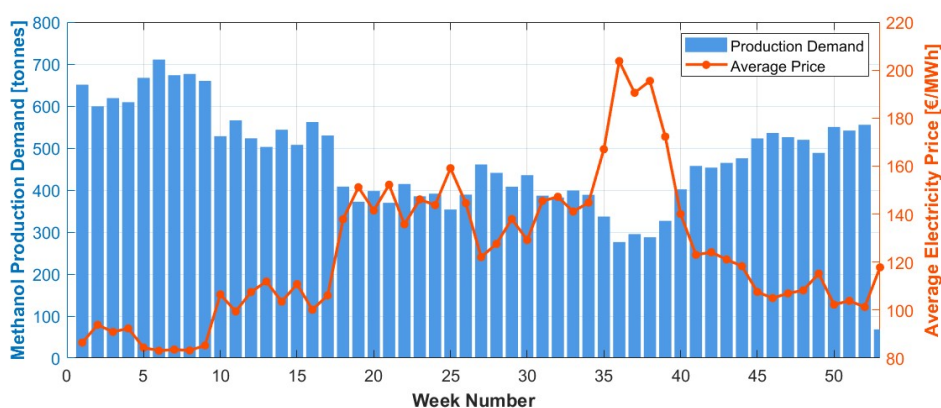**Figure 5.28:** Weekly MeOH production demand based on electricity price averages.

It is important to emphasise that while weekly average electricity prices were used to define the demand distribution, all optimisation simulations were still performed using the original hourly resolution data. This ensures that the dynamic behaviour of the electricity market is fully captured during the optimisation runs.

5.5.2 Optimisation Parameters

The regression analysis of the electrolyser power consumption data gave a quadratic relationship between the operational load percentage and electricity consumption. Figure 5.29 presents the regression results, showing great agreement between the calculated data points from the Simulink model and the fitted regression curve ($R^2 = 0.99$). The resulting quadratic regression parameters are in the Table 5.9
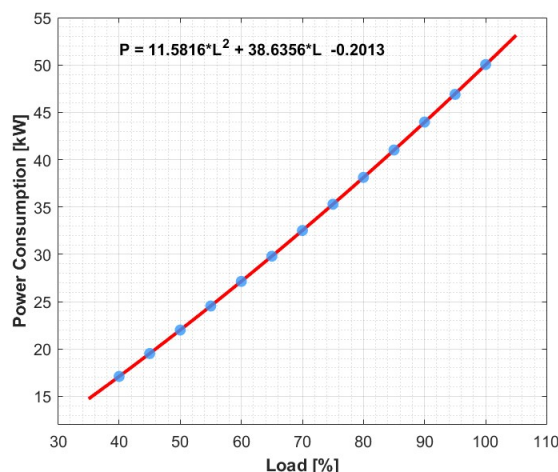

Figure 5.29: Electrolyser power consumption regression model showing quadratic relationship between load percentage and electricity consumption

The matrix representation of the MeOH production rates is presented in Figure 5.30. This matrix captures the dynamic relationship between electrolyser load transitions and the resulting MeOH production rates in kmol/h, accounting for the transient behaviour of the MeOH synthesis system when H_2 flow rates changes. In this matrix, each row represents the electrolyser load from the previous time step (l'), while each column represents the current time step load (l). The matrix element $M_{l',l}$ provides the MeOH production rate when transitioning from load l' to load l. Diagonal elements from the matrix represent steady-state MeOH production rates for constant H_2 supply, while off-diagonal elements capture transient production effects during load transitions, reflecting the dynamic response of the MeOH synthesis reactor to changing H_2 flow rates. This matrix-based approach enables the optimisation algorithm to accurately evaluate MeOH production for any sequence of electrolyser load changes while maintaining computational efficiency compared to implementing the full Aspen Dynamics surrogate model directly within the optimisation framework.

To validate the accuracy of the matrix-based approach, a comparative analysis was conducted using optimisation results from a representative week. The electrolyser load profile obtained from the optimisation algorithm was applied as input to the computationally intensive Aspen Dynamics surrogate model. Figure 5.31 presents the MeOH production profiles obtained from both approaches throughout the validation period. The comparison demonstrates great agreement between the two methods, with total MeOH production differing by less than 1% over the entire week. This validation confirms that the matrix-based

	TO						
	40	**50**	**60**	**70**	**80**	**90**	**100**
40	**56.28**	68.13	77.71	85.03	89.41	91.77	92.66
50	58.29	**70.35**	82.72	91.79	99.49	104.69	109.47
60	62.78	71.90	**84.42**	96.70	106.60	114.97	118.89
70	69.74	76.76	86.04	**98.49**	110.80	120.72	128.84
80	78.25	82.95	90.50	100.00	**112.56**	125.23	136.03
90	89.24	92.13	95.90	103.64	113.68	**126.63**	139.56
100	97.97	102.48	103.92	108.72	117.35	127.33	**140.70**

Figure 5.30: MeOH production transition matrix [kmol/h] for electrolyser load changes.

approach maintains high accuracy while providing the computational efficiency required for practical optimisation implementation.
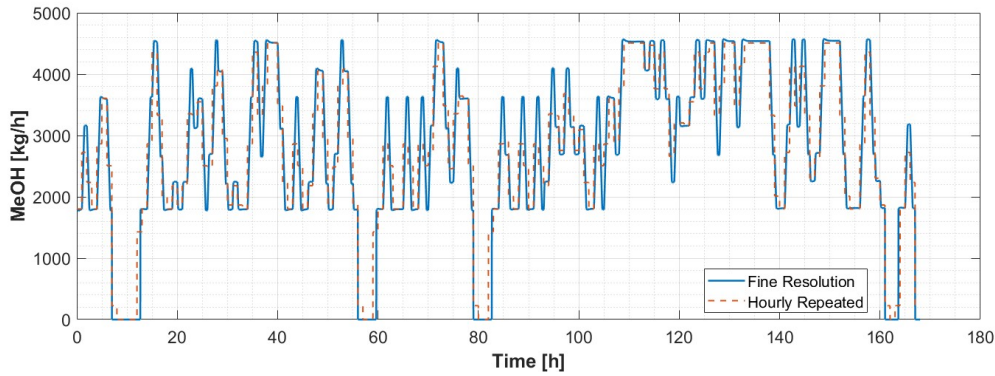

Figure 5.31: Validation comparison between matrix-based approach and surrogate model for MeOH production over one week

The general concept of the H_2buffer tank is described in Section 4.9.1. To allow for a controlled ramp-down of the MSD system during electrolyser shutdowns, the tank must store approximately 17 kmol of H_2. In addition, to compensate for the difference in response times between the electrolyser, which is able to change load immediately, and the MSD system, which requires a gradual ramp-up and ramp-down period, an additional 144 kmol of H_2 storage is needed. This results in a total storage requirement of 161 kmol of H_2, which determines the size of the tank. Assuming a storage pressure of 70 bar, a temperature of 60 °C, and a compressibility factor Z=1.07, the total tank volume is calculated to be approximately 61.4 m^3. This value is considered reasonable when compared to the study by Sollai [13], which reports a 20 m^3 storage tank for a 6 MW system operating at 200 bar. Further simulation or optimisation of the buffer tank design was not conducted, as it falls

outside the scope of this work. However, one clear opportunity for improvement would be to increase the hydrogen storage pressure, which would reduce the required tank volume for the same storage capacity.

Finally, Table 5.9 presents the complete set of parameters employed in the optimisation framework, including economic, operational, and system constraint parameters.

**Table 5.9:** Parameters of the optimisation model

Description	Parameter	Value	Unit	Source
System Configuration				
Optimisation time resolution	-	1	hour	4.9.1
AC/DC conversion loss	-	5	%	4.9.4
Flow Ramp Rates				
MSD ramp rate (operation)	-	60	%	5.3.3
MSD ramp rate (transition)	-	1000	%	4.9.4
Temporal Duration				
MSD flow ramp duration	$D^{\text{MSD-ramp}}$	6	min	4.9.4
MSD reactor heating duration	$D^{\text{MSD-heating}}$	39	min	4.9.4
MSD reactor cooling duration	$D^{\text{MSD-cooling}}$	90	min	4.9.4
Cold start duration	D^{cold}	42.5	h	5.2.2
Hot start duration	D^{hot}	2	h	5.2.2
Tank filling duration	D^{tank}	7	h	5.2.2
Power Consumption				
quadratic regression parameter	a	11.5816	-	5.5.2
quadratic regression parameter	b	38.6356	-	5.5.2
quadratic regression parameter	c	-0.2013	-	5.5.2
Standby power consumption	$E^{\text{con-SB}}$	0.165	MW	5.2.2
MSD power consumption at 100%	$E^{MSD}_{1,1}$	2.017	MW	4.9.4
MSD power consumption	E^{MSD}_l	$E^{MSD}_{1,1} \cdot \lambda_l$	MW	4.9.5
MSD standby power	$E^{\text{MSD-SB}}$	$0.2E^{MSD}_{1,1}$	MW	[65]
MSD ramp-up/down power	$E^{\text{MSD-ramp}}$	$0.4E^{MSD}_{1,1}$	MW	5.2.2
Economic Costs				
Cold start cost	C^{cold}	161	€	5.2.2
Hot start cost	C^{hot}	11	€	5.2.2
CO_2 credit price	C^{CO_2}	55.3	€/tonne	[10]
Excess heat value	C^{heat}	30.2	€/MW	[10]
Methanol Production				
MeOH yearly demand	-	25000	tonne	-
MeOH production rate during start	M^{start}	29.67	kg/min	5.5.2

### 5.5.3 Operating Modes and Optimisation Phases

To evaluate the impact of operational flexibility on MeOH production cost, two optimisation models were developed, each representing different levels of control over electrolyser operation. The first model, referred to as Phase 1, includes three discrete operating modes: running (at fixed 100% load), standby, and shutdown. The second model, Phase 2, extends this by allowing variable load operation between 40% and 100%, in addition to the other two modes. These models are used to calculate and compare the annual MeOH production cost per tonne and to assess how load flexibility influences economic performance.

During periods of standby or shutdown of electrolyser, the MSD system is assumed to remain in standby mode. As noted above, the year is divided into weekly intervals, each optimised independently using the full hourly electricity price profile and the corresponding weekly production target. To visualise the impact of different optimisation strategies, three representative weeks from Figure 5.28 are selected, one with the lowest electricity price (week 6), one with the highest electricity price (week 36) and one with the median electricity price (week 43).
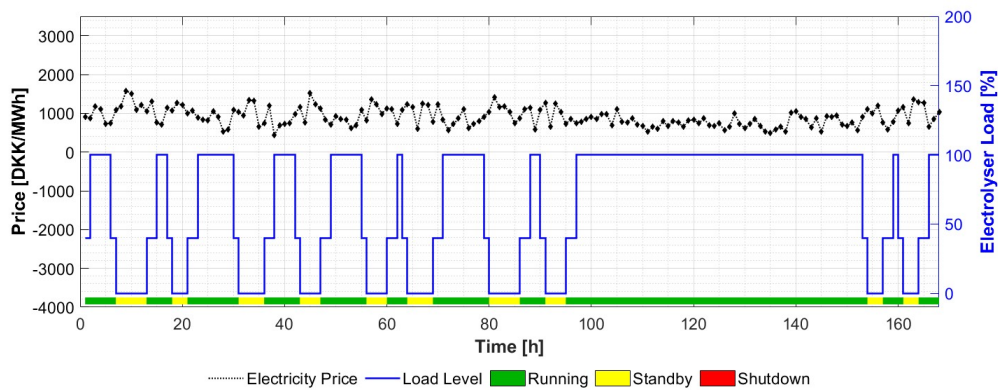
The Figures 5.32 and 5.33 below show the electrolyser's operation profiles for these three weeks under both Phase 1 and Phase 2 models, respectively.
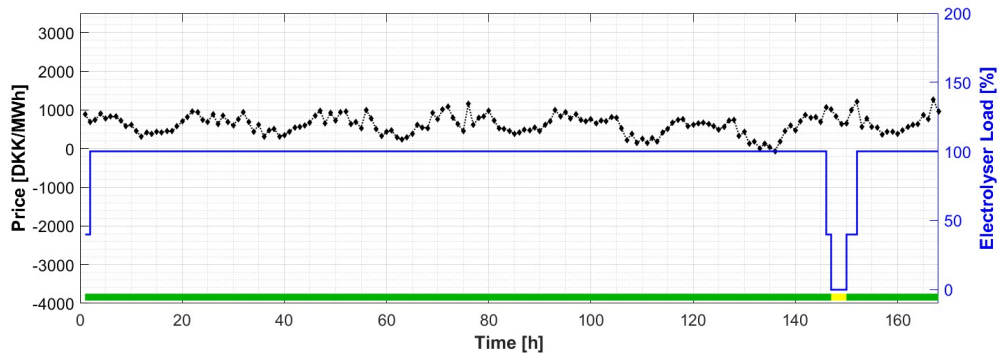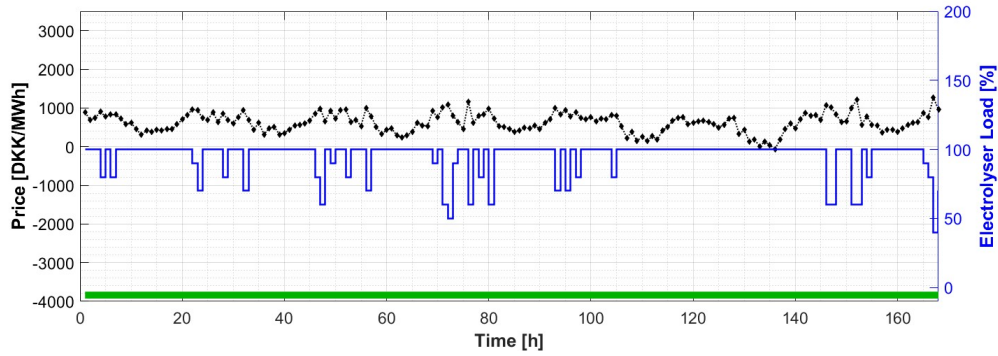

(a) Week 6 – High demand scenario.
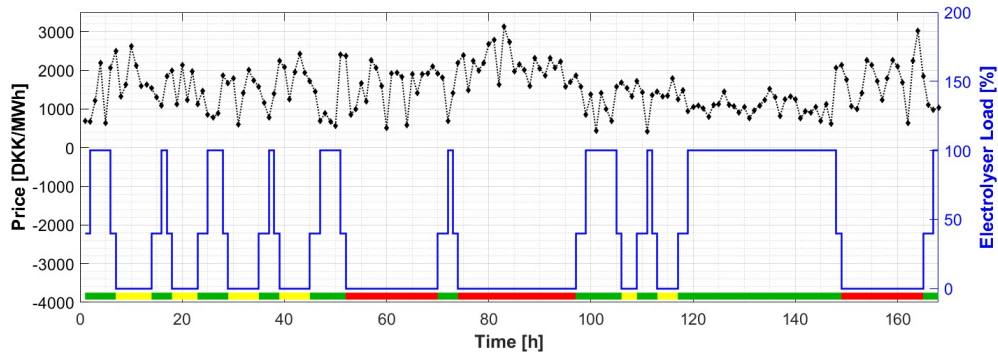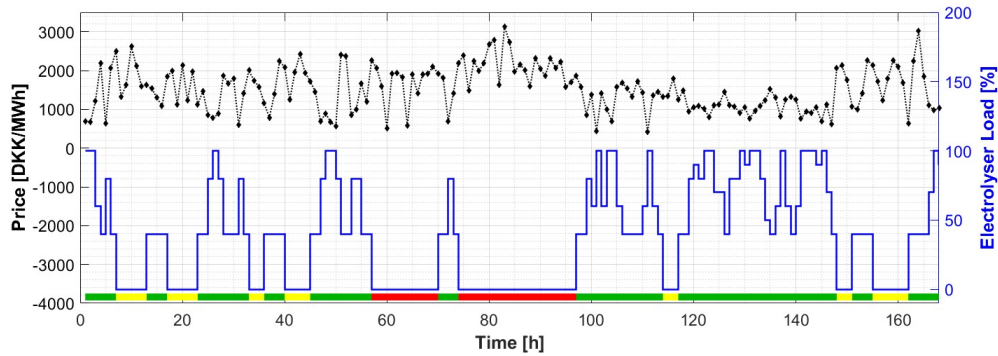

(b) Week 36 – Low demand scenario.

(c) Week 43 – Median demand scenario.

Figure 5.32: Electrolyser operation states during three selected weeks for Phase 1 model.

Under the Phase 1 model, the electrolyser runs continuously at 100% capacity during Week 6 (Figure 5.32a) due to high production demand and low electricity prices. In contrast, Week 36 (Figure 5.32b) shows frequent transitions between standby and shutdown modes, reflecting efforts to minimise operation during expensive electricity hours. For the median week (Figure 5.32c), the electrolyser toggles mainly between running and standby modes, without entering shutdown. This behaviour highlights the model's sensitivity to electricity prices and production demand.

(a) Week 6 – High demand scenario.

(b) Week 36 – Low demand scenario.
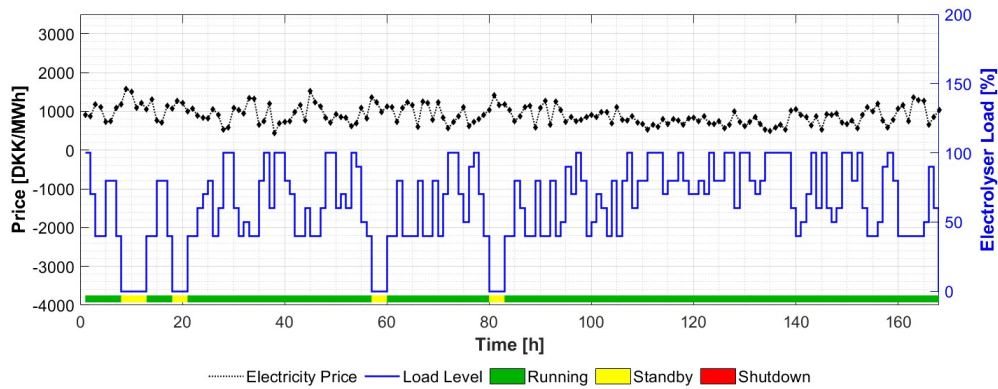
(c) Week 43 – Median demand scenario.

Figure 5.33: Electrolyser operation profiles for three selected weeks under the Phase 2 model with load flexibility (40–100%).

In the Phase 2 results, more stable and efficient operation is observed due to the ability to

adjust load continuously. For instance, in Figure 5.33a for high demand week, the electrolyser operates continuously without any need for standby mode. In Week 36 (Figure 5.33b), although high electricity prices still lead to some shutdowns, the number of shutdown periods is reduced compared to Phase 1. Finally, in the median demand week, the Figure 5.33c shows that the system operates more smoothly with minimal standby periods and no shutdowns, demonstrating that partial load capability allows for increased runtime, potentially reducing electrolyser degradation associated with frequent start-stop cycles.

5.5.4   Annual Electrolyser Operation and Methanol Production Cost

With the optimisation framework fully defined, the Phase 2 and 1 models were executed across all weeks of the year. This approach provided a detailed hour by hour profile of the electrolyser's operating states throughout the entire year. Figure 5.34 presents a pie chart summarising the total distribution of operational states for the electrolyser for Phase 2. It reveals that the unit operated in running mode approximately 86% of the time, with the majority of this time spent at full capacity (100% load). The remaining time was distributed across lower partial load levels, standby, and shutdown modes. Furthermore, over the course of the year, the electrolyser entered shutdown mode less than 30 times and switched to standby mode approximately 160 times.
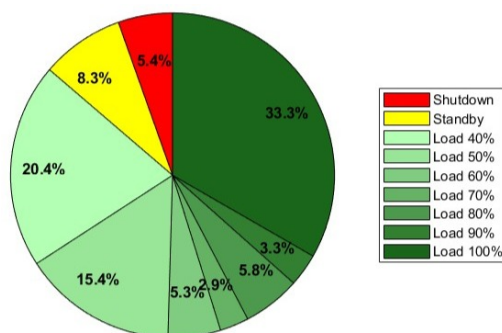

Figure 5.34: Electrolyser operational state distribution over a full year (Phase 2).

Building on this operational profile, the associated cost structure of the entire system was analysed. Figure 5.35 illustrates the breakdown of total annual costs for Phase 2. The cost of H_2 production via the electrolyser dominates the overall system cost, accounting for more than 83% of the total. This reflects the electricity intensive nature of electrolysis. The CAPEX of the entire plant is the second-largest contributor, followed by the expense related to CO_2 supply. The energy consumption of the MSD unit, by contrast, represents only a small fraction, around 3.5 %, of the total cost, highlighting the comparatively low operational burden of the downstream process.
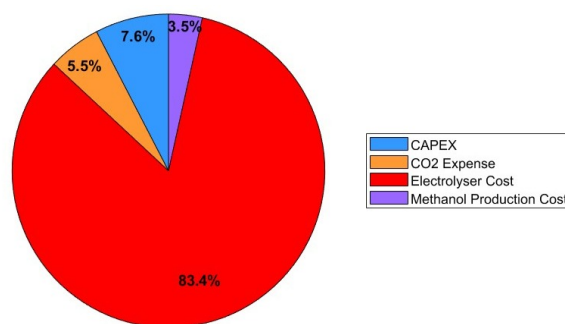
Figure 5.35: Cost distribution for Phase 2 based on annual operation.

Table 5.10 compares the final MeOH production costs for both operational strategies. The more flexible Phase 2 model resulted in a lower cost of 1196.4 €/tonne, compared to 1240.1 €/tonne under Phase 1. This reduction of nearly 50 €/tonne can be attributed to the improved ability to shift production away from high-cost electricity periods and to minimise shutdowns. The resulting MeOH cost falls within the current production cost range for

Table 5.10: MeOH Price Comparison Across Phases

Phase	Methanol Price [€/tonne]
Phase 1	1240.1
Phase 2	1196.4

renewable MeOH systems, as shown in Figure 2.10. While this confirms the technical and economic feasibility of the proposed setup, it also suggests potential for further optimization.

5.5.5 Sensitivity Analysis on Economic Parameters

To better understand the economic stability of the system, a sensitivity analysis was conducted on key external cost drivers. Two parameters were selected for evaluation due to their significant influence on methanol production cost: the price of carbon dioxide and the efficiency of the electrolyser.

Impact of CO_2 Price on Methanol Cost

As previously discussed in Section 2.4, CO_2 used for MeOH production can be obtained from different sources. In this study's baseline optimisation, CO_2 was assumed to be captured from industrial point sources. This is currently the most commonly applied method due to its relatively low cost, approximately 50 €/tonne. However, to transition toward fully renewable e- MeOH production, alternative CO_2 sources must be considered. If biomass-based CO_2 is used, the cost rises to around 200 €/tonne. In this case, the methanol production cost increases to just over 1400 €/tonne. At the upper extreme, direct air capture (DAC) CO_2 , currently priced around 400 €/tonne, raises the MeOH price above 1700 €/tonne, as shown in Figure 5.36.
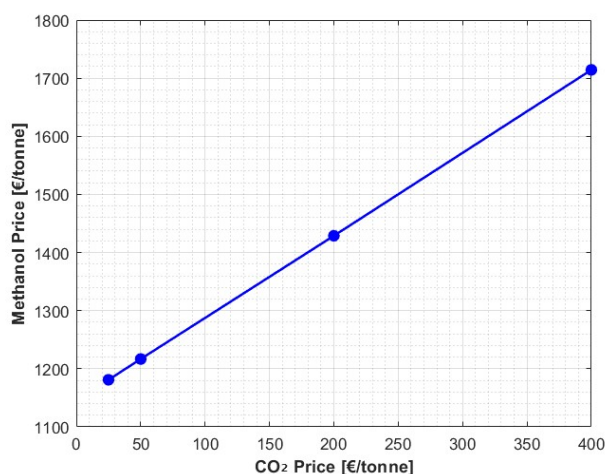
Figure 5.36: Effect of carbon dioxide price on MeOH production cost.

These results highlight the tradeoff between economic feasibility and environmental sustainability. While renewable carbon dioxide sources offer a pathway to fully decarbonised MeOH, they significantly increase production costs compared to fossil-based CO_2.

Impact of Electrolyser Efficiency on Methanol Cost

The potential impact of electrolyser technology improvement presents a compelling case for continued research and development in this field. As illustrated in Figure 5.37, a 5% improvement in electrolyser efficiency under identical operating conditions would result in a reduction in MeOH production cost, from 1196.4 €/tonne to approximately 1147 €/tonne under the Phase 2 operational strategy. This 50 €/tonne reduction represents a 4.1% decrease in overall production costs. Given that H_2 production via electrolysis accounts for over 80% of the total system costs, efficiency improvements translate directly into significant economic benefits, highlighting the importance of continued technological development in electrolyser systems.
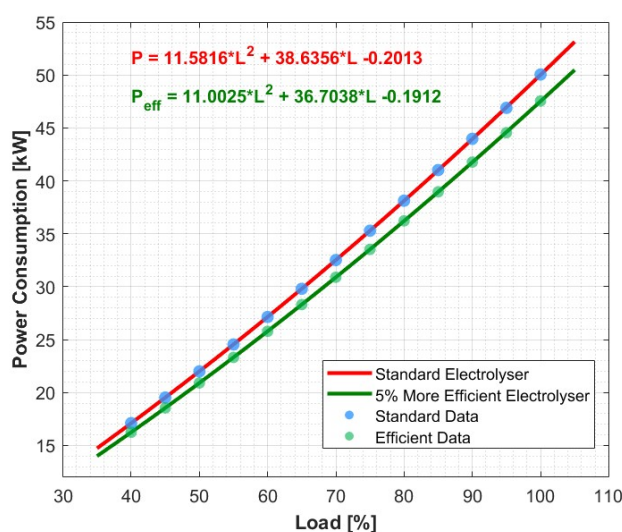

Figure 5.37: Effect of electrolyser efficiency on MeOH production cost

Chapter 6

Discussion

This chapter connects the results to the broader context of e-Methanol (e-MeOH) production cost and highlights the main challenges that were identified.

6.0.1 Cost Analysis

The capital expenditure (CAPEX) analysis showed that the electrolyser is by far the most expensive part of the system, making up almost 90% of the total CAPEX. This confirms that the electrolyser is currently the main economic barrier to cost-competitive e-MeOH. This observation is consistent with the findings of Ikonen (2023) [63], who reported that approximately 85% of the total CAPEX is associated with the electrolyser. However, this economic landscape may shift significantly in the future. As electrolyser technology advances and manufacturing scales increase, unit costs are expected to decline substantially. Furthermore, if PEM electrolysers (PEMEL) can operate at pressures higher than 70 bar, such as 200 bar as demonstrated at laboratory scale by Hancke et al.(2022) [15], this could reduce both the reactor volume and the power consumption of the compressor by increasing conversion in the MeOH synthesis (MS) loop. This would simplify the system and help lower the overall production cost. On the operational side, this study found that approximately 83% of the total annual cost is attributed to electrolyser operating expense (OPEX). This closely aligns with the 85% reported by Taslimi et al. (2024) [10], further highlighting the dominant role of the electrolyser in both CAPEX and OPEX.

The calculated e-MeOH production cost of 1196 €/tonne falls within a realistic and competitive range when compared with existing literature. According to IRENA reports, current e-MeOH production costs typically range from 745 to 1490 €/tonne, placing this study's results well within that spectrum. When comparing with other reference studies, several factors help explain the observed differences. Taslimi et al. (2024) [10] report slightly lower MeOH costs, which can be attributed to the use of lower electricity prices based on pre-war market conditions. Yi Zheng et al. (2022) [4] presents a broader cost range of 584 to 1146 €/tonne, depending on the source and price of carbon dioxide CO_2, as well as the use of off-grid renewable electricity. This explains why the result in this report is slightly above the lower end of that range. Fuglsang (2022) [12] reports costs between 1084 and 1108 €/tonne, closely aligning with the outcome of this study. Lastly, Sollai et al. (2023) [13] reports a cost of 960 €/tonne. One possible explanation for this lower value is the use of a significantly larger hydrogen (H_2) buffer tank, which allows for greater operational flexibility and potentially more cost-efficient load scheduling of the electrolyser.

6.0.2 Components

The PEMEL analysis demonstrates that electrolyser power consumption has a non-linear relationship with current load variations, directly correlating with varying efficiency across

different operating conditions. In the operational range from 40% to 100% load capacity, cell efficiency gradually decreases as current density increases, declining from 76% at low current densities to around 67% at 2.14 A/cm^2. The efficiency degradation is caused by the increase in overpotentials, with ohmic overpotential representing the dominant loss mechanism. It is primarily caused by increased ion flow resistance within cell components, particularly across the proton exchange membrane. While maintaining the stack humid helps minimise these resistive losses, technological improvements also present the improvement possibility, by reducing membrane thickness and implementing higher-conductivity materials. These advancements present opportunities for efficiency improvements, which could reduce power consumption. These efficiency gains would have positive effects on the overall economics of H_2 production and impact the cost competitiveness of MS.

The adiabatic fixed-bed reactor was chosen because it has the lowest capital cost. However, this type of reactor might not be the best option when the system needs to handle frequent changes in load or when it is turned on and off often. Other designs, such as gas-cooled or water-cooled reactors, might handle these conditions better [20]. In this study, transitions between standby and running modes were not modelled in detail. Instead, values for energy use and response time were taken from Mbatha et al. (2024)[20] and Lagoni (2023) [65]. Future work should include simulations that show how different reactor types behave during these transitions to better understand their impact on system performance.

The recycle loop and purge settings in MS had a big impact on how well the system used CO_2 and how efficient it was overall. A low purge ratio was chosen to avoid wasting gas and to reduce emissions. However, this setting might need to be adjusted if the CO_2 comes from other sources, like biomass, since those can contain more inert gases. In MeOH distillation (MD) unit, the distillation column does require a great amount of energy because of reboiler. Some of this heat demand was reduced by using recovered heat from within the system. Still, there might be ways to make the process more efficient, such as using more than one distillation column. Wastewater treatment was not modelled in detail. Instead, the system was designed to produce clean H_2O at the outlet so that very little energy would be needed for any further treatment.

6.0.3 System

Although both surrogate models and detailed dynamic electrolyser models were developed during this work, they are not directly integrated into the optimisation framework. Future work should focus on connecting these models directly to the optimisation code, which would enable comprehensive dynamic simulations and facilitate the development of improved control strategies for real-world operation. This integration would allow for more accurate representation of system behaviour under varying operating conditions and provide better insights for optimal system design and control.

Electricity pricing was not analysed in detail in this study, as the price data were provided through collaboration with another student. The values used reflect recent grid market conditions, which differ from those in earlier reference studies such as Taslimi et al. (2024) [10], where electricity costs were based on cost levels before Ukraine war. This difference in pricing directly affects the comparison of economic results. Using off-grid electricity

sources, such as a co-located wind or solar farm, could reduce production costs by avoiding exposure to volatile electricity market prices. However, this approach would require a high initial CAPEX investment and some form of energy storage to manage periods without sun or wind. A hybrid approach that combines both grid and off-grid electricity could offer a more balanced solution and should be explored further in future work.

While excess heat recovery was incorporated for the MeOH synthesis and distillation (MSD) portion of the system, the substantial amount of excess heat generated by the PEMEL was considered low-value and therefore excluded from the economic analysis. Given the significant quantity of this excess heat, this assumption may be overly conservative, especially for the cold countries like Denmark. If this low-grade heat could be monetised through district heating applications or other uses, it could further reduce the calculated MeOH production cost.

The CO_2 price used in this study was based on the reference work by Taslimi (2024) [10], where CO_2 is assumed to be sourced from industrial emissions. The sensitivity of MeOH production cost to CO_2 price variations was also highlighted in the analysis by Yi Zheng et al. (2022) [4], and further confirmed in Subsection 5.5.5. The most environmentally sustainable option would involve using CO_2 from direct air capture (DAC). However, DAC currently represents the most expensive CO_2 source available, raising the MeOH production cost to over 1700 €/tonne ([1]). This highlights the challenge of balancing environmental ambitions with economic feasibility in the development of e-MeOH systems.

The number of operating hours and the frequency of shutdowns have a direct impact on the durability of the PEM electrolyser. Frequent voltage fluctuations can accelerate the degradation of the electrolyte membrane, ultimately reducing the lifespan of the system [59]. In this study, the electrolyser was assumed to operate at constant pressure, which helps improve durability by avoiding mechanical stress caused by pressure fluctuations on the membrane and electrode assemblies. When comparing the Phase 1 and Phase 2 optimisation models, the introduction of flexible operation in Phase 2 not only reduced the overall production cost, but also decreased the number of shutdowns and standby periods. This improvement contributes to better long-term durability of the electrolyser. Still, over the course of one year, the electrolyser in Phase 2 entered shutdown mode around 30 times. Ideally, this number should be reduced further to minimise wear and improve system reliability. One possible way to achieve this is by lowering the minimum operating load of the electrolyser from 40% to 20%. This would allow the system to continue operating at low output during periods of high electricity prices, rather than shutting down completely. When comparing the operating load distribution to Taslimi et al. (2024) [10], similar patterns are observed. In both cases, the electrolyser spends the majority of its time operating at full load, while roughly one third of the time is spent at partial or minimum load. This suggests a balanced and validated operating profile.

The chosen production target of 25,000 tonnes per year significantly influences the calculated MeOH price. Smaller demand scenarios would enable operation during only the lowest-cost electricity periods, thereby reducing overall production costs. Conversely, larger production demands would force operation during higher-cost periods, increasing the average production cost.

Chapter 7

Conclusion

This study successfully addressed the three critical challenges identified in e-methanol (e-MeOH) production through comprehensive modelling, optimisation, and economic analysis of an integrated power-to-MeOH (PtMeOH) system.

Steady-state and dynamic model development is done for all major system components. The PEM electrolyser (PEMEL) model achieved high accuracy with 0.89% mean absolute error (MAE) when validated against experimental data, capturing the non-linear efficiency-load relationship that varies from 76% at low loads to 67% at rated capacity. The MeOH synthesis and distillation (MSD) system model demonstrated stable dynamic performance for load transitions while maintaining product specifications above 99.7% MeOH purity. The developed Long short-term memory (LSTM) surrogate model achieved excellent predictive accuracy and is used for system evaluation.

System flexibility evaluation is done after systems were built to see operational advantages related to variable load capability. The dynamic coupling between PEMEL and MSD systems was successfully characterised, showing that flexible operation (Phase 2) reduced production costs by 50 €/tonne compared to fixed-load operation (Phase 1). The system achieved 86% annual runtime with strategic use of partial loads during moderate electricity price periods, effectively minimising harmful start-stop cycles while maintaining economic efficiency.

Cost-effective optimisation demonstrated that e-MeOH can be produced at 1196.4 €/tonne under optimal flexible operation, positioning it within the competitive range of current renewable MeOH technologies. The economic analysis confirmed that electrolyser costs dominate both capital expenditure (CAPEX) (90%) and operational expenditure (OPEX) (83%), identifying this as the primary target for cost reduction. Sensitivity analysis also revealed critical dependencies on CO_2 cost as well as electrolyser efficiency improvements.

Key limitations include neglecting of pressure changes in the electrolyser part of the system, simplifying assumptions related to hydrogen (H_2) buffer tank, missing investigation on cold and hot start-up of MSD and conservative excess heat utilisation assumptions. The study confirms that while current e-MeOH production costs exceed fossil-MeOH prices, the demonstrated operational flexibility and identified improvement pathways provide a clear route toward economic competitiveness. The developed modelling framework and optimisation methodology offer an example of practical tools for commercial PtMeOH developments, contributing to the broader implementation of Power-to-X (PtX) technologies in sustainable energy systems.

Future research should focus on directly integrating components in the optimisation for more advanced optimisation strategies, exploring hybrid electricity supply configurations, investigating higher-pressure electrolyser operation to further improve system performance and gaining a deeper understanding of MSD behaviour during standby and shutdown conditions.

Bibliography

[1] IRENA and Methanol Institute. *Innovation Outlook: Renewable Methanol*. Tech. rep. International Renewable Energy Agency, 2021. URL: https://www.irena.org/publications.

[2] DNV. *Hydrogen Forecast to 2050: Energy Transition Outlook 2022*. Tech. rep. DNV, 2022. URL: https://www.dnv.com.

[3] Na Li et al. "A review of reformed methanol-high temperature proton exchange membrane fuel cell systems". In: *Renewable and Sustainable Energy Reviews* 182 (2023), p. 113395. DOI: 10.1016/j.rser.2023.113395. URL: https://doi.org/10.1016/j.rser.2023.113395.

[4] Yi Zheng et al. "Data-driven robust optimization for optimal scheduling of power to methanol". In: *Energy Conversion and Management* 256 (2022), p. 115338. DOI: 10.1016/j.enconman.2022.115338. URL: https://doi.org/10.1016/j.enconman.2022.115338.

[5] Q. Shen et al. "Advancements in methanol distillation system: A comprehensive overview". In: *Processes* 11.3 (2023). DOI: 10.3390/pr11030929.

[6] Samuel Simon Araya et al. *Power-to-X: Technology overview, possibilities and challenges*. Tech. rep. Aalborg University, 2022. URL: https://vbn.aau.dk/en/publications/3bd8d6b3-3651-42e7-a81b-4ee400abb74f.

[7] Erik Lewenhaupt. *Methanol - A Future Fuel for Shipping*. Presented at the IHS Chemical World Methanol Conference. Accessed: 2025-03-28. Stena AB Group, Nov. 2015. URL: https://www.stenabulk.com/sites/default/files/2021-11/Methanol-Future-Fuel-Shipping-IHS-World-Methanol-Conference-Nov15.pdf.

[8] Maersk. *Maersk to deploy first large methanol-enabled vessel on Asia–Europe trade lane*. Accessed: 2025-03-28. Dec. 2023. URL: https://www.maersk.com/news/articles/2023/12/07/maersk-to-deploy-first-large-methanol-enabled-vessel-on-asia-europe-trade-lane.

[9] Yi Zheng et al. "Optimal day-ahead dispatch of an alkaline electrolyser system concerning thermal–electric properties and state-transitional dynamics". In: *Applied Energy* 307 (2022), p. 118091. DOI: 10.1016/j.apenergy.2021.118091. URL: https://doi.org/10.1016/j.apenergy.2021.118091.

[10] Melika Sadat Taslimi et al. "Optimization and analysis of methanol production from CO2 and solar-driven hydrogen production: A Danish case study". In: *International Journal of Hydrogen Energy* 69 (2024), pp. 466–476. DOI: 10.1016/j.ijhydene.2024.05.033. URL: https://doi.org/10.1016/j.ijhydene.2024.05.033.

[11] European Energy. *European Energy produces first raw e-methanol at Kassø*. Accessed: 2025-03-23. Mar. 2025. URL: https://europeanenergy.com/2025/03/12/european-energy-produces-first-raw-e-methanol-at-kasso/.

[12] Mathias Fuglsang and Frede Hvelplund. "Feasibility study of Power-to-Methanol in Denmark". In: *Aalborg University, Department of Planning* N/A (2022), p. 57. DOI: N/A. URL: N/A.

[13] Stefano Sollai et al. "Renewable methanol production from green hydrogen and captured CO_2: A techno-economic assessment". In: *Journal of CO_2 Utilization* 68 (2023), p. 102345. DOI: 10.1016/j.jcou.2022.102345. URL: https://doi.org/10.1016/j.jcou.2022.102345.

[14] Luísa Marques et al. "Review of Power-to-Liquid (PtL) Technology for Renewable Methanol (e-MeOH): Recent Developments, Emerging Trends and Prospects for the Cement Plant Industry". In: *Preprints* (Sept. 2024). Not peer-reviewed. DOI: 10.20944/preprints202409.0956.v1. URL: https://doi.org/10.20944/preprints202409.0956.v1.

[15] Ragnhild Hancke, Thomas Holm, and Øystein Ulleberg. "The Case for High-Pressure PEM Water Electrolysis". In: *Energy Conversion and Management* 261 (2022), p. 115642. DOI: 10.1016/j.enconman.2022.115642. URL: https://doi.org/10.1016/j.enconman.2022.115642.

[16] Dana S. Marlin, Emeric Sarron, and Ómar Sigurbjörnsson. "Process Advantages of Direct CO to Methanol Synthesis". In: *Frontiers in Chemistry* 6 (2018), p. 446. DOI: 10.3389/fchem.2018.00446. URL: https://doi.org/10.3389/fchem.2018.00446.

[17] Xiaoti Cui and Søren Knudsen Kær. "A comparative study on three reactor types for methanol synthesis from syngas and CO". In: *Chemical Engineering Journal* 393 (2020), p. 124632. DOI: 10.1016/j.cej.2020. 124632.

[18] Mustapha Grema Mohammed et al. "Overview of the latest progress and prospects in the catalytic hydrogenation of carbon dioxide (CO) to methanol in membrane reactors". In: *International Journal of Hydrogen Energy* 77 (2024), pp. 936–957. DOI: 10.1016/j.ijhydene.2024.06.138.

[19] Boreum Lee et al. "Renewable methanol synthesis from renewable H_2 and captured CO_2: How can power-to-liquid technology be economically feasible?" In: *Applied Energy* 279 (2020), p. 115827. DOI: 10.1016/j.apenergy.2020.115827. URL: https://doi.org/10.1016/j.apenergy.2020.115827.

[20] Siphesihle Mbatha et al. "Detailed assessment of dynamic startup, shutdown, and flexibility of the adiabatic, gas-and water-cooled methanol fixed bed reactor: comparison for power to methanol application". In: (2024).

[21] DNV. *Energy Transition Outlook 2024: A global and regional forecast to 2050*. DNV report. 2024. URL: https://www.dnv.com/eto.

[22] Andrea Barisione. "Performance analysis of a PEM Electrolyzer system: dynamic simulation and scale-up study". Advisor: Dr. Paolo Colbertaldo. Co-advisor: Dr. Giulio Guandalini, Ing. Marco Ficili. Master's thesis. Politecnico di Milano, 2023. URL: https://www.polimi.it.

[23] Lorenzo Garibaldi. "Dynamic modelling of a high-power electrolyser: A study of green hydrogen generation from an offshore wind turbine and a wave energy converter". Master's Thesis, supervised by G. Giorgi, G. Bracco, and M. Retes Peñalba. MA thesis. Politecnico di Torino, 2022. URL: https://webthesis.biblio.polito.it/.

[24] Nord Pool Group. *Day-ahead Market Prices (AT, DK1) – Latest Daily Aggregate*. https://data.nordpoolgroup.com/auction/day-ahead/prices?deliveryDate=latest&currency=EUR&aggregation=DailyAggregate&deliveryAreas=AT,DK1. Accessed: 2025-04-30. 2025.

[25] Guanghao Wang et al. "The impact of renewable energy on extreme volatility in wholesale electricity prices: Evidence from Organisation for Economic Co-operation and Development countries". In: *Journal of Cleaner Production* 484 (2024), p. 144343. DOI: 10.1016/j.jclepro.2024.144343. URL: https://doi.org/10.1016/j.jclepro.2024.144343.

[26] GridX. *What is a negative energy price in Europe?* https://www.gridx.ai/knowledge/what-is-negative-energy-price-in-europe. Accessed: 2025-04-30. 2024.

[27] Xiaoti Cui. *Introduction to Power-to-X systems*. https://www.energy.aau.dk/. Lecture slides, AAU Energy, Oct. 2024. 2024.

[28] Annalicia Poehler and COWI. *Power-to-X: The Hydrogen Vector and Green Fuel Pathways*. https://www.cowi.com. Conference presentation, June 15, 2022. 2022.

[29] Inamuddin, Mohammad Luqman, and Abdullah M. Asiri. *Electrolysis: Theory, Types and Applications*. Cambridge: Royal Society of Chemistry, 2020. ISBN: 978-1-78801-378-9. URL: https://doi.org/10.1039/9781788013789.

[30] Kennedy Space Center, Center Operations Directorate. *Liquid Hydrogen Consumption During Space Shuttle Program*. Internal presentation or report. Presented on February 25, 2011. 2011.

[31] Vincenzo Liso. *Fuel Cells, Hydrogen Technology and Power-to-X – Electrolysis Systems, Hydrogen Physical Properties, and Compression*. https://www.energy.aau.dk/. Lecture slides, AAU Energy, Lecture 5, accessed 2025-04-30. 2024.

[32] Michael Sura. *Reflections on NASA's Liquid Hydrogen Consumption and Implications for Hydrogen Handling*. https://www.linkedin.com/feed/update/urn:li:activity:7300152441402990593/. Accessed: 2025-04-30. 2025.

[33] NOAA Global Monitoring Laboratory. *Trends in Atmospheric Carbon Dioxide*. Accessed: May 8, 2025. 2024. URL: https://gml.noaa.gov/ccgg/trends/.

[34] United Nations Framework Convention on Climate Change (UNFCCC). *The Paris Agreement*. Accessed: May 8, 2025. 2015. URL: https://unfccc.int/process-and-meetings/the-paris-agreement.

[35] Samuel Shiferaw Araya et al. "Hydrogen and Synthetic Fuel-Based Energy Storage: Electrochemical and Thermal Conversion Pathways". In: *Energies* 13.3 (2020), p. 596. DOI: 10.3390/en13030596.

[36] George A. Olah, Alain Goeppert, and G. K. Surya Prakash. "Chemical recycling of carbon dioxide to methanol and dimethyl ether: From greenhouse gas to renewable, environmentally carbon neutral fuels and synthetic hydrocarbons". In: *Renewable and Sustainable Energy Reviews* 16.1 (2012), pp. 482–496. DOI: 10.1016/j.rser.2011.09.002.

[37] Iberdrola. *Puertollano Green Hydrogen Plant*. Accessed: 2025-05-11. 2025. URL: https://www.iberdrola.com/about-us/what-we-do/green-hydrogen/puertollano-green-hydrogen-plant.

[38] Anita H. Reksten et al. "Projecting the future cost of PEM and alkaline water electrolysers: a CAPEX model including electrolyser plant size and technology development". In: *International Journal of Hydrogen Energy* 47 (2022), pp. 38106–38113. DOI: 10.1016/j.ijhydene.2022.08.306. URL: https://doi.org/10.1016/j.ijhydene.2022.08.306.

[39] Electric Hydrogen. *PEM vs. Alkaline: Re-examining Market Perceptions of Electrolyzer Technologies in an Evolving Landscape*. https://eh2.com/wp-content/uploads/2025/01/Final_PEM_vs_Alkaline_December_2024_Whitepaper.pdf. Accessed: 2025-05-11. 2024.

[40] Vincenzo Liso et al. "Modelling and Experimental Analysis of a Polymer Electrolyte Membrane Water Electrolysis Cell at Different Operating Temperatures". In: *Energies* 11.12 (2018), p. 3273. DOI: 10.3390/en11123273. URL: https://doi.org/10.3390/en11123273.

[41] Ravindra Datta et al. "Modeling of PEM Water Electrolyzer". In: *PEM Electrolysis for Hydrogen Production: Principles and Applications*. Ed. by Elsevier. Chapter 12. Taylor Francis Group, 2016, pp. 243–265.

[42] Siavash Asiaban, Dimitar Bozalakov, and Lieven Vandevelde. "Development of a dynamic mathematical model of PEM electrolyser for integration into large-scale power systems". In: *Energy Conversion and Management: X* 23 (2024), p. 100610. DOI: 10.1016/j.ecmx.2024.100610. URL: https://doi.org/10.1016/j.ecmx.2024.100610.

[43] A. Awasthi, Keith Scott, and S. Basu. "Dynamic modeling and simulation of a proton exchange membrane electrolyzer for hydrogen production". In: *International Journal of Hydrogen Energy* 36.21 (2011), pp. 14779–14786. DOI: 10.1016/j.ijhydene.2011.03.045. URL: https://doi.org/10.1016/j.ijhydene.2011.03.045.

[44] Malte Pfennig, Barbara Schiffer, and Tanja Clees. "Thermodynamical and electrochemical model of a PEM electrolyzer plant in the megawatt range with a literature analysis of the fitting parameters". In: *International Journal of Hydrogen Energy* 104 (2025), pp. 567–583. DOI: 10.1016/j.ijhydene.2024.04.335. URL: https://doi.org/10.1016/j.ijhydene.2024.04.335.

[45] Jarmo Saari. *Heat Exchanger Dimensioning*. Lecture notes for LOQ4086, Lappeenranta University of Technology. 2005. URL: https://sistemas.eel.usp.br/docentes/arquivos/5817712/LOQ4086/saari_heat_exchanger_dimensioning.pdf.

[46] Huiyong Kim, Mikyoung Park, and Kwang Soon Lee. "One-dimensional dynamic modeling of a high-pressure water electrolysis system for hydrogen production". In: *International Journal of Hydrogen Energy* 38.6 (2013), pp. 2596–2609. DOI: 10.1016/j.ijhydene.2012.12.006. URL: https://doi.org/10.1016/j.ijhydene.2012.12.006.

[47] Edward Rauls et al. "Favorable Start-Up behavior of polymer electrolyte membrane water electrolyzers". In: *Applied Energy* 330 (2023), p. 120350. DOI: 10.1016/j.apenergy.2022.120350. URL: https://doi.org/10.1016/j.apenergy.2022.120350.

[48] Enapter. *Warm-up time of Enapter Electrolyser*. https://www.enapter.com/kb_post/what-is-the-duration-of-starting-the-electrolyser-until-it-is-fully-functional-how-long-is-the-warm-upramp-up-time/?utm_source=chatgpt.com. 2023.

[49] A. Ali et al. "Review of catalysts for CO_2 hydrogenation to methanol: A focus on recent advancements and future directions". In: *Unpublished Manuscript* (2024). Accessed via personal communication or private repository.

[50] K. M. Vanden Bussche and G. F. Froment. "A steady-state kinetic model for methanol synthesis and the water gas shift reaction on a commercial $Cu/ZnO/Al_2O_3$ catalyst". In: *Journal of Catalysis* 161.1 (1996), pp. 1–10. DOI: 10.1006/jcat.1996.0156.

[51] L.M. Al-Mallah. *Aspen Plus® Chemical Engineering Applications*. 1st. Chapter 7: Reactors with Complex (Non-Conventional) Reaction Kinetic Forms. John Wiley & Sons, Inc., 2017. ISBN: 978-1-119-29126-3.

[52] Xiaoti Cui, Søren Knudsen Kær, and Mads Pagh Nielsen. "Energy analysis and surrogate modeling for the green methanol production under dynamic operating conditions". In: *Fuel* 307 (2022), p. 121924. DOI: 10.1016/j.fuel.2021.121924. URL: https://doi.org/10.1016/j.fuel.2021.121924.

[53] *Designing of Distillation Column in Aspen Plus*. Tutorial document on distillation modeling using Aspen Plus, including DSTWU and RadFrac methods. Educational Institute for Equipment and Process Design. 2023.

[54] William L. Luyben. *Distillation Design and Control Using Aspen Simulation*. Wiley-AIChE. Hoboken, NJ: John Wiley & Sons, 2013. ISBN: 978-1-118-80152-2.

[55] William L. Luyben. *Plantwide Dynamic Simulators in Chemical Processing and Control*. New York: Marcel Dekker, 2002.

[56] Greg Van Houdt, Carlos Mosquera, and Gonzalo Nápoles. "A review on the long short-term memory model". In: *Artificial Intelligence Review* 53.8 (2020), pp. 5929–5955. DOI: 10.1007/s10462-020-09838-1.

[57] Xiaonan Li et al. "A review of machine learning for the optimization of energy systems". In: *Applied Energy* 277 (2020), p. 115397. DOI: 10.1016/j.apenergy.2020.115397. URL: https://www.sciencedirect.com/science/article/pii/S0306261920315671.

[58] M. R. Teles. "Optimization and Analysis on Variable Operation Conditions of Green Methanol Plant". MA thesis. Technical University of Denmark, 2022. URL: https://orbit.dtu.dk/en/publications/optimization-and-analysis-on-variable-operation-conditions-of-gree.

[59] "Water Electrolyzer Stack Degradation". In: (2022). Technology Brief. URL: https://www.netl.doe.gov/sites/default/files/netl-file/WATER-ELECTROLYZER-STACK-DEGRADATION.pdf.

[60] Monjid Hamdan and Kevin Harrison. *MW-Scale PEM-Based Electrolyzers for RES Applications*. DOE Hydrogen and Fuel Cells Program Annual Merit Review. 2019. URL: https://www.nrel.gov/docs/fy19osti/73388.pdf.

[61] Robin Smith. *Chemical Process Design and Integration*. Chichester, England: John Wiley & Sons, 2005. ISBN: 9780471486807.

[62] *Al2O3 Copper Catalyst Price — Market Listing*. https://www.made-in-china.com/products-search/hot-china-products/Al2o3_Copper_Catalyst.html. Accessed May 2025. 2024.

[63] Jonathan Ahlbäck Ikonen. "Techno-economic analysis of large-scale production of e-methanol via CO-hydrogenation in Power-to-X". AFRY Report. MA thesis. Department of Chemical Engineering, Lund University, 2023.

[64] Haluk Görgün. "Dynamic modelling of a proton exchange membrane (PEM) electrolyzer". In: *International Journal of Hydrogen Energy* 31.1 (2006), pp. 29–38. DOI: 10.1016/j.ijhydene.2005.04.001. URL: https://doi.org/10.1016/j.ijhydene.2005.04.001.

[65] Nils Thomas Schneider and Zenia Lagoni. "Flexibility of Power-to-Methanol in 2030: An Investigation of the Flexibility Provided Through Electricity Consumption in Different Scenarios for 2030". Supervised by Peter Sorknæs. Master's Thesis. Department of Planning, Aalborg University: Aalborg University, 2023.